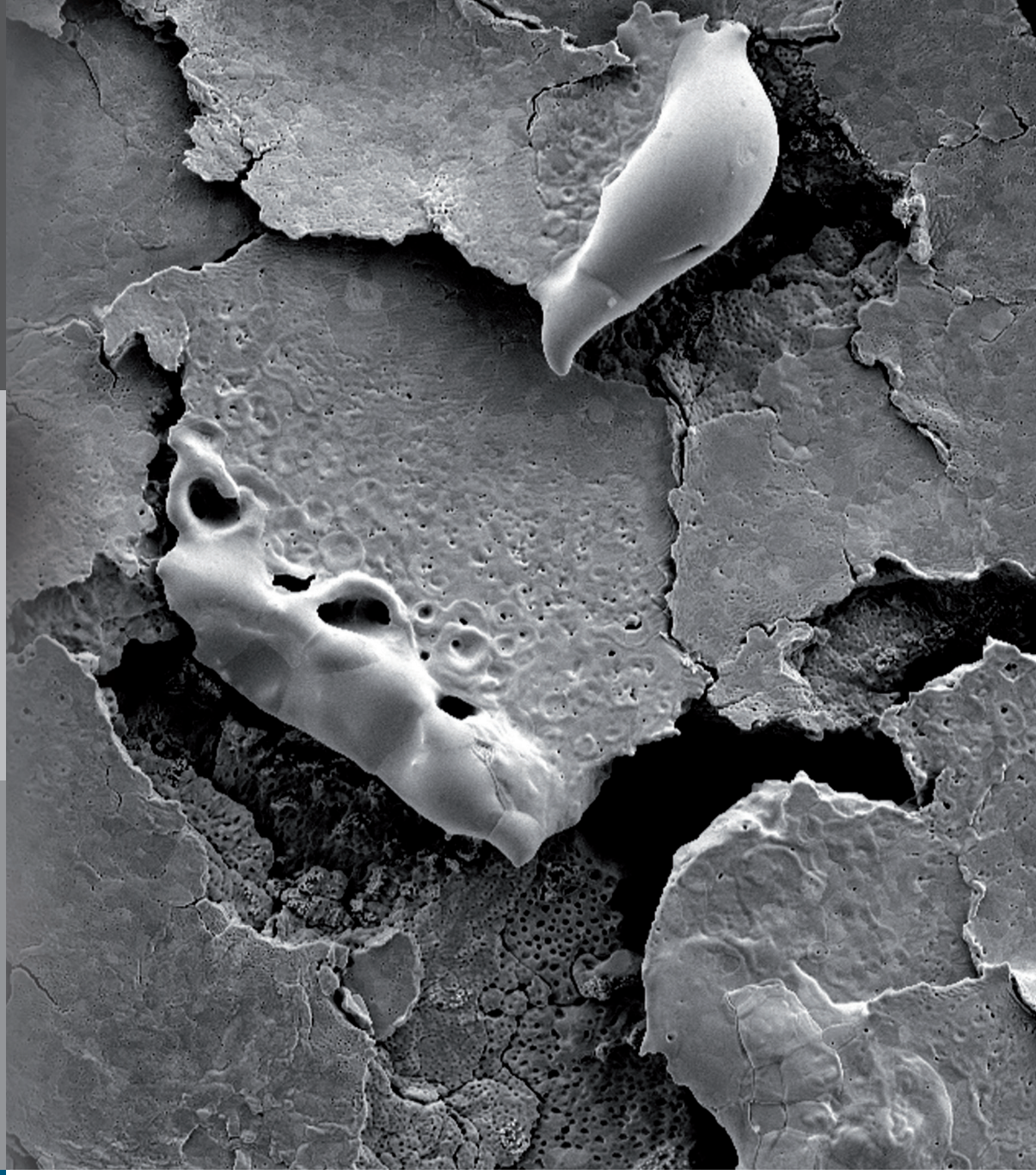

Thermal Shock Behaviour of Different Tungsten Grades under Varying Conditions

Oliver Marius Wirtz

Mitglied der Helmholtz-Gemeinschaft

JÜLICH
FORSCHUNGSZENTRUM

Schriften des Forschungszentrums Jülich
Reihe Energie & Umwelt / Energy & Environment Band / Volume 161

Forschungszentrum Jülich GmbH
Institute of Energy and Climate Research (IEK)
Microstructure and Properties of Materials (IEK-2)

Thermal Shock Behaviour of Different Tungsten Grades under Varying Conditions

Oliver Marius Wirtz

Schriften des Forschungszentrums Jülich
Reihe Energie & Umwelt / Energy & Environment Band / Volume 161

ISSN 1866-1793 ISBN 978-3-89336-842-6

Bibliographic information published by the Deutsche Nationalbibliothek.
The Deutsche Nationalbibliothek lists this publication in the Deutsche Nationalbibliografie; detailed bibliographic data are available in the Internet at http://dnb.d-nb.de.

Publisher and Distributor:	Forschungszentrum Jülich GmbH Zentralbibliothek 52425 Jülich Phone +49 (0) 24 61 61-53 68 · Fax +49 (0) 24 61 61-61 03 e-mail: zb-publikation@fz-juelich.de Internet: http://www.fz-juelich.de/zb
Cover Design:	Grafische Medien, Forschungszentrum Jülich GmbH
Printer:	Grafische Medien, Forschungszentrum Jülich GmbH
Copyright:	Forschungszentrum Jülich 2013

Schriften des Forschungszentrums Jülich
Reihe Energie & Umwelt / Energy & Environment Band / Volume 161

D 82 (Diss.,RWTH Aachen University, 2012)

ISSN 1866-1793
ISBN 978-3-89336-842-6

List of symbols and abbreviations

Symbols

ΔT	Temperature rise	[K]
Δt	Pulse duration	[s]
ϵ	Absorption coefficient for electrons	[-]
λ	Thermal conductivity	[$WK^{-1}m^{-1}$]
μ	Poisson´s ratio	[-]
ν	Frequency	[Hz]
ρ	Density	[kgm^{-3}]
σ	Nuclear cross section	[barn]
τ_E	Energy confinement time	[s]
R_a	Arithmetic mean roughness	[μm]
a	Thermal diffusivity	[m^2s^{-1}]
C	Heat capacity	[JK^{-1}]
c	Speed of light	[ms^{-1}]
c_p	Specific heat capacity	[$Jkg^{-1}K^{-1}$]
d	Distance	[m]
F_{HF}	Factor of heat flux	[$MWm^{-2}s^{1/2}$]
I	Current	[A]
I_{abs}	Absorbed current	[A]
I_{inc}	Incident current	[A]
K_D	Kinetic energy	[kgm^2s^{-2}]
K_x	Correlation constant	[-]

m	Mass	[kg]
n	Ion density	[m^{-3}]
n_e	Electron density	[m^{-3}]
P	Power	[W]
P_{abs}	Absorbed power density	[Wm^{-2}]
S	Area	[m^2]
T	Temperature	[K]
t	Time	[s]
T_1	Correction factor	[-]
T_e	Electron temperature	[eV]
U_a	Acceleration voltage	[V]

Abbreviations

BSE	Backscattered Electron
CCD	Charge-Coupled Device
CFC	Carbon Fibre Composite
CS	Cross Section
CTE	Coefficient of Thermal Expansion
DBTT	Ductile-to-Brittle Transition Temperature
DIFFER	Dutch Institute for Fundamental Energy Research
dpa	Displacement Per Atom
DSC	Differential Scanning Calorimetry
EDM	Electric Discharge Machining
EDX	Energy-Dispersive X-ray
ELM	Edge Localized Mode
FEM	Finite Element Method
FIR	Far Infrared
FWHM	Full-Width-Half-Maximum
JUDITH	Juelicher Divertor Test Facility in Hot Cells

L	Longitudinal Grain Structure (in loading direction)
LCMF	Last Closed Magnetic Field Line
LM	Light Microscopy
MARION	Material Research Ion Beam Test Stand
NIR	Near Infrared
pBN	Pyrolytic Boron Nitride
PFC	Plasma-Facing Component
PFM	Plasma-Facing Material
PG	Pyrolytic Graphite
PSI	Plasma Surface Interaction
R	Recrystallised Longitudinal Grain Structure (in loading direction)
RT	Room Temperature
SCK•CEN	Studiecentrum Voor Kernenergie•Centre D'Etude De L'Energie Nucleaire
SEM	Scanning Electron Microscopy
SOL	Scrape-Off Layer
T	Transversal Grain Structure (in loading direction)
TV	Top View
UTS	Ultimate Tensile Strength
VDE	Vertical Displacement Event
W-UHP	Ultra High Purity Tungsten (99.9999 wt%)
WT%	Weight Percentage
WVMW	Tungsten-Vacuum-Metallizing-Tungsten

List of publications

Parts of the results presented in this work have already been published in the following articles:

M. Wirtz, J. Linke, G. Pintsuk; Thermal resistivity of tungsten grades under fusion relevant conditions; *Jahrestagung Kerntechnik* 2010, Compact Nr. 801 (2010).

J. Linke, Th. Loewenhoff, V. Massaut, G. Pintsuk, G. Ritz, M. Rödig, A. Schmidt, C. Thomser, I. Uytdenhouwen, V. Vasechko, M. Wirtz; Performance of different tungsten grades under transient thermal loads; *Nuclear Fusion* 51 (7), art. no. 073017 (2011).

J. W. Coenen, V. Philipps, S. Brezinsek, G. Pintsuk, I. Uytdenhouwen, M. Wirtz, A. Kreter, K. Sugiyama, H. Kurishita, Y. Torikai, Y. Ueda, U. Samm; Melt-layer ejection and material changes of three different tungsten materials under high heat-flux conditions in the tokamak edge plasma of TEXTOR; *Nuclear Fusion* 51 (11), art. no. 113020 (2011).

M. Wirtz, J. Linke, G. Pintsuk, L. Singheiser, I. Uytdenhouwen; Comparison of the thermal shock performance of different tungsten grades and the influence of microstructure on the damage behaviour; *Physica Scripta* T145 , art. no. 014058 (2011).

M. Wirtz, J. Linke, G. Pintsuk, J. Rapp, G. M. Wright; Influence of high flux hydrogen-plasma exposure on the thermal shock induced crack formation in tungsten; *Journal of Nuclear Materials* 420 (1-3), pp. 218-221 (2012).

M. Wirtz, J. Linke, G. Pintsuk, G. De Temmerman, G. M. Wright; Thermal shock behaviour of tungsten after high flux H-plasma loading; *Journal of Nuclear Materials* Submitted.

This work, supported by the European Communities under the contract of Association between EURATOM/Forschungszentrum Jülich, was carried out within the framework of the European Fusion Development Agreement. The views and opinions expressed herein do not necessarily reflect those of the European Commission.

Kurzfassung

Thermonukleare Fusionskraftwerke sind eine vielversprechende Möglichkeit, die Energieversorgung zukünftiger Generationen zu sichern. Allerdings stellt sie uns in vielen Forschungsbereichen vor enorme Herausforderungen. Ein großer Schritt hin zu einem Prototyp eines Fusionsreaktors (DEMO) wird ITER sein, welcher zurzeit in Cadarache in Südfrankreich gebaut wird. Eine der schwierigsten Aufgaben stellt hierbei die Auswahl von geeigneten Werkstoffen dar und ganz besonders die der dem Plasma zugewandten Materialien (plasma facing material, PFM). PFMs, die in einer Anlage wie ITER zu Einsatz kommen, müssen nicht nur extremen stationären und transienten thermischen Belastungen standhalten, sondern auch hohen Wasserstoff-, Helium- und Neutronenflüssen widerstehen. Materialien, die für eine solche Anwendung in Frage kommen, sind Beryllium, Wolfram und Kohlenstofffaserverstärkter Kohlenstoff (carbon fibre composite, CFC).

Wolfram ist der vielversprechendste Werkstoff für eine Anwendung im Bereich des Divertors, wo die extremsten Belastungsbedingungen herrschen und wird aller Wahrscheinlichkeit nach auch als PFM in DEMO Verwendung finden. Aus diesem Grund konzentriert sich die vorliegende Arbeit auf die Untersuchung des Thermoschockverhaltens verschiedener Wolframsorten unter ITER und DEMO relevanten Belastungszuständen, um die zugrundeliegenden Schädigungsmechanismen zu verstehen und Materialeigenschaften zu identifizieren, welche dieses Verhalten beeinflussen. Hierzu wurden sowohl die mechanischen und thermischen Eigenschaften, als auch die Mikrostruktur von fünf industriell hergestellten Wolframsorten charakterisiert. Anschließend wurden alle fünf Materialien bei Temperaturen zwischen RT und 600 °C in der Elektronenstrahlanlage JUDITH 1 transienten thermischen Belastungen mit Leistungsdichten von bis zu 1,27 GWm^{-2} ausgesetzt. Um ein weites Spektrum an Belastungsbedingungen abzudecken und eine übermäßige Arbeitsbelastung der Testanlage zu vermeiden, wurde die maximale Zyklenzahl auf 1000 begrenzt. Die Ergebnisse dieser Experimente ermöglichten es, unterschiedliche Schädigungs- und Rissgrenzwerte für die verschiedenen Materialien festzulegen, sowie bestimmte Materialeigenschaften zu identifizieren, die einen Einfluss auf die Lage dieser Grenzwerte und die Ausprägung der verursachten Schädigungen haben. Darüber hinaus konnte festgestellt werden, dass nicht nur die unterschiedlichen Zusammensetzung der Materialien, sondern auch die Mikrostruktur und die Rekristallisation des Materials einen wesentlichen Einfluss auf die Thermoschockschädigung hat, wie z. B. den Rissverlauf und die Oberflächenaufrauung.

Neben diesen rein thermischen Belastungen wurden Wolframproben nacheinander mit Wasserstoffplasma hoher Flussdichte und zyklischen Thermoschocks belastet. Die aus

diesen Versuchen erhaltenen Ergebnisse sollten Aufschluss darüber geben, ob die zusätzliche Belastung mit hohen Teilchenflüssen einen Einfluss auf das Thermoschockverhalten von Wolfram hat. Hierbei wurde vor allem auf die Veränderung der Thermoschockrissparameter wie Rissabstand, -breite und -tiefe geachtet. Die Ergebnisse haben gezeigt, dass besonders die Vorbelastung mit Wasserstoffplasma einen signifikanten Einfluss auf das Thermoschockverhalten von Wolfram hat. Neben der Abfolge der Belastungszustände konnte die Oberflächentemperatur der Wolframproben während der Plasmabelastung als weiterer Einflussparameter auf das Materialverhalten identifiziert werden. Eine der offensichtlichsten Veränderungen aufgrund der Vorbelastung mit Wasserstoff ist, dass die Thermoschockrisse nicht länger auf den elektronenstrahlbelasteten Bereich beschränkt sind. Sie breiten sich sowohl in dem Bereich, der zuvor mit Plasma belastet wurde, also auch im unbelasteten Randbereich der Wolframproben aus. Darüber hinaus ist bei der Vorbelastung von Wolframproben mit Wasserstoff eine generelle Abnahme aller Rissparameterwerte zu beobachten.

Die Kombination dieser Ergebnisse zeigt, dass das Thermoschockverhalten von Wolfram sehr komplex ist und von einer großen Bandbreite von Parametern beeinflusst wird. Die Auswirkungen extremer thermischer Belastungen auf unterschiedliche Wolframsorten können sehr gut mittels Elektronenstrahltest simuliert und charakterisiert werden, allerdings ohne den Einfluss hoher Teilchenflüsse zu berücksichtigen. Der Einfluss von Wasserstoffplasma hoher Flussdichten kann aus den nacheinander erfolgten Belastungsexperimenten abgeschätzt werden. Die Ergebnisse bieten einen guten Überblick der zu erwartenden Materialschädigung von Wolfram als PFM. Zusätzlich zeigen sie, dass die bei starken thermischen Belastungen in Kombination mit hohen Teilchenflüssen verursachten Schädigungen an der Materialoberfläche schädlich für den Betrieb von zukünftiger Fusionsanlagen wie ITER oder DEMO sind und signifikanten Einfluss auf deren Betriebsbedingungen für 10^6 oder mehr Zyklen, wie sie in ITER erwartet werden, haben.

Abstract

Thermonuclear fusion power plants are a promising option to ensure the energy supply for future generations, but in many fields of research enormous challenges have to be faced. A major step on the way to the prototype fusion reactor DEMO will be ITER which is build in Cadarache, southern France. One of the most critical issues is the field of in-vessel materials and components, in particular the plasma facing materials (PFM). PFMs that will be used in a device like ITER have to withstand severe environmental conditions in terms of steady state and transient thermal loads as well as high particle fluxes such as hydrogen, helium and neutrons. Candidate wall materials are beryllium, tungsten and carbon based materials like CFC (carbon fibre composite).

Tungsten is the most promising material for an application in the divertor region with very severe loading conditions and it will most probably also be used as PFM for DEMO. Hence, this work focuses on the investigation of the thermal shock response of different tungsten grades in order to understand the damage mechanisms and to identify material parameters which influence this behaviour under ITER and DEMO relevant operation conditions. Therefore the microstructure and the mechanical and thermal properties of five industrially manufactured tungsten grades were characterised. All five tungsten grades were exposed to transient thermal events with very high power densities of up to 1.27 GWm^{-2} at varying base temperatures between RT and 600 °C in the electron beam device JUDITH 1. The pulse numbers were limited to a maximum of 1000 in order to avoid immoderate workload on the test facility and to have enough time to cover a wide range of loading conditions. The results of this damage mapping enable to define different damage and cracking thresholds for the investigated tungsten grades and to identify certain material parameters which influence the location of these thresholds and the distinction of the induced damages. Furthermore the grain structure and the recrystallisation of the material have a significant influence on the thermal shock damage, especially the cracking pattern and surface roughening.

Beside the thermal shock damage mapping tungsten was also successively exposed to steady state high flux hydrogen-plasma and to cyclic thermal shock events simulated with an electron beam. The induced damages were investigated to determine if the exposure to hydrogen-plasma has an influence on the thermal shock response of tungsten. Special attention was paid to the thermal shock crack parameters such as distance, width and depth. The investigations showed that there is a significant influence on the damage behaviour of tungsten, especially if the tungsten targets are pre-loaded with hydrogen plasma. Beside the sequence of the exposure also the surface temperature during the plasma loading shows a clear influence on the thermal shock

behaviour. One of the most obvious changes is that due to the pre-exposure with hydrogen the thermal shock cracks are not limited to the electron beam loaded area anymore. They propagate through the only plasma loaded surface and even penetrate into the unexposed area at the edges of the tungsten targets. Additionally, all crack parameters decrease if the targets are pre-loaded with hydrogen plasma.

The combination of these results shows that the thermal shock response of tungsten as a PFM is very complex and depends on a wide range of parameters. It can be very well characterised by electron beam tests, but it has to be taken into account that these tests only simulate thermal loads without any influence of particle exposure. The influence of high flux hydrogen-plasma exposure on the thermal shock behaviour of tungsten can be estimated based on the results obtained from successive loading experiments. They give a good overview of the expected damages on tungsten as a PFM. These damages on the surface of the materials which are induced by high power densities and in combination with particle fluxes are detrimental for the operation of next step fusion devices such as ITER and DEMO and will have significant impact on the operational limits for large pulse numbers of 10^6 or more as expected in ITER.

Contents

1 Introduction **1**

1.1 Nuclear fusion 1

1.2 ITER design and operation conditions 3

1.3 Plasma wall interaction 6

1.3.1 Energy deposition by thermal loads 7

1.3.2 Particle fluxes 8

1.4 Plasma facing materials 9

1.5 Induced material damages 12

1.6 Simulation of fusion relevant conditions 13

1.7 Scope of work 14

2 Test facilities and material characterisation methods **17**

2.1 Mechanical properties 17

2.1.1 Tensile test 18

2.1.2 Impulse excitation method - Grindo Sonic 19

2.2 Thermal properties 21

2.2.1 Coefficient of thermal expansion - dilatometer 21

2.2.2 Specific heat capacity - differential scanning calorimetry 22

2.2.3 Thermal diffusivity - laser-flash method 23

2.3 Test facilities 25

2.3.1 JUDITH 1 25

2.3.2 Pilot-PSI 29

2.3.3 MARION 30

2.3.4 Nd:YAG laser 31

2.4 Post mortem analysis methods 33

2.5 Finite element method (FEM) 34

3 Thermal shock performance of different tungsten grades 35

3.1 Tungsten grades 35

3.1.1 Manufacturing and microstructure 35

3.1.2 Mechanical properties 44

3.1.3 Thermal properties 48

3.2 Experimental conditions 50

3.3 Simulation of temperature distributions 52

3.4 Results and discussion 55

3.4.1 Damage mapping 57

3.4.2 Investigation of thermal shock crack networks 71

3.4.3 Pulse number dependent thermal shock performance 77

3.4.4 Comparison of damages induced by laser and electron beam . . 79

3.5 Summary and conclusion 82

4 Influence of hydrogen on the thermal shock behaviour of tungsten 89

4.1 Tungsten grade 89

4.2 Experimental conditions 90

4.3 Results and discussion 93

4.4 Summary and conclusion 101

5 Overall conclusion and outlook 103

A Appendix: Hydrogen implantation in MARION 105

B Appendix: Tests at high temperatures in JUDITH 1 109

C Appendix: Detailed measurement results 113

C.1 Microstructure and density 113

C.2 Database for the calculation of the thermal conductivities 113

C.3 Arithmetic mean roughness of tungsten with different grain structures . 115

C.4 Crack parameters for tungsten with different grain structures 116

Bibliography 119

1 Introduction

One of the major challenges in the twenty-first century will be the energy research. Our immense current power consumption and estimations for the future energy needs in combination with the limited availability of fossil fuels will lead to serious problems in the nearer future. A second and even more serious problem is the environmental pollution and its consequences because of the massive use of fossil fuels. Also, there are several better applications for these raw materials than burning them.

The only alternatives to burning fossil fuels are renewables, fission and fusion. None of these alternatives can solve the problems by itself. Renewables today still have a poor gained energy to needed area ratio in comparison to our needs. For nuclear fission this ratio is much better but highly radioactive waste is produced albeit in very small amounts. Additionally there is a risk of a maximum credible accident caused by malfunction, terrorism or natural disasters. The third alternative is nuclear fusion. It is the least developed of the three technologies but the most promising [1].

This work will deal with nuclear fusion, from a materials science point of view.

1.1 Nuclear fusion

There are two different nuclear reactions, nuclear fission which is already used in present nuclear power plants to gain energy and nuclear fusion. Nuclear fusion means that multiple nuclei join and form a new heavier nucleus. If these nuclei are lighter than ^{62}Ni one will gain energy from this reaction because of the mass deficiency [2]. For example the nucleus of hydrogen is a single proton. When four of these protons are combined to a larger nucleus, they become more stable or in other words the binding energy increases as shown in figure 1.1. This causes the release of energy which is described by the following equation:

$$4\,{}^{1}_{1}\mathrm{H} + 2\mathrm{e} \longrightarrow {}^{4}_{2}\mathrm{He} + 27.05\,\mathrm{MeV} \tag{1.1}$$

A closer look at the atomic masses of H and He will show where the 27.05 MeV come from. The atomic mass of ${}^{1}_{1}$H and ${}^{4}_{2}$He is ca. 1.008 u and ca. 4.003 u, respectively. In reaction 1.1 the mass decreases by 0.7 %. The mass deficiency is $4.815 \cdot 10^{-29}$ kg which

corresponds to an energy of $4.333 \cdot 10^{-12}$ J = 27.05 MeV. This kind of fusion reaction powers the stars such as our sun and therefore allows us to exist [3].

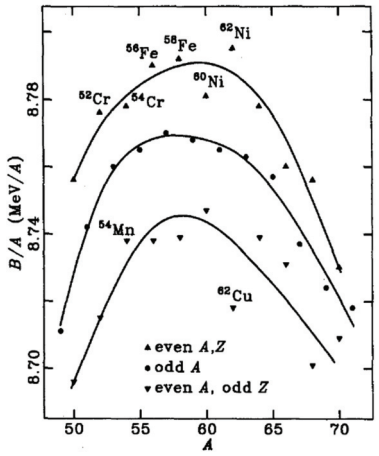

Figure 1.1: Binding energy of different nuclei. ^{62}Ni has the highest average binding energy. That means that nuclear fusion reactions of elements lighter and nuclear fission reactions of elements heavier than ^{62}Ni release energy [2].

It is a scientific challenge to initiate nuclear fusion because the nuclei have a positive charge and have to overcome the Coulomb repulsion. In a star, massive gravitational forces and core temperatures of around 10^7 K are the driving forces for fusion reactions. On earth, due to a lack of these gravitational forces, other ways have to be found.

Figure 1.2 shows the cross section of different fusion reactions. The most promising reaction, because of its high cross section at a relatively low temperature, is:

$$^2\mathrm{D} + ^3\mathrm{T} \longrightarrow {}^4\mathrm{He} + \mathrm{n} + 17.58\,\mathrm{MeV} \tag{1.2}$$

The fuel for this reaction are the hydrogen isotopes deuterium and tritium. They form an intermediate state ^{5}He (half life time ca. $5.5 \cdot 10^{-22}$ s) [4] which decays into a stable ^{4}He nucleus and a neutron with the kinetic energies of 3.5 MeV and 14.1 MeV respectively. Deuterium is stable and exists in natural hydrogen in a weight ratio of 1:5000. Tritium is not stable and decays with a half life time of 12.32 years into ^{3}He via β-decay. However, it can be produced via nuclear reaction from lithium, which can be found in the earth's crust. There are two possible reactions of tritium breeding shown in the following [3, 5]:

$$^6\mathrm{Li} + n \longrightarrow {}^4\mathrm{He} + ^3\mathrm{T} + 4.78\,\mathrm{MeV} \tag{1.3}$$

$$^7\mathrm{Li} + n \longrightarrow {}^4\mathrm{He} + ^3\mathrm{T} + \mathrm{n} - 2.47\,\mathrm{MeV} \tag{1.4}$$

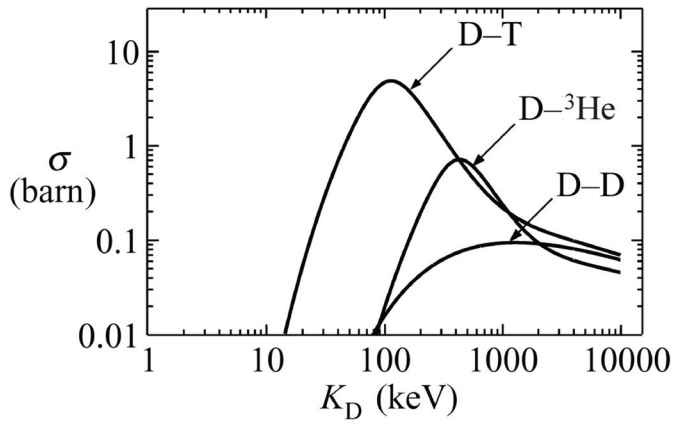

Figure 1.2: Fusion cross section (σ) of different nuclei as a function of their kinetic energy (K_D). The deuterium-tritium reaction has the highest cross section at the lowest temperature and is the most promising candidate for controlled fusion on earth [6].

The conditions at which fusion reactions (figure 1.2) are possible are not easily achieved. A particle plasma with a high temperature T, high particle density n and a long confinement time τ_E is necessary to initiate the fusion reaction. All these parameters are combined in the Lawson Criterion:

$$n \cdot \tau_E \cdot T \geq 6 \cdot 10^{28}\,\mathrm{s\,K\,m^{-3}} \tag{1.5}$$

There are two different methods to confine plasma with the above mentioned conditions, the so called inertial and magnetic confinement [7]. For the magnetic confinement the ignition conditions for fusion are a temperature T $\approx 10^8$ K, a particle density of n $\approx 2 \cdot 10^{20}$ m^{-3} and a confinement time $\tau_E \approx 3$ s. The confinement time τ_E for inertial fusion is much lower, because the particle density n will be higher. There are two different types of magnetic confinement reactor principles, the Tokamak and Stellerator [7]. In the following chapter 1.2 the Tokamak-principle will be briefly explained.

1.2 ITER design and operation conditions

One possibility to confine the fusion plasma is by magnetic fields and the most developed method is the so called Tokamak principle. The expression Tokamak is derived from the Russian *toroid-kamera-magnit-katushka*, which means *the toroidal magnetic chamber*. The magnetic fields that confine the plasma are generated by different coils. A toroidal field prevents the plasma from touching the surrounding vacuum vessel and is generated by poloidal coils. A central solenoid magnet acts like the primary

winding of a transformer, induces an electric current in the plasma. This provides an additional poloidal magnetic field component to stabilise the plasma. Because of this induced plasma current a TOKAMAK runs only in a pulsed operation mode. Figure 1.3 gives a schematic overview of magnetic coils and the plasma in a TOKAMAK [8].

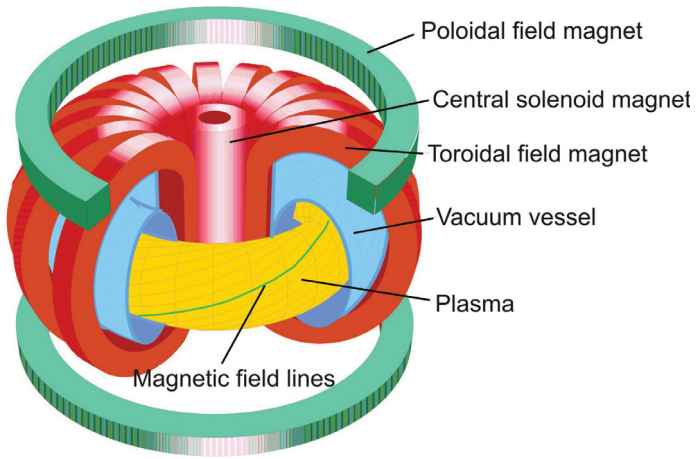

Figure 1.3: Schematic view of a TOKAMAK. The combination of poloidal, toroidal and solenoid coils create a more or less stable confined plasma. Because of the transformer principle it can only run in a pulsed mode [9].

In several devices like the Joint European Torus (JET), Tore Supra and DIII-D the feasibility of plasma confinement and a controlled fusion reaction on earth has been demonstrated. The next steps to the first commercial fusion reactor will be the experimental reactor ITER (latin: "way"; originally an acronym for International Thermonuclear Experimental Reactor) built in Cadarache, southern France, and, based on the obtained results, the demonstration power plant DEMO (DEMOnstration Power Plant).

ITER will base on the TOKAMAK-principle and its magnetic system will consist of several superconducting coils for the toroidal and poloidal fields. These coils, in combination with the also superconducting solenoid coil, will help to control the plasma inside the vacuum vessel. Part of this vacuum vessel will be multiple exchangeable components like test-modules for the first wall, diagnostic-modules, blanket-modules, divertor-cassettes and limiter. The exchange of these modules will happen via a remote-controlled robotic system. The materials that will be used here have to withstand high particle fluxes comprising electrons, ions and neutrons and have to remove high heat fluxes, especially at the first wall and the divertor. Figure 1.4 shows a schematic view of how ITER will look like. The vacuum vessel located in the centre is surrounded by a cryostat which guarantees the cooling of the superconducting coils [10–12].

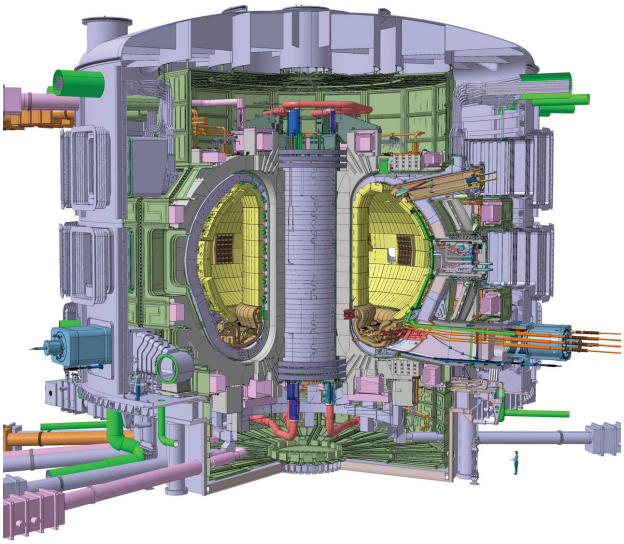

Figure 1.4: Schematic view of ITER. The vacuum vessel is located in the centre surrounded by the magnetic field coils and diagnostic-modules. These are surrounded by the cryostat that cools the superconductive coils. The whole machine will be the world's largest TOKAMAK with a height of 29 m and a diameter of 28 m [13].

The main parameters for ITER are listed in the following table 1.1:

Table 1.1: Main parameters of ITER [13, 14].

Heating power (input)	50 MW
Fusion power (output)	500 MW
Q = fusion power / heating power	≥ 10
Plasma major radius	6.2 m
Plasma minor radius	2 m
Plasma current	15 MA
Toroidal field	5.3 T
Plasma volume	≈ 840 m^3
Plasma mass	0.5 g
Neutron wall load	≤ 1 dpa
Pulse duration	≥ 450 s

One of the key components of ITER is the divertor. The major task of the divertor is to remove the "ash" from the plasma. This so called ash consists of He particles

from the fusion reaction (equation 1.2) and impurities of the plasma due to plasma wall-interactions. All of these particles will be "pumped down" by the divertor [10–12].

The whole divertor will consist of 54 divertor cassettes which will be located at the bottom of the vacuum vessel in toroidal direction. Figure 1.5 shows a schematic view of the ITER divertor.

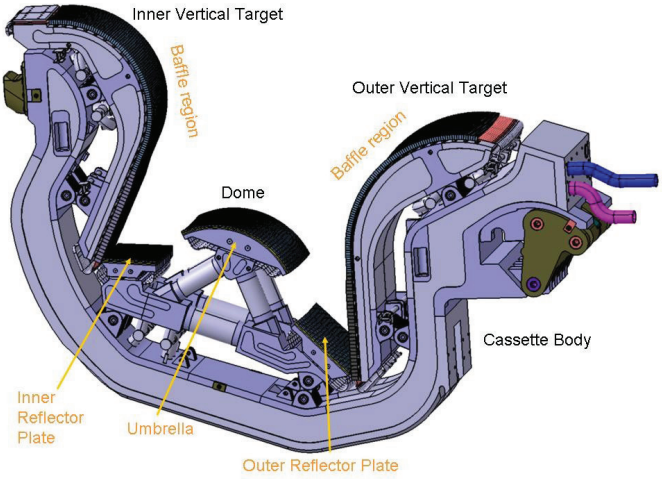

Figure 1.5: Schematic view of one divertor cassette (dimensions ca. $5 \times 2 \times 0.5$ m). Charged particles follow along the last closed magnetic field line and hit the divertor at the inner and outer vertical targets. The particles are neutralised and will be removed by vacuum pumps [13].

The above mentioned "ash" particles are electrically charged. These ions are guided along the last closed magnetic field line (LCMF) called the separatrix and the region of open field lines called scrape-off layer (SOL) to the divertor. Here the particles have direct contact to the material surface and are neutralised. After that they will be pumped out by vacuum pumps. Additionally these high particle fluxes deposit high heat loads on the PFMs especially in the divertor region. The loading of the divertor consists of three different kinds, thermal loads, thermal induced mechanical stresses and high particle fluxes. The combination of these three makes it very difficult to choose a material that can resist these conditions [15, 16].

1.3 Plasma wall interaction

In today's fusion devices like JET plasma pulses last for typically tens of seconds. In ITER a typical plasma pulse will last 450 s and continuous operation is intended. This

enormous increase of pulse length and the complex operation conditions in ITER will put high demands on the materials that will be used for the first wall and the divertor in terms of particle and heat loads. If one only takes into account the integrated wall load, a single ITER pulse is comparable to 1 year of JET operation which is the biggest TOKAMAK device in the world up to know [17].

1.3.1 Energy deposition by thermal loads

During a plasma discharge the surrounding materials have to absorb a certain amount of energy. The surface temperature increases throughout the discharge time until the energy deposition and dissipation by active cooling reach an equilibrium. During a normal ITER plasma pulse the expected heat fluxes for are ca. 0.5 MWm^{-2} for the first wall and up to 20 MWm^{-2} for the divertor. Moreover high particle fluxes will degrade the mechanical and thermal properties of the materials and make it even more difficult to choose the right material for this application (subsection 1.3.2) [18, 19].

Beside these steady-state conditions there are uncontrolled electromagnetic forces and fluctuations that lead to instabilities of the plasma confinement. Due to that there are intensive transient heat loads which can be classified in three main types. An overview of some events, their different power densities and durations, is given in figure 1.6.

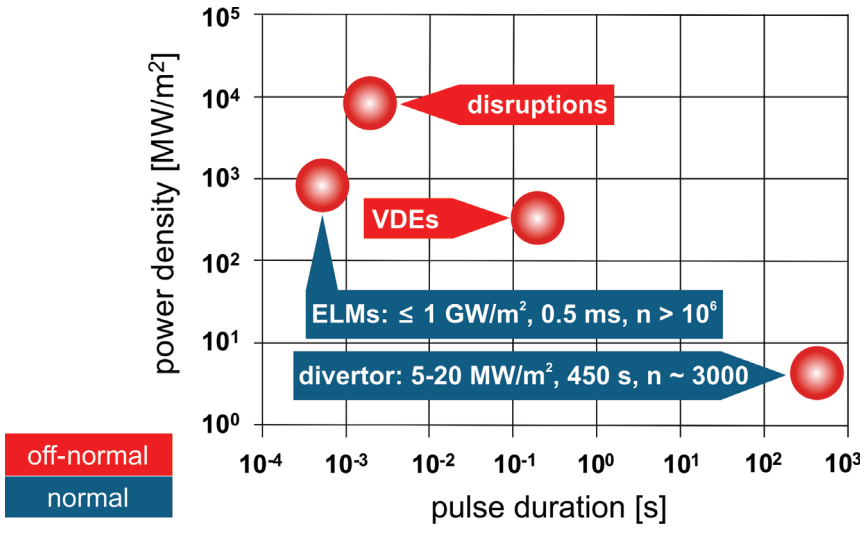

Figure 1.6: Overview of the power densities and durations of different events in ITER. They are divided in normal and off-normal events. The letter n indicates the number of events that the divertor or the first wall have to endure before they are replaced. Off-normal events have to be avoided during operation [20, 21].

Edge Localized Modes (ELMs) are so called normal transient events. They are common for H-mode (high confinement mode) plasmas and lead to a periodic energy loss at the plasma edge. The pressure gradient at the edge of the plasma exceeds a critical threshold and turbulent vortices can be observed. The pressure collapses and the edge plasma is lost to the SOL. It follows the magnetic field lines to the divertor and deposits its energy there [22].

ELMs can be classified into three different groups. Type 1 giant ELMs, Type 2 grassy ELMs and Type 3 small ELMs. On the basis of recent knowledge only type 1 ELMs are considered as the most problematic ones in terms of plasma facing material damage. They are also called "giant" ELMs. In ITER they are expected to deposit an energy of ca. 1 $\mathrm{MJm^{-2}}$ or more with a duration of 0.2 ms – 0.5 ms and a frequency of several Hz [23, 24]. However, mitigation techniques are explored and have to be utilised in ITER to decrease the deposited energy per ELM below the damage threshold.

Plasma disruptions are off-normal transient events. A disruption is a sudden breakdown of the plasma because of instabilities of the plasma confinement due to electromagnetic forces. After a fast thermal quench the plasma current rapidly breaks down. This can be divided into three phases: during the *precursor phase* distortion of the plasma and the magnetic field are induced. This leads to a rapid loss of thermal energy which is called *thermal quench*. Finally the plasma current rapidly decays. This phase is called *current quench*. Disruptions deposit a large amount of energy on the plasma facing materials of more than 30 $\mathrm{MJm^{-2}}$ within 0.1 ms and 3 ms [19, 24].

Vertical Displacement Events (VDEs) are also off-normal transient events. The events are caused by the loss of vertical control of the plasma confinement. This leads to a vertical drift of the plasma and a plasma contact to the wall. During that contact the plasma deposits an energy of ca. 60 $\mathrm{MJm^{-2}}$ on the wall. Such events have a duration between 100 ms – 300 ms. They can cause serious damage to the plasma facing materials and components [25, 26].

1.3.2 Particle fluxes

Materials that will be used in ITER have to withstand high particle fluxes. These fluxes can be divided in ion, electron and neutral fluxes. Both have similar values of $> 10^{24}$ $\mathrm{m^{-2}s^{-1}}$ at the plasma strike points in the divertor region. The ions follow open magnetic field lines of the separatrix and the SOL. Taking an ITER discharge of 450 s into account this flux leads to a total fluence of $> 10^{26}$ $\mathrm{m^{-2}}$ per discharge. The plasma density is around 10^{21} $\mathrm{m^{-3}}$ and the plasma temperature around 3 eV, which corresponds to an ion impact energy of ca. 15 eV, due to the acceleration between the plasma facing component (PFC) and the plasma, the so called plasma sheath potential. These loading conditions will lead to a significant heat up of the PFM surface of 200 °C

up to 1500°C in the divertor region and 200 °C up to 300 °C for the first wall [16,27–29].

In contrast to that it is much more complicated for ions to reach the first wall and the estimated fluxes are fraught with uncertainties. There are no open magnetic field lines which lead them to the first wall, but there is a small ion flux to the first wall based on neoclassical and anomalous transport [30]. Modelling results predict a neutral flux in the range of $> 10^{19}$ – 10^{21} $m^{-2}s^{-1}$ with energies between 8 – 300 eV. Indeed, the ion flux is 3 orders of magnitude smaller than in the divertor region even if long range transport through the SOL is taken into account [16].

Another major concern for PFCs in future fusion devices is the severe exposure to high energetic neutrons. The neutrons are produced during the fusion reaction (equation 1.2) with an energy of ca. 14 MeV and will cause drastic volumetric material damages. They will change the lattice structure of every material significantly and therefore cause significant degradation of material properties [31]. The expected neutron exposure of PFCs during ITER lifetime will be 1 dpa (displacement per atom) and several ten dpa for DEMO [20, 32, 33].

1.4 Plasma facing materials

The materials that will be used as plasma facing material (PFM) have to withstand enormous thermal, ion, electron and neutron fluxes as mentioned in the chapters above. This makes the selection of the PFMs one of the most important and difficult questions for a project like ITER or DEMO. Before a material can be used as a PFM a lot of parameters have to be taken into account and requirements have to be met [20, 29]. The most important ones are:

- high thermal conductivity
- high melting/sublimation point
- high resistance against neutron induced material degradation and activation
- high thermal shock resistance
- low tritium inventory
- low erosion rate/high sputter resistance
- plasma compatibility ⇒ low atomic number Z
- technical requirements: availability, cost, workability, joining

The contamination of the plasma with atoms of the PFM will lead to poor plasma performance due to high radiation losses which originate from electron excitation and

deexcitation. These radiation will escape the confinement and the kinetic energy of the fuel nuclei is lost. Especially for atoms with a high atomic number (Z), which are not completely ionised, this is an effective cooling mechanism and can even lead to a complete plasma breakdown [34].

In this context also safety and administrative limits have to be taken into account, which are not a concern in present TOKAMAKs. The safety limits of ITER for mobilised radioactive dust and tritium are 1 ton of global in vessel dust and 1 kg of tritium inventory, respectively. These limits have to be observed to avoid the evacuation of the neighbouring population in case of an accidental release. Based on these safety limits administrative limits have been derived to accommodate uncertainties of the available measuring methods. They were set to 670 kg of global in vessel dust and 700 g of tritium inventory [16].

There are only a few materials available today that meet most of these requirements. These materials are beryllium, tungsten and carbon fibre composites (CFC), which are foreseen for different parts of the inner wall. Beryllium will be used for the first wall, tungsten and/or CFC for the divertor. Where these components/materials are located in the vacuum vessel is depicted in figure 1.7 [34].

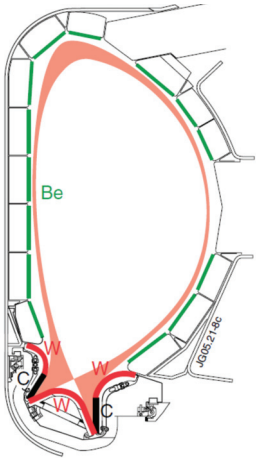

Figure 1.7: This picture shows a cross section of the ITER vacuum vessel. The first wall consists of 440 blanket modules, which will be made of beryllium (green). The divertor is at the bottom of the vacuum vessel. The dome and the vertical targets will be made of tungsten (red). CFC (black) will be used for the strike points of the separatrix [35].

Beryllium is a candidate for the first wall and has already been tested as a PFM in TOKAMAK device JET. It is also considered as a neutron multiplier for the tritium

breeding blankets and it will act as an oxygen getter to clean the plasma. In addition beryllium has a low atomic number (Z), which allows a relatively high concentration in the plasma, no chemical sputtering and a high thermal conductivity. The disadvantages of beryllium are the low melting temperature and high vapour pressure, a clear increase of the surface level (swelling) during transient events, the short erosion lifetime, the toxicity and the low resistivity against neutron radiation damages [36,37].

Another material that is already used in today's running fusion devices is graphite or the more advanced carbon fibre composite (CFC). In a machine like ITER it is only intended to be used for the divertor, specifically for the vertical target where the plasma has direct contact with the PFM. CFC is very suitable for that region because of its low Z, high thermal conductivity, high thermal shock resistance and its inability to melt. But the high tritium retention, the high chemical erosion and the severe degradation of the thermal conductivity after neutron irradiation limits the applicability of CFC [38].

The third material that will be used in ITER and which is currently the most promising candidate material for the first wall in DEMO and as PFM in future fusion reactors is tungsten. Especially the low erosion and sputtering rate, the low tritium retention and the combination of a high thermal conductivity and the highest melting point (3422 °C) of all metals makes tungsten one of the most suitable PFMs. However tungsten has also serious drawbacks like the high atomic number (Z = 74), a poor workability at low temperatures (high ductile to brittle transition temperature (DBTT)), recrystallisation and neutron embrittlement/activation [39,40]. The required amount of tungsten for the divertor in ITER is approximately 85 t, which is less than 10 % of the annual worldwide output of tungsten in 2006. This will fit the needs for ITER even if additional tungsten is necessary to exchange PFMs. Tungsten has a frequency of ~10 g/t in the earth crust, with the most important deposits in India, China, America and Austria. [41,42].

The main characteristics of the materials are summarised in table 1.2. An overview of the advantages and disadvantages is given in table 1.3.

Table 1.2: Main characteristics of beryllium, CFC and tungsten [29,34,43].

	Be	CFC	W
atomic number Z	4	6	74
melting point [°C]	1285	3500 (subli.)	3422
max. allowable concentration in the plasma	15%	12%	1 ppm
thermal conductivity at RT [$Wm^{-1}K^{-1}$]	184	200 – 500	183
thermal expansion coefficient at RT [10^{-6} K^{-1}]	11.6	≈ 0[1]	4.6

[1] in pitch-fibre direction

Table 1.3: Outline of the advantages and disadvantages of PFMs [36–39, 44].

Material	Advantages	Disadvantages
Be	• low Z • high thermal conductivity • no chemical sputtering • oxygen getter	• low melting point • toxicity • short erosion lifetime • low neutron radiation resistance • high swelling
CFC	• low Z • high thermal conductivity • high thermal shock resistance • no melting	• high erosion rate at high temperatures • high mismatch of CTE with Cu or steel heat sink • reduction of thermal conductivity after neutron irradiation • high tritium retention
W	• high melting point • high thermal conductivity • low erosion • low tritium retention • low swelling	• high Z • high DBTT • recrystallisation • neutron embrittlement/activation

1.5 Induced material damages

Due to high particle and heat fluxes a wide range of material damages are induced in the PFM, for example physical and chemical sputtering, radiation enhanced sublimation, crack formation, melting, thermal evaporation and, for CFC, sublimation. How severe the induced damages are and how the materials resist these damage mechanisms strongly depends on the kind of material.

For tungsten most of these damage mechanisms have no impact on the material. Physical and chemical sputtering by light ions like hydrogen have almost no influence because of the high activation energy [45], but they can cause lattice defects such as dislocations and vacancies [46]. Severe damages on tungsten are induced by neutron irradiation, transient and steady state heat loads. High neutron fluxes also cause lattice defects and lead to transmutation of tungsten atoms into rhenium, osmium and tantalum [47]. The combination of these effects leads to a change of thermal and mechanical properties of the material [48].

This work focuses on the damage behaviour of tungsten grades under high heat fluxes. A schematic overview of the expected damages in dependence on the power densities is given in figure 1.8. The fusion relevant heat loads are simulated by an electron beam or alternatively by other heating methods. The basic principle and the electron beam

test facility JUDITH 1 will be explained in chapters 1.6 and 2.3.1 in more detail. With an energy of 120 keV the electrons accelerated in JUDITH 1 penetrate 7 μm deep into the material according to Monte-Carlo simulations [49]. At very low power densities no damages or surface modifications are induced. If the power density is increased the so called damage threshold is reached. Above this threshold the material surface shows roughening and/or swelling. These surface modifications are a result of plastic deformation due to compressive stresses induced in the loaded area during the heating process because the colder surrounding material prevents the grains from expanding. During the cooling process the grains shrink again and the compressive stresses are converted into tensile stresses. When the tensile stresses are higher than the tensile strength of the material, cracks will be formed. This happens at power densities above the cracking threshold. At higher power densities the melting threshold is reached. Parts of the surface start to melt and resolidify during the cooling process (melting point of tungsten: 3422 °C).

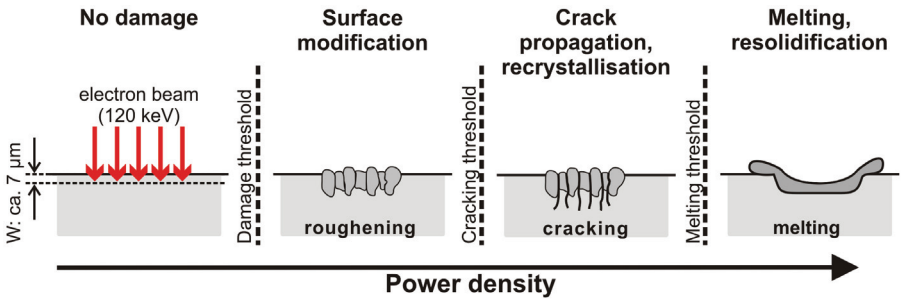

Figure 1.8: Expected material damages induced by transient heat loads on W in dependence on the power density. The material is heated up by an electron beam. At power densities below the damage threshold no damages or surface modifications occur. Above this threshold roughening starts and is combined with cracking of the material when the cracking threshold is exceeded. At very high power densities surface parts of the material start to melt.

1.6 Simulation of fusion relevant conditions

The choice of an appropriate PFM in combination with a convenient PFC design is an important task of today's R&D. Therefore test methods and facilities are necessary to simulate fusion relevant loading conditions and to characterise the response of PFMs. The most common test facilities/methods for fusion relevant conditions are electron, neutral/ion and laser beam facilities [50–52], but occasionally arc discharge facilities and infrared heaters are used. All of these testing methods have advantages and drawbacks, which have to be taken into account during the planning, performance and interpretation of these tests.

For the simulation of thermal shock events like ELMs, VDEs and disruptions (see 1.3.1) high power densities, fast pulse rise time, short pulse duration and frequency are important. Appropriate test facilities are electron beam guns and pulsed lasers. They are capable of short pulse rise time and duration in combination with high pulse frequencies. A major problem is the defined power density input into materials because of the material and surface dependent absorption of electrons and photons. Another issue that has to be taken into account is the energy and material dependent penetration depth of electrons, which leads to a volumetric loading instead of a surface loading within a thin layer. These issues will be explained and discussed in more detail in chapter 2. Another possibility of simulating fusion relevant conditions is the use of plasma accelerators. These devices provide the most realistic conditions because they simulate not only the thermal loads like electron beam guns and lasers but also particle fluxes. One major drawback is the low repetition rate because of the cool-down period of the plasma generator.

Beside the thermal shock events it is also important to simulate steady state heat loads. This can be done by electron/ion beam or plasma facilities and by infrared or ohmic heating systems which guarantee a homogeneous heating even of large samples. They are also stable over a long period of time and enable the sample to reach thermal equilibrium. These tests give information on the heat dissipation of materials and whole components before and after stationary or cyclic thermal shock loading or neutron irradiation tests.

1.7 Scope of work

The realisation of a thermonuclear fusion reactor puts high requirements on material properties. Materials that will be used for the first-wall and the divertor components of future fusion devices, like ITER and DEMO, have to withstand extreme conditions as mentioned in previous sections. To guarantee reasonable lifetime of a fusion device in terms of safety and economy, PFCs have to withstand the environmental conditions long enough without severe material property modifications or damages. Especially the combination of steady state heat loads, transient heat loads with fast repetition rates and very high particle fluxes are a big challenge for every PFM (see section 1.3).

There are only three materials, namely beryllium, tungsten and CFC, which are considered to have a sufficient lifetime under these severe environmental conditions (see section 1.4). The most promising material for the divertor in ITER and for further applications as PFM in DEMO and future fusion devices is tungsten. Its main advantages are its high thermal conductivity, high melting temperature, low tritium inventory and low erosion rate. In contrast to that, tungsten has also some drawbacks like the poor mechanical properties at low temperatures (high DBTT), a high Z and a remarkable

neutron-irradiation induced activation. Tungsten and its behaviour as a PFM becomes even more important due to recent considerations to change the ITER divertor design, which address the replacement of a CFC/tungsten combination (cf. figure 1.7) by a full tungsten divertor right from the start of ITER operation.

A serious concern about today's industrially available tungsten grades is their resistance against fusion relevant thermal loads. This comprises on the one hand thermal fatigue damage due to cyclic steady state heat fluxes and on the other hand transient thermal loads like plasma disruptions or ELMs. Especially during a thermal shock event cracks and crack networks are expected to form due to thermally induced stresses. How their pattern is influenced by microstructure, material properties and base temperature. Furthermore high particle fluxes may also have an influence on the damage behaviour. A detailed knowledge of induced damages and their pattern can help to prevent or at least reduce material erosion and component degradation during the operation of ITER. The risk of a plasma break down would be reduced and the lifetime of PFC could be increased. Therefore this work focuses on the thermal shock behaviour of tungsten up to very high power densities being still below the melting threshold under varying conditions, in order to understand its thermal shock response, and considers two topics:

The first comprises the testing, qualification and quantification of the thermal shock behaviour of different tungsten grades to achieve a better understanding of the underlying damage mechanisms and get an estimation of tungsten degradation under transient thermal loads with high power densities (chapter 3). In compliance with this aim, five industrially produced tungsten grades/alloys are characterised according to their microstructure, mechanical and thermal properties. Furthermore these grades are exposed to thermal shock events at different base temperatures, which are applied by the electron beam facility JUDITH 1 (Juelich Divertor Test Facility in Hot Cells) in order to simulate ELM like loading conditions. Subsequently the thermal shock response of all tungsten grades is compared to identify significant and even slight differences in their damage behaviour. The identified differences are related to the determined material properties and as a result it is possible to define the influence of specific material parameters on certain aspects of the thermal shock behaviour of tungsten.

The second topic is the influence of high flux hydrogen-plasma on the thermal shock behaviour of tungsten aiming for the determination of mutual influences between exposure by high-flux hydrogen-plasma and thermal shock loading as well as of important loading parameters (chapter 4). It was shown in previous experiments [53–55] and in chapter 3 that transient thermal loads induce a wide range of damages like melting, enhanced erosion, thermal shock crack networks and surface modifications on the loaded tungsten surface. To achieve more realistic testing conditions and to quantify the influence of high flux hydrogen-plasma on the damage behaviour, tungsten is exposed to both loading conditions successively.

Finally the results of both parts are combined to give an overview of expected material modifications and damages especially for high thermal loads during ITER operation and how additional hydrogen exposure will affect that behaviour. If these damages are tolerable or can be prevented by improving material parameters is also a part of the final discussion in chapter 5.

2 Test facilities and material characterisation methods

During this work a lot of different measuring instruments had to be used to determine thermo-mechanical and thermo-physical material properties. Also an electron beam facility, a laser and linear plasma devices were used to simulate thermal shocks which are comparable with loads expected in future fusion devices. The facilities are located at the Belgian Nuclear Research Centre (SCK•CEN) (tensile tests in subsection 2.1.1), the Dutch Institute for Fundamental Energy Research (DIFFER) (Pilot-PSI in subsection 2.3.2) and the Forschungszentrum Jülich (FZJ). In this chapter not only the test and characterisation methods will be explained but also machine specific characteristics which are important for the tests and experiments in chapter 3 and 4.

2.1 Mechanical properties

Solid components can be deformed elastically and plastically. Characteristic for elastic deformation is that after mechanical loading the material returns to its initial state without any lasting deformation. For small strains there is a linear dependency between stress and strain described by Hooke's law. Metals can usually be deformed beyond the elastic behaviour resulting in plastic deformation of the material. This kind of deformation is irreversible and causes a permanent elongation/contraction after unloading.

The elastic and plastic properties of a material are very important parameters for the design and lifetime assessment of technical applications. A common technique to determine the mechanical properties of a material is the tensile test (subsection 2.1.1). The measured stress-strain diagrams provide information like yield strength, ultimate tensile strength (UTS) and fracture strain. A drawback of this method is that the samples are destroyed during the test and only one diagram at defined conditions is obtained. Therefore the method is very time and cost intensive. A cheaper and non-destructive method is the impulse excitation technique (subsection 2.1.2). This method uses the resonance of a material to calculate the Young's modulus, Shear modulus and Poisson's ratio.

2.1.1 Tensile test

The tensile tests were carried out in close collaboration with the fusion materials group at SCK•CEN, Mol, Belgium, using a high temperature vacuum furnace set-up. With this set-up it is possible to measure stress-strain diagrams at different base temperatures. The operation temperature range is quite wide with a minimum at RT and a maximum of 2300 °C.

The furnace consists of mesh heating elements and radiation heat shielding made from the refractory metals tungsten and molybdenum with a size of 100 mm in diameter and a height of 203 mm. The maximum work chamber size has a diameter of 76 mm and a height of 127 mm. All of this is located in a vacuum vessel which can be pumped down to a typical working pressure of $5{\cdot}10^{-2}$ mbar or be flooded with inert gas like nitrogen, helium or argon to a standard positive pressure of ca. 140 mbar during operation. There are also eleven thermocouples mounted at different positions of the device to ensure a controlled heating and homogeneous temperature distribution inside the furnace and the specimen. Figure 2.1 gives an overview of the high temperature vacuum furnace and the positions of the thermocouples [56].

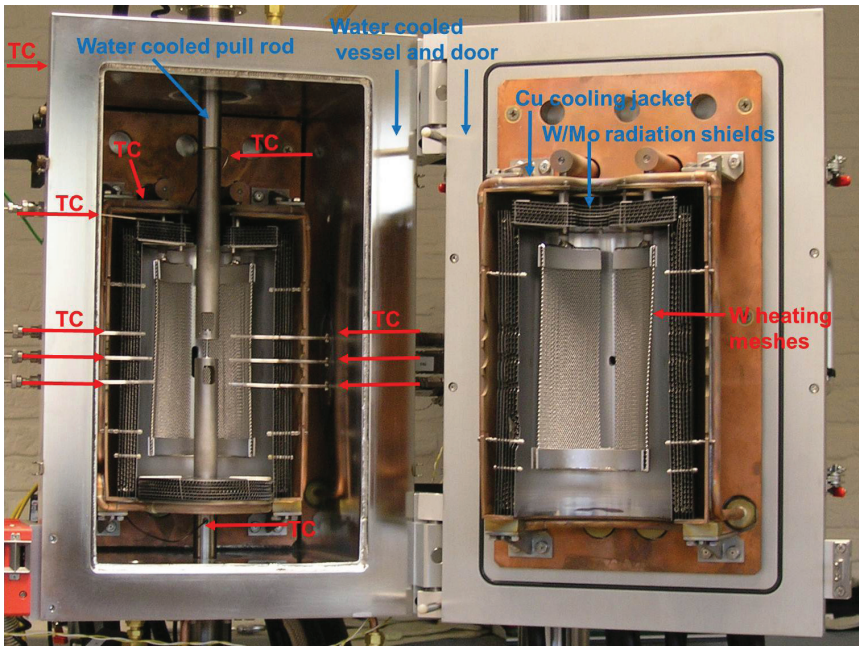

Figure 2.1: Picture of the high temperature vacuum furnace. All important parts are indicated with red or blue arrows, like the thermocouples (red arrows TC), the cooling circuits (blue arrows) and the heating mesh (red arrow) [56].

The radiation shields are surrounded by a copper cooling jacket to make sure that the outside temperature of the vacuum vessel never exceeds 60 °C. Especially at high temperatures above 800 °C the temperature uniformity is very good and the differences are below 20 °C over the mechanically loaded area. For lower temperatures the temperature uniformity becomes worse particularly in vacuum because the radiation heating is less efficient. In contrast to that the temperature stability is always around ± 3 K [56].

For tensile tests at different temperatures appropriate pull rod designs have to be used and in view of materials and joining techniques also the pull rods have to be water cooled. Because of the extreme differences in temperature a two part design was chosen for the load strings. The upper pull-rod is to be connected to the load frame via a draw bar/pilgrim nut and the lower load string is connected to the actuator via the load-cell. Tensile tests can be performed with strain rates between 10^{-4} – 10 s^{-1}. A picture of a typical tensile test specimen showing also all relevant dimensions is plotted in figure 2.2 [56].

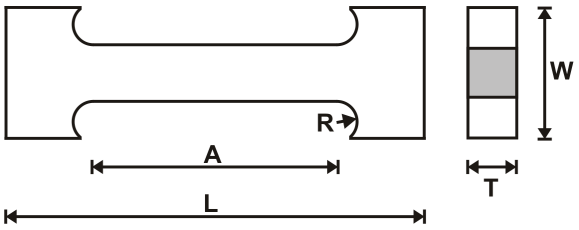

Figure 2.2: Typical tensile test specimen geometry with the maximum dimensions of L = 26 mm and W = 8 mm. The gauge thickness is T = 3 mm and the gauge length is A = 15 mm. The curvature radius is R = 1.5 mm.

2.1.2 Impulse excitation method - Grindo Sonic

The impulse excitation method is a non-destructive technique that covers a dynamic determination of the elastic properties of materials. This method is in principle suitable for all elastic materials as long as their internal damping does not exceed a certain value. The procedure uses light external mechanical impulse which excites the sample material to transient natural vibration. This mechanical vibration is recorded by a transducer and analysed during the subsequent free relaxation by corresponding software. There are no special specimen dimensions required. They can vary between small bars of several millimetre and large beams with a weight of several hundred kilogrammes [57].

The test itself lasts only a few seconds and only minute stresses are applied to the specimen, hence the test is non-destructive. The moduli measured are those at the

origin of the stress-strain diagram and therefore give the intrinsic moduli. There are different formulas to calculate the Young's modulus from the vibration frequency. For a specimen with a rectangular cross section the formula is [58]:

$$E = 0.9465 \left(\frac{m\nu_n^2}{b}\right) \left(\frac{l^3}{h^3}\right) T_1 \tag{2.1}$$

with the following formula symbols:

E = dynamic Young's modulus [Pa]
m = mass of the test specimen [g]
ν_n= vibration frequency [Hz]
b = width of the test specimen [mm]
l = length of the test specimen [mm]
h = height of the test specimen [mm]
T_1= correction factor

The correction factor has to be added to take the finite thickness of the specimen into account (Poisson's ratio). For specimen with aspect ratios of l/h > 20 the correction factor is given by:

$$\begin{aligned} T_1 =& 1 + 6.585(1 + 0.0752\mu + 0.8109\mu^2)(l/h)^2 - 0.868(l/h)^4 \\ & - \left(\frac{8.34(1 + 0.2023\mu + 2.173\mu^2)(l/h)^4}{1 + 6.338(1 + 0.1408\mu + 1.536\mu^2)(l/h)^2}\right) \end{aligned} \tag{2.2}$$

where μ is the Poisson's ratio.

The impulse excitation experiments to determine the Young's modulus of tungsten specimens were carried out with the GrindoSonic MK5i device. With this device it is possible to measure temperature dependent modulus values up to 1200 °C between 0.05 and 900 GPa. The temperature is controlled by two type K thermocouples and the temperature ramp rate is selectable from 1 °C to 300 °C per hour. It is also possible to perform the test under inert gas atmosphere or vacuum, but the gas supply and vacuum pumps are not yet available.

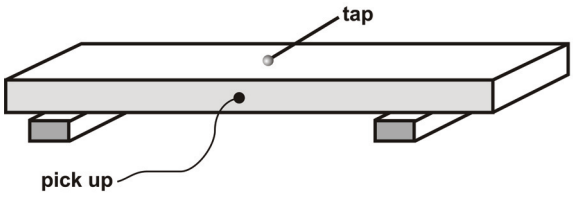

Figure 2.3: Schematic picture of the experimental design of the GrindoSonic MK5i instrument. The mechanical impulse is induced by a tap and recorded by a transducer. Typical sample size is 150 × 40 × 10 mm^3.

The typical samples that are tested in this device are bar shaped samples because for this shape the fundamental flexural mode of vibration will have the maximum deviation in the centre and at both ends. A bar shaped sample should have the dimension relations b/l < 1/3. Otherwise the sample supports can not be considered as straight lines and the sample mounting would become very complicated. The mechanical impulse is induced by a tap and recorded by a transducer in the middle of the sample to avoid a tilting movement of the sample (figure 2.3). It is essential that the exiting impulse is light and elastic which means that the impacting object must bounce back immediately. Therefore it is a spherical object at the end of a thin flexible stem. Size and material for the "ball" are chosen considering the size and material of the sample. The shorter, thicker and harder the material, the harder the material for the "ball" has to be [59].

2.2 Thermal properties

Detailed knowledge about the thermal properties of a material is essential before it can be used for applications where high thermal loads and steep temperature gradients are expected such as presented in section 1.3. Based on this severe conditions the most interesting parameters are the coefficient of thermal expansion (CTE), the specific heat capacity (c_p), the thermal diffusivity (a), the density (ρ), and the thermal conductivity (λ). The CTE is a parameter that describes how the size of an object changes with temperature and therefore provides the basis to estimate thermally induced internal stresses in material composites. Furthermore the materials have to conduct the heat fast enough from the surface to the cooling tubes to prevent overheating of the surface. This ability is represented by the thermal conductivity, which can be calculated by c_p and a via the formula $\lambda(T) = a(T) \cdot c_p(T) \cdot \rho(T)$, where ρ is the material density.

2.2.1 Coefficient of thermal expansion - dilatometer

The CTE was measured by the vertical double pushrod dilatometer L75V of the Linseis Messgeräte GmbH (figure 2.4). It can operate in a temperature range from RT to 1600 °C under argon inert gas atmosphere with a flow rate of 4.8 l/min. The samples are arranged as leverage (="pushrod") and the displacement during the heating process is measured by an inductive position sensor. Hereby the change of the CTE can be measured with an accuracy of $0.2 \cdot 10^{-6}$ K^{-1}. All data points are collected and important parameters like heating, cooling, atmosphere etc. are controlled by a data acquisition system which is connected to the device. Special attention has to be paid to the sample fabrication. The accuracy of the measurement strongly depends on the plane parallelism of the cross sectional areas of the samples where they are clamped in the dilatometer.

Polycrystalline aluminium oxide (Al_2O_3) samples are used as a reference material and

to control the measured data. The reference material and the materials to be measured are mounted in the dilatometer (see figure 2.4b for CFC) and loaded with ~500 mN. They are heated with a rate of 3 K/min and cooled down with 8 K/min to the target values.

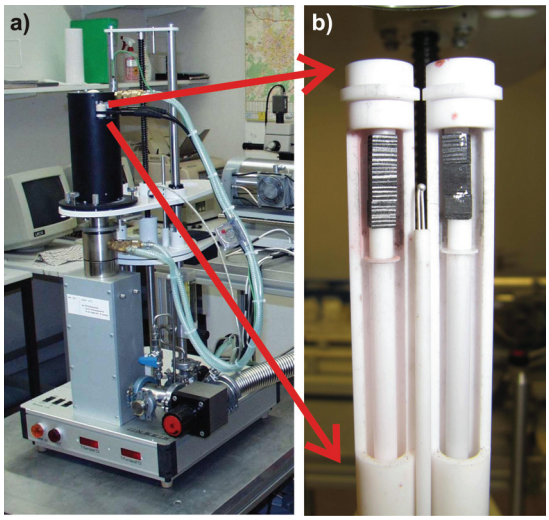

Figure 2.4: a) Picture of the vertical double pushrod dilatometer L75V by Linseis. b) Two CFC samples mounted in the dilatometer.

During the experiment the length variation ΔL and temperature difference ΔT are recorded. These values in combination with the original length of the samples L_0 allow to calculate the CTE α as following [60]:

$$\alpha = \frac{1}{L_0}\frac{\Delta L}{\Delta T} \tag{2.3}$$

2.2.2 Specific heat capacity - differential scanning calorimetry

The differential scanning calorimetry (DSC) is a method to determine the temperature dependency of the specific heat capacity, which is the amount of energy required to change the temperature of a material by a given amount. This thermoanalytical method is based upon the different rate of heat flows which are necessary to increase the temperature of a sample and a reference material depending on temperature and/or time. Thereby it is important that sample and reference material are heated to the same temperature [61].

The measurements were performed with the high-temperature device “DSC 404C” by NETZSCH - Gerätebau GmbH (picture 2.5). This facility covers an operative temper-

ature range between -60 °C and 1400 °C. It is also possible to perform measurements under inert gas atmosphere to prevent sample materials from oxidation. The change of mass that accompanies the oxidisation process would lead to a distortion of the measured values.

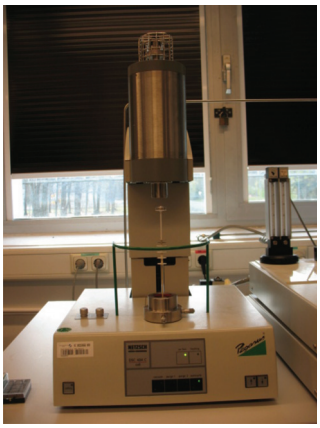

Figure 2.5: Picture of the High-Temperature Differential Scanning Calorimeter DSC 404C by Netzsch.

During an experiment the required amount of energy to keep sample and reference materials at the same temperature is recorded and assigns every temperature a difference in heat flow rate. From these data and the combination of heat flow (= q/t) and heating rate (= ΔT/t) the heat capacity C can be calculated [62]:

$$C = \frac{q}{\Delta T} \tag{2.4}$$

If the mass of the sample (m) is know, the specific heat capacity at constant pressure (c_p) can be calculated using the equation [62]:

$$c_p = \frac{q}{m \cdot \Delta T} \tag{2.5}$$

2.2.3 Thermal diffusivity - laser-flash method

With the laser-flash method the thermal diffusivity of a material can be determined in a short time and up to high temperatures. It is convenient for isotropic, anisotropic and composite materials such as metal-to-metal bonds [63, 64].

The schematic view of the used laser-flash device is shown in figure 2.6. A neodymium-glass-laser with a pulse length between 0.1 ms and 2 ms and a wavelength of 1064 nm is used to heat one side of a disk shaped sample and the sample temperature is measured by Pt/PtRh-thermocouples. At the same time the temperature development of

the back side of the sample is recorded by an infrared sensor. An appropriate sample should have a diameter between 6 mm and 13 mm and a height of 1 to 6 mm. In addition, the measurement accuracy strongly depends on the plane parallelism of the sample front and back side. The tolerance for this is in the range of ±5 %. Tests can be performed at temperatures between RT and 1500 °C under vacuum (0.1 Pa), inert gas (helium) or oxidising atmosphere. Before and after an experiment a reference stainless steel sample is tested to make sure that the device is working properly.

Based on this experimental set-up the thermal diffusivity can be determined by the temperature rise of the sample's back side. The relation between the thermal diffusivity a and the temperature rise is given by the equation:

$$\mathrm{a} = \frac{K_x D^2}{t_x} \tag{2.6}$$

with D as sample thickness and the correlation constant K_x. The index x stands for the percentage of time until the maximum temperature is reached. If the half time of this period is taken into account equation 2.6 changes to [65]:

$$\mathrm{a} = \frac{0.139 \cdot D^2}{t_{1/2}} \tag{2.7}$$

The thermal conductivity can be calculated by the product of the specific heat capacity (c_p(T)), the thermal diffusivity (a(T)) and the density (ρ(T)) [60].

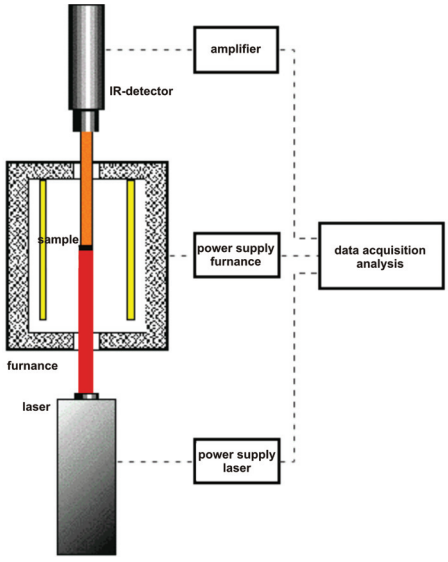

Figure 2.6: Schematic view of a laser-flash device.

2.3 Test facilities

A rather detailed qualification programme is required to make sure that tungsten or any other candidate materials (see 1.4) can be used as a PFM and can withstand the in section 1.3 mentioned environmental conditions for an appropriate operation time. There are three different methods to simulate fusion relevant conditions as already mentioned in section 1.6. All four test facilities, described in this section, are based on one of these methods. Special attention is paid to the electron beam facility JUDITH 1 (Jülicher Divertor Test Facility in Hot Cells), and the interaction of electrons with matter, because most of the experiments described in chapter 3 and 4 were performed with it.

2.3.1 JUDITH 1

The electron beam facility JUDITH 1 is located in the hot cells at FZJ. It is capable of simulating fusion relevant steady-state heat loads as well as transient events such as ELMs, VDEs and plasma disruptions (see 1.3.1). Samples vary between large actively cooled divertor modules for thermal screening or fatigue tests, small samples for thermal shock tests to investigate the induced material damages like cracks and material erosion and neutron irradiated components. A schematic overview and a photograph of JUDITH 1 are shown in figure 2.7.

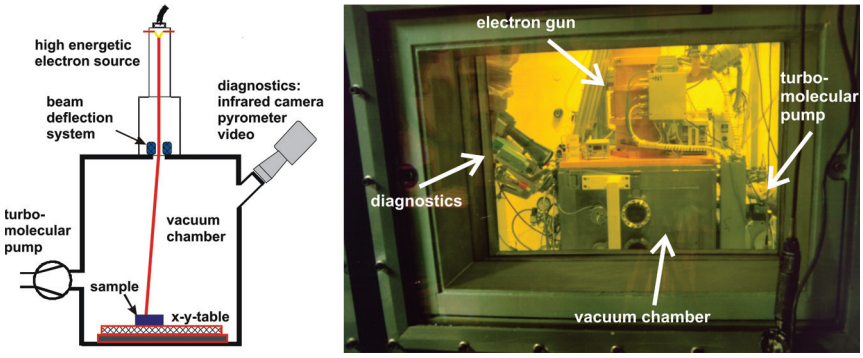

Figure 2.7: Left: schematic view of the electron beam facility JUDITH 1 with diagnostic systems. A thermal shock sample is mounted on a xyz-table and scanned by the electron beam. Right: Photograph of JUDITH 1 located in the hot cells.

JUDITH 1 consists of a modified electron beam gun with a power of 60 kW, a vacuum chamber with the dimensions of 800 × 600 × 900 mm^3 and several diagnostic devices such as an infrared pyrometer, two colour pyrometers, fast pyrometers, thermocouples for the cooling water, calorimetry and material samples as well as infrared and visual cameras. The electron beam is generated with a tungsten cathode that emits free

electrons. These are accelerated with a voltage $\leq$ 150 kV and focused by magnetic coils to a beam diameter (FWHM) of 1 mm. Deflection coils are used to scan the samples with frequencies of up to 100 kHz in x- and y-direction. Before an electron beam can be generated the whole facility has to be evacuated. The normal working pressure for the beam generator system is 10^{-5} mbar and for the sample chamber 10^{-4} mbar [66]. A schematic view of the beam path for an electron pulse of 1 ms is given in figure 2.8.

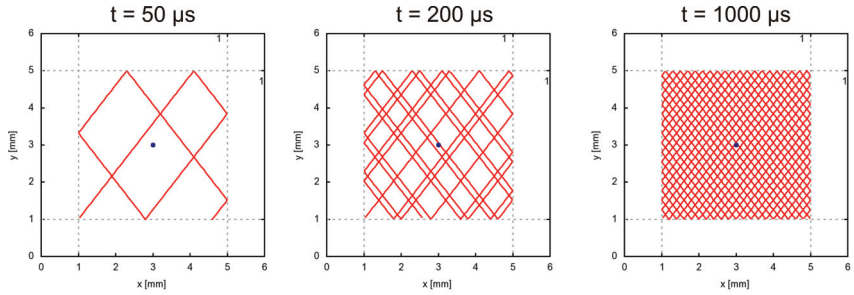

Figure 2.8: Calculated electron beam path of a 1 ms pulse in JUDITH 1 after 50 μs, 200 μs and 1000 μs. The loaded area (4 $\times$ 4 mm^2) is scanned with frequencies of 40 kHz and 31 kHz in x- and y-direction, respectively. These high and odd frequencies were chosen to achieve a homogeneous loading.

These high frequencies in combination with the choice of odd frequencies for both directions ensure the best possible homogeneous loading. The maximum beam deflection in xy-direction that can be achieved with this system is $\pm$5 cm at the nominal acceleration voltage. From this follows a loaded area of up to 100 cm^2. Short pulses between 1 ms and 100 ms for the simulation of thermal shock events are generated by a charged condenser with a pulse rise and fall time of 100 μs. In contrast to that a continuous surface scanning is also possible. Actively cooled components are connected to the internal cooling circuit of JUDITH 1, which cools with water at RT and a maximum flow rate of 60 l/min [66].

The beam power depends on the acceleration voltage U_a and the beam current I. During normal operation the acceleration voltage is fixed at 120 kV. This results in a electron energy of 120 keV and a penetration depth of ~7 μm in tungsten (95 % of the absorbed electron beam energy is deposited) [67, 68], which causes volumetric heating within a thin layer instead of pure surface heating. The beam power is varied via the current ($\leq$ 400 mA). Furthermore these two parameters have an influence on the mean power density P_{abs} absorbed by the sample material. It can be calculated using the equation:

$$P_{abs} = \frac{U_a \cdot I \cdot \epsilon}{S} \tag{2.8}$$

with S for the loaded surface area and ϵ for the electron absorption coefficient of the sample material. This absorption coefficient strongly depends on the material and the electron interaction with it. A schematic overview of the interaction process is given in figure 2.9.

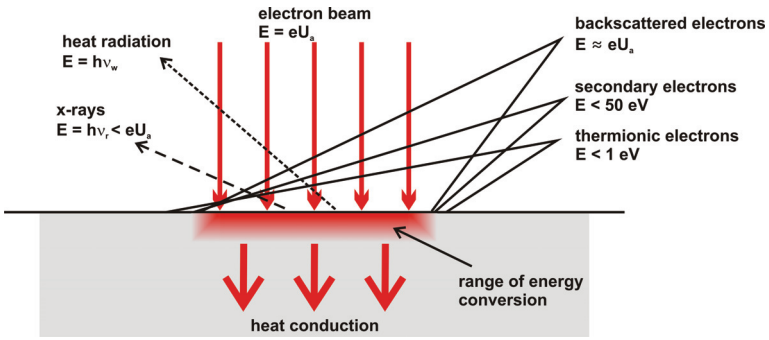

Figure 2.9: Overview of the interaction of accelerated electrons with matter according to [67]. The range of energy conversion depends on the incident electron energy eU_a. Weakening factors of the energy absorption are backscattered and secondary electrons.

The electrons hit the target material with a kinetic energy of eU_a. This kinetic energy is converted into heat and excitation energy of the target atoms. The range of energy conversion depends on the incident electron energy eU_a [67, 68]. However, there are weakening factors, which make this energy deposition less effective. Backscattered or reflected primary electrons interact with target atoms via inelastic collisions. They deposit only a small amount of their kinetic energy and leave the target material usually after one collision ($E \approx eU_a$). Primary electrons, which deposit most of their incident kinetic energy in the target material, induce the emission of secondary electrons. These secondary electrons can diffuse to the surface and leave the material with an energy of ≤ 50 eV. The last group are thermionic electrons, which leave the material due to the high temperatures generated. They carry an energy of up to 1 eV and are negligible in comparison to the backscattered and secondary electrons as well as the energy loss due to heat radiation and x-rays [68].

In order to quantify the energy loss all samples are grounded via a 100 Ω resistor and the current through the samples is measured. For tungsten samples these measurements lead to an electron absorption ceofficient ϵ (I_{abs}/I_{inc}) of 0.46. This value deviates a lot from the absorption coefficient obtained by Monte-Carlo-simulations (0.55) [49] and found in literature (0.5 and 0.62) such as [67] and [69]. An experiment was designed and performed to determine where this deviation of the absorption coefficient of tungsten comes from.

The electron absorption coefficient of tungsten

The major part of the discrepancy between the electron absorption coefficient obtained by current measurements and the simulation/literature values of 20 % is assumed to be a result of the neglection of emitted secondary and thermionic electrons. These electrons have no or only a small influence on the energy loss but they do not contribute to the current through the sample and lead therefore to a measured I_{abs}/I_{inc} of 0.46 while the material absorbs much more energy.

The secondary and thermionic electrons have to be collected and added to the current through the sample to proof this assumption. Therefore thin gold foils were tauten on a brass and a ceramic ring (inner diameter: 12 mm; height: 2 mm) and placed on a tungsten sample as shown in figure 2.10. The foil had to be very thin to ensure that only a negligible amount of primary and backscattered electrons is absorbed. Additionally, the foil had to be a conductor to collect the secondary electrons and add them to the sample current. Due to that a pure gold foil with a thickness of 100 nm and an absorption of fast electrons below 5 % was chosen [68]. Brass was chosen because it is a conductor and the same material as the sample holder of JUDITH 1. The ceramic ring was used as a control to quantify the amount of primary electrons absorbed by the gold foil.

For the experiment the normal operation conditions of JUDITH 1 were used. The primary electrons impinge perpendicular to the target surface with an energy of 120 keV. W-UHP (Ultra high purity tungsten) with a purity of 99.9999 wt% was used as target material. The current through the grounded sample flowed through the sample holder and was measured via a 100 Ω resistor. It was monitored and recorded by an oscilloscope. Each set up (without foil, with foil on ceramic and with foil on brass ring) was exposed to electron beam pulses with a duration of 1 ms and an incident current I_{inc} of 50 mA.

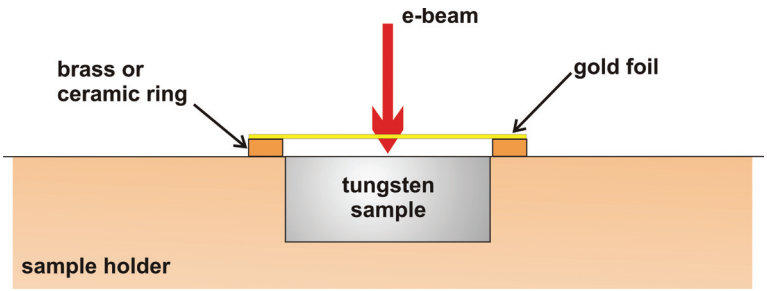

Figure 2.10: Scheme of the experimental set-up to determine the electron absorption coefficient of tungsten. A gold foil on a 2 mm high brass or ceramic ring is tauten over a tungsten sample to collect the secondary and thermionic electrons.

The current measurements through the tungsten targets for all three set ups are shown in figure 2.11. The response threshold of the oscilloscope is 13.54 mA. Due to that the signal does not start at 0 mA. The results show that the gold foil has a significant effect. Without gold foil the average current is (23.31 ± 0.43) mA (figure 2.11a) which increases to (28.57 ± 3.58) mA and (26.8 ± 1.16) mA with gold foil on ceramic and brass ring, respectively (figure 2.11b and c). With an incident current of 50 mA this results in absorption coefficients ϵ of 0.47 ± 0.01, 0.57 ± 0.07 and 0.54 ± 0.02, respectively.

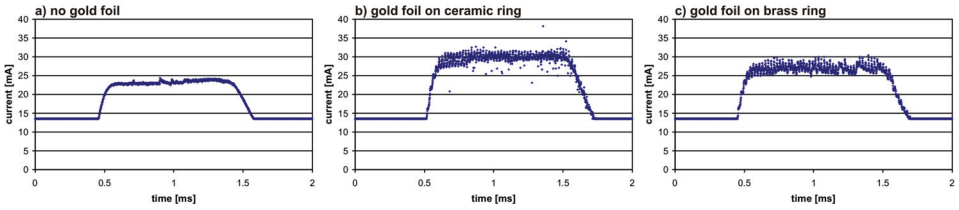

Figure 2.11: Results of the current measurements through the tungsten target: a) without gold foil; b) with gold foil on ceramic ring; c) with gold foil on brass ring. The incident current for all set-ups was 50 mA. The response threshold of the oscilloscope is 13.54 V.

The absorption coefficient of 0.54 is in very good agreement with the simulated and literature value of 0.55 and confirms the assumption that secondary electrons do not contribute to the current through the sample. They are collected by the gold foil and dissipated through the brass ring and the sample. An unexpected result is the high current through the foil on the ceramic ring. It was meant to determine absorption by the gold foil itself and the absorption coefficient was expected to be smaller than without foil, because ceramic is an electric insulator and therefore the collected electrons are trapped. There are two possible explanations for this high value. First: During all experiments the gold foil was partly detached from the brass ring as well as from the ceramic ring. Due to that the foil could touch the tungsten target and therefore negate the insulation effect of the ceramic ring. Second: The insulation worked and was not abolished by the detached gold foil. That resulted in a negatively charged foil and ring. Due to this space charge secondary and thermionic electrons were pushed back to the sample because of the coulomb repulsion. Nevertheless, this experiment showed that the electron absorption coefficient for electrons of tungsten ϵ might be closer to the simulated value of 0.55.

2.3.2 Pilot-PSI

The exposure of tungsten to high flux hydrogen plasma was done with the linear plasma device Pilot-PSI (plasma surface interaction) at DIFFER. It produces plasma parameters such as electron densities $n_e \approx 10^{19} - 10^{21}$ m^{-3} and temperatures $T_e \approx 1$ eV – 5 eV

($T_e = T_i$ in Pilot-PSI for floating targets), which are ITER divertor relevant steady state conditions [70].

A schematic overview of the facility is given in figure 2.12. The vacuum vessel with a length of 1 m and a diameter of 0.4 m is pumped down to a pressure of ~10^{-6} mbar which increases during exposure to ~1 to $2{\cdot}10^{-2}$ mbar. It is placed inside of five coils, which generate an axial magnetic field of up to 1.6 T. The plasma source consists of 3 tungsten cathodes, a stack of five copper plates with 4 mm diameter holes form a 30 mm discharge channel and a tungsten copper nozzle, which acts as an anode. The plasma is formed by cascaded arc exhaust along the magnetic field lines. It is confined to a column of ~15 mm diameter, which has the highest density and temperature in the centre. Pilot-PSI is a pulsed device due to limited magnetic cooling. Each plasma pulse can have a duration between 4 s and 160 s depending on the magnetic field. After that time the coils need a certain time to cool down. The plasma can be composed of various gases such as hydrogen, helium, argon or nitrogen and mixtures of them [51,71].

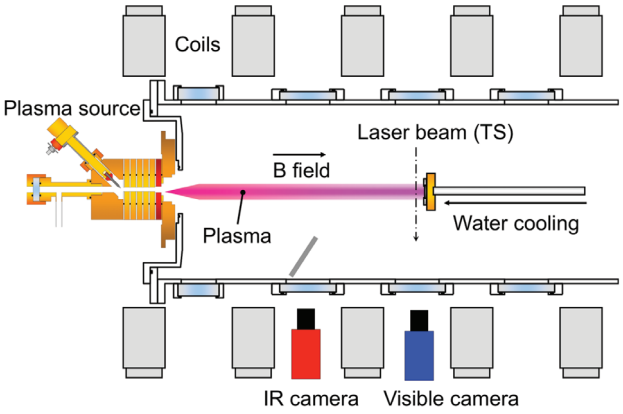

Figure 2.12: Schematic view of the linear plasma device Pilot-PSI at DIFFER [72].

For the exposure in Pilot-PSI all targets have to be clamped to an actively cooled copper heat sink. The flow rate of the cooling water and distance of the targets can be varied. This influences the maximum temperature of the targets during the experiment. The targets are monitored by infrared and visual cameras, multi-wavelength pyrometers and calorimetry. Plasma parameters are measured by Thomson scattering at ~21 mm in front of the targets [73].

2.3.3 MARION

The ion beam test facility MARION (Material Research Ion Beam Test Stand) is a device to expose PFMs to high energetic particle beams. It was developed and used

to study ion source conditions and for material testing [74]. A schematic view of the device is shown in figure 2.13.

The ion or particle beam is generated by an arc discharge source. It consists of 24 tungsten filaments and three grids with 774 extraction holes. The acceleration voltage can be varied between 15 kV and 60 kV with a beam current of $\leq$ 100 A. This leads to a total beam power of 70 kW up to 6 MW and power densities $\leq$ 120 MWm^{-2}. The pulse time depends on the acceleration voltage. Below 30 kV the source can run between 10 ms and 30 s, above 30 kV it can only run up to 10 s. After a pulse the source needs a cool down time between 1 and 5 minutes. A neutral or ion beam can be created using either H_2 or He gas, but mixtures are also possible [74, 75].

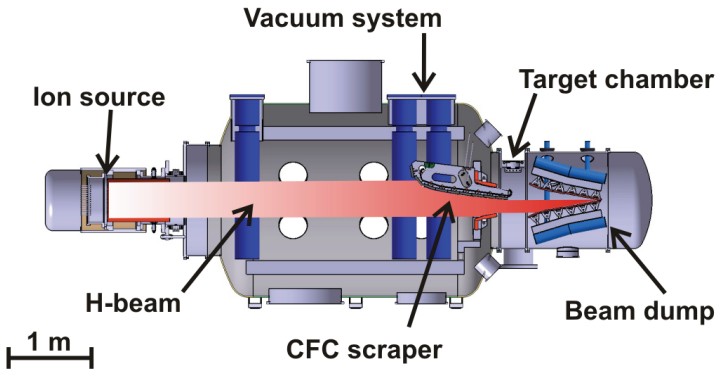

Figure 2.13: Schematic view of the material ion beam test facility MARION according to [74].

Before the source can work properly the whole device has to be evacuated. The vacuum system consists of rotary vane pumps, roots pumps, turbo molecular pumps and cryo pumps with a total pumping capacity of 1.2×10^6 l/s and reaches a base pressure of 10^{-6} mbar. Targets can be assembled via a flange with a diameter of 150 mm in the target chamber (cf. appendix A). A carbon fibre composite (CFC) scraper protects the supporting structures such as cooling tubes and thermocouples. It can withstand power densities up to 80 MWm^{-2} for 10 s. Copper beam dumps protect the back side of the target chamber from the particle beam and are used as vertical and horizontal calorimeter. Other diagnostics are CCD (Charge-Coupled Device), NIR (Near Infrared) and FIR (Far Infrared) cameras as well as one and two colour pyrometers and thermocouples [74, 75].

2.3.4 Nd:YAG laser

The experimental set-up of a thermal shock experiment with a laser beam is shown in figure 2.14 and normally used for laser induced desorption measurements. An in-

dustrially available Nd:YAG laser provided by LASAG Industrial-Laser (Typ: FLS N 352N-306, cavity 306) was modified for the desorption/thermal shock experiments. It has a wavelength of 1064 nm, a beam diameter of 6 mm and is commonly used for welding applications. The beam is coupled into a fibre-optics with a 400 μm core diameter and guided 35 m to the experiment [52].

The beam profile of the laser is not constant, neither in spatial nor in time dependent course. However, because of the total reflection in the fibre-optics and for a pulse duration of more than 0.7 ms the beam profile can be considered as a box profile with constant intensity. This is very important for the determination of the correct beam intensity. Pulse duration and frequency can be varied between 0.1 ms – 20 ms and 0.1 Hz – 1000 Hz, respectively. The combination of these parameters is limited by the threshold values of the laser: the maximum beam power is 20 kW, the maximum energy is 60 J and the maximum average power is 300 W [76].

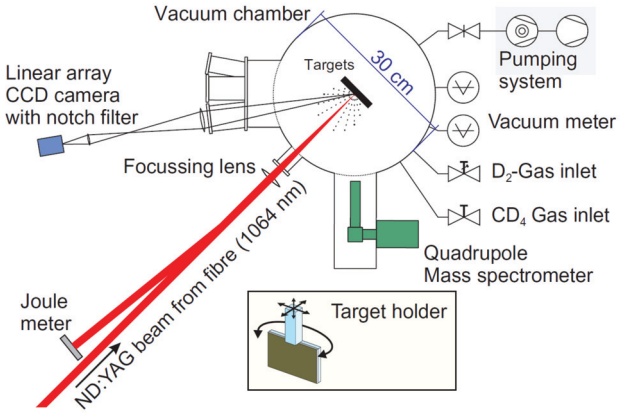

Figure 2.14: Experimental set-up of the pulsed Nd:YAG laser beam [52].

The light of the Nd:YAG laser is in the infrared range and therefore not visible for the human eye. To adjust the laser beam on the sample a He-Ne-laser has to be used. Its red light is in the range between 630 to 640 nm with a power of several milliwatt. Both laser beams follow the same path and therefore allow to position the beam with an accuracy below 0.5 mm (half beam diameter) [76].

The samples are located in a cylindric vacuum chamber with a height of 1 m and a diameter of 30 cm where the decoupled laser beam is imaged onto the targets by a lens with a focal length of 30 cm. The target holder can be rotated and moved in xyz-direction. All tests are performed under vacuum with an initial pressure between 10^{-7} and 10^{-8} mbar [52, 76].

Before thermal shock experiments on tungsten are performed it is absolutely essential to know how much energy is absorbed by the target material and how much is reflected. Therefore the reflectance of a tungsten surface, polished to a mirror finish, was determined by a reflectometer. The results are plotted in figure 2.15 and show that about 60 % of the incident laser light (wavelenght: 1064 nm) is reflected and only 40 % of the laser beam energy is absorbed by the tungsten target. These values have to be taken into account for the planning and execution of thermal shock tests with this laser beam facility.

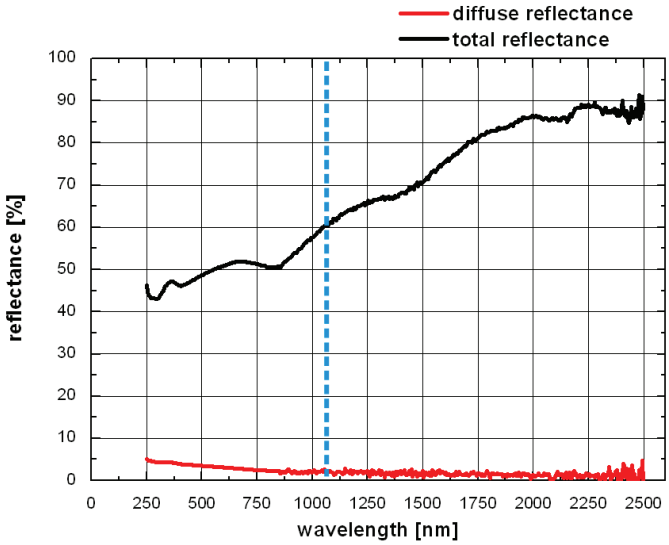

Figure 2.15: Reflectance of a polished tungsten surface in dependence on the wavelength. The dashed blue line represents the wavelength of the Nd:YAG laser.

2.4 Post mortem analysis methods

A lot of different diagnostic and examination techniques had to be used to characterise the material structure before and after testing. These comprises profilometry, scanning electron microscopy (SEM), light microscopy (LM) and metallography.

For the characterisation of the surface morphology a laser profilometer (wavelength: 670 nm) by the UBM GmbH was used. The reflection of the laser light is used to provide information about the morphology of the scanned surface with a lateral resolution of up to 2000 points/mm. The maximum measurable height difference is $\pm$ 500 μm with an accuracy of 10 nm within an area of up to 50 $\times$ 50 mm^2.

Especially for cracked surfaces SEM images were made and used to determine crack parameters such as distance and width. For most of the samples both, backscattered electron (BSE) images, which provide more information about the chemical composition, and secondary electron (SE) images, which give a very good impression of the topography, were used to get a comprehensive impression of the loaded sample surface.

LM images were used to get a good overview of large damaged sample areas, to characterise the materials microstructure and to measure crack depth as well as crack propagation into the sample material. The samples have to be prepared by metallographic means before the microstructure and the crack propagation into a material can be analysed. First, the samples were cut with a diamond wire near the region of the desired cross section. The remaining material was carefully ground with SiC paper (granulation 80 – 500) and polished with diamond paste (particle size 6 μm down to 0.25 μm). Afterwards the tungsten cross section was etched with a solution of NH_3, H_2O_2 and pure water (mixing ratio 1:2:7). LM images were taken before and after etching.

2.5 Finite element method (FEM)

The finite element method offers a wide spectrum of possible applications and solutions for complex problems. It is based on the solution of partial differential equations and/or integral equations which describe a given problem. The simulation requirements of such a model to solve a given problem are the idealisation of the system into calculable form, the definition of boundary conditions and their solvability and, most important, the correct interpretation of the obtained results [77].

During this work the FEM calculations were used to determine the maximum temperature distribution and development during the thermal shock tests presented in chapter 3. The selected software was ANSYS, which combines all necessary tools for a complete FEM simulation. It allows the simulation of thermal, mechanical, electromagnetic, fluid dynamic, transient and dynamic problems and their combinations. This can be preformed via so called input-files in “ANSYS parametric design language (APDL)” or a graphic interface called “the workbench”.

3 Thermal shock performance of different tungsten grades

As pointed out in chapter 1 the thermal shock resistance of a PFM is one of the most important selection criteria for an application in ITER and DEMO [40, 78]. This chapter will deal with the characterisation of the thermal shock response of five different tungsten grades. Additionally, the microstructure as well as the thermal and mechanical properties of all materials are determined. Afterwards all material properties and behaviours are compared to learn which material parameters have an influence on the thermal shock performance and to determine the load limits of tungsten for transient events.

3.1 Tungsten grades

Tungsten is one of the most promising materials for the application as PFM in the divertor region in ITER and is the only PFM which is foreseen for DEMO so far. Beside the many advantages of tungsten like the high melting temperature, high thermal conductivity, low sputter yield, low tritium inventory and low vapour pressure one of the most serious problems of tungsten is the poor workability due to the high ductile to brittle transition temperature (DBTT) which is characteristic for a body-centred cubic lattice structure. However, the DBTT is an ill-defined material parameter and depends strongly on the testing method, the purity of the material and the heat treatment. The DBTT of tungsten varies between 100 °C and 600 °C, which corresponds to approximately 5 % – 20 % of the melting temperature [79–81].

The material performance can be improved by alloying different elements and/or variations of the mechanical and thermal treatment during and after the manufacturing process.

3.1.1 Manufacturing and microstructure

The tungsten grades investigated in this work are industrially manufactured trial grades in terms of material composition and production process, provided by the Plansee AG, Austria. All grades were produced by a powder metallurgical production process,

which is schematically shown in figure 3.1. The raw material for all tungsten products is enriched tungsten oxide (30 % – 70 % WO_3), which is separated from ores (Fe/$MnWO_4$ and $CaWO_4$) by crushing, grinding, floating and roasting. Subsequently the oxide is hydrogen reduced at temperatures between 700 °C and 1100 °C to obtain tungsten powder. Alloying or doping elements can be added before or after the reduction process [79, 82].

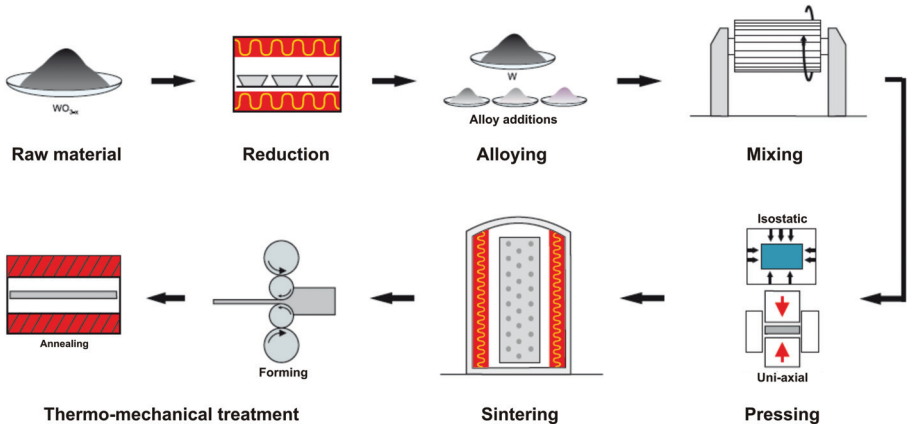

Figure 3.1: Schematic overview of the basic powder metallurgical production process of tungsten grades [82].

The sieved and homogenised metal powder is densified by cold isostatic pressing and sintered at temperatures between 2000 °C and 2500 °C. After sintering the pressed blanks have a rather low density of around 80 % and quite poor mechanical properties. In order to increase the density and to improve the material properties the blanks are mechanically deformed at temperatures up to 1600 °C. This treatment comprises rolling, hammering, forging or swaging. Intermediate and closing annealing of the blanks is necessary to reduce induced stresses and to maintain sufficient workability. The annealing temperature depends on the degree of deformation [79].

All investigated tungsten grades described below were deformed by forging. In contrast to conventional forging processes for tungsten blanks, the forging was not applied in radial but in axial direction as schematically shown in figure 3.2. The starting dimensions of the sintered blanks were approximately 80 mm in diameter and 116 mm in height which then were deformed into a disc shaped geometry with a diameter of 160 mm and a height of 29 mm. Finally, the material was stress relieved for 2 hours at 1000 °C.

The characterisation of the materials' microstructure (see section 2.4), essential for the qualification of the manufacturing process and the understanding of the thermal shock

response later investigated, was performed by cutting representative specimens from the edge and the centre of the received tungsten block (figure 3.2). Hereby, investigations in two orthogonal planes, i.e. the r/z (cross section: cs) and the r/φ (top view: tv) planes in cylinder coordinates, were performed to address the deformation induced anisotropy of the material. The minimum and maximum grain diameters were determined with the sliding caliper principle (feret min/max; cf. figure 3.8). Furthermore selected specimens from all materials were recrystallised at temperatures between 1600 °C and 1800 °C for 1 h in a vacuum furnace (pressure: 10^{-6} mbar). Those recrystallisation temperatures and durations were set according to the information given by the manufacturer. The resulting changes in microstructure were also investigated as described before.

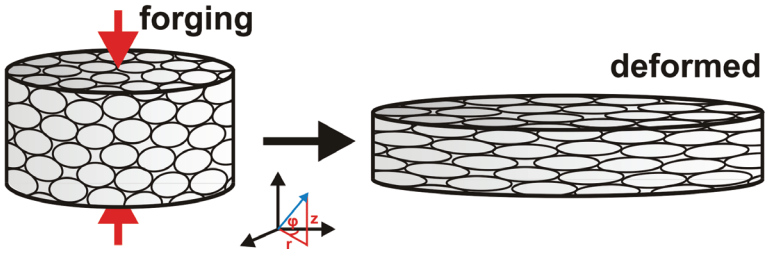

Figure 3.2: Sintered tungsten block forged axial into a flat disc geometry with a height of approx. 29 mm and a diameter of approx. 160 mm.

W-UHP (Ultra high purity tungsten) is manufactured from tungsten powder with a purity of 99.9999 wt% (metallic purity excluding molybdenum < 20 μg/g) to avoid the outgasing of impurities. It is used for the electrodes in HID (High Intensity Discharge) lamps because the high purity guarantees a consistent lamp quality and increased life time. Parts of the material was recrystallised at 1600 °C for 1 h [82]. Figure 3.3 shows LM images of the as-received and recrystallised grain structure. It is easy to see that the as-received grains resemble the shape of the deformed tungsten block shown in figure 3.2. The average grain dimensions are given in the table on the right side as well as their ratio to quantify the degree of deformation.

Pure W has only a few applications as coating material, for the construction of heating elements or heat shields. In general tungsten is used as doped or alloyed material to improve its properties for industrial applications. Pure tungsten is manufactured by Plansee with a purity of 99.97 wt% (metallic purity excluding molybdenum < 100 μg/g) [41, 82]. LM images of the grain structure in the as-received and recrystallised state as well as average grain dimensions are shown in figure 3.4. In comparison to the as received W-UHP the grains of pure W are deformed stronger. However, after the recrystallisation at the same conditions as W-UHP the grains show a similar homogenised structure as for W-UHP.

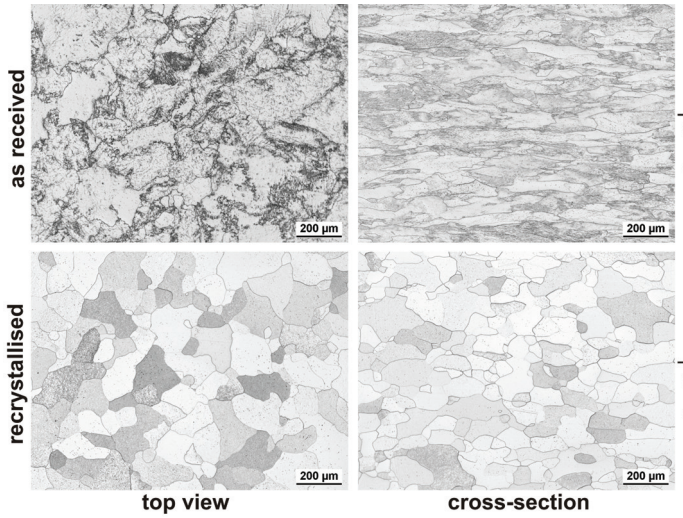

	feret min [µm]	feret max [µm]	ratio
tv	53.2	66.7	0.80
cs	48.3	169.5	0.29

	feret min [µm]	feret max [µm]	ratio
tv	76.0	125.9	0.60
cs	74.2	146.9	0.51

Figure 3.3: LM images of the as received and recrystallised W-UHP microstructure. The average grain dimensions are given in the table on the right side.

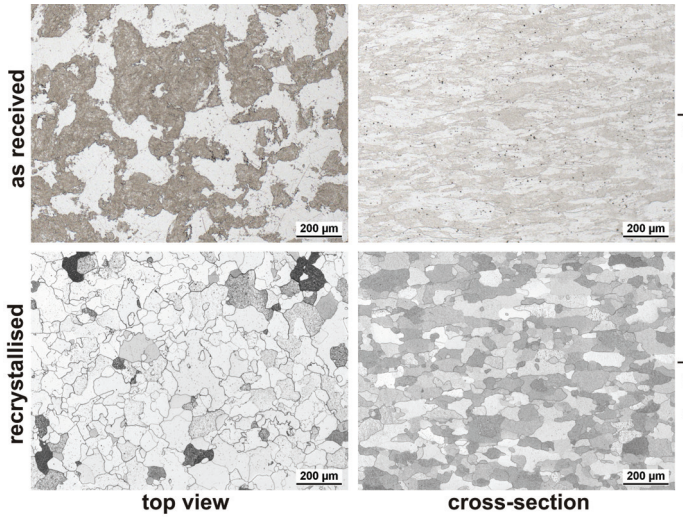

	feret min [µm]	feret max [µm]	ratio
tv	40.0	121.0	0.33
cs	42.3	264.0	0.16

	feret min [µm]	feret max [µm]	ratio
tv	50.6	78.7	0.64
cs	37.7	68.1	0.55

Figure 3.4: LM images of the as received and recrystallised pure W microstructure. The average grain dimensions are given in the table on the right side.

WVMW (Tungsten-Vacuum-Metallising-Tungsten) is pure tungsten doped with ppm levels of potassium (K). This special grade comprises 15 – 40 ppm potassium. During the sintering and deforming process small potassium filled voids are formed and break up into nanometre sized bubbles. Due to these very small bubbles, which are located inside the grains as well as at the grain boundaries, the movement of dislocations and grain boundaries is impeded. This results in grain refinement, improved ductility, improved stability of grain boundaries and therefore in an increase of the recrystallisation temperature in comparison to W-UHP and pure W. As consequence WVMW has to be recrystallised at 1800 °C for 1 h. It is mainly used for anodes in short arc lamp manufacturing, because of its high arcing resistance [82–84].

An overview of the grain structure before and after recrystallisation is given in figure 3.5. The effect of a more homogeneous grain structure after the recrystallisation is the same as for W-UHP and pure W, but the grains themselves are much smaller.

WTa1 and WTa5 tungsten consist of pure tungsten alloyed with 1 and 5 wt% tantalum, respectively. These are experimental tungsten grades which are not commercially available. Today, only tantalum rich alloys are of technical importance, because of the combination of the good corrosion resistance of tungsten and the high elasticity of tantalum. The system tungsten and tantalum is characterised by a complete miscibility over the complete composition range. Tantalum itself is a refractory metal like tungsten but with a lower melting point of 3020 °C. Its main advantage is that it is still ductile at low temperatures (DBTT = -269 °C). The main application of tantalum are capacitors with a high capacity [79, 85, 86]. Both materials were recrystallised for 1 h, but WTa1 at 1600 °C and WTa5 at 1800 °C, because the high amount of tantalum increases the recrystallisation temperature [79].

Figure 3.6 shows LM pictures of WTa1 before and after recrystallisation. The general anisotropic grain structure and the homogenisation after recrystallisation is very similar for WTa5. Even concerning grain dimension both materials show no significant differences. They vary within ± 2 μm, except for the maximum value of the as received cross section, which is 25.3 μm and results in a ratio of 0.19. The grains of WTa1 and WTa5 are the smallest of all investigated tungsten grades. Grain dimensions of WTa5 are given in appendix C.1.

Beside the differences in composition and grain size, the general grain structure in the as received state and after the recrystallisation is the same for all investigated materials. The as received grain structure assimilates the shape of the original tungsten block (see figure 3.2), while the recrystallised microstructure shows a more homogeneous pattern. Additionally the grain structure and size for each tungsten grade showed no variation in dependence on the position within the block. Furthermore no porosities were observed. To approve that, the density of each tungsten grade was measured. All obtained re-

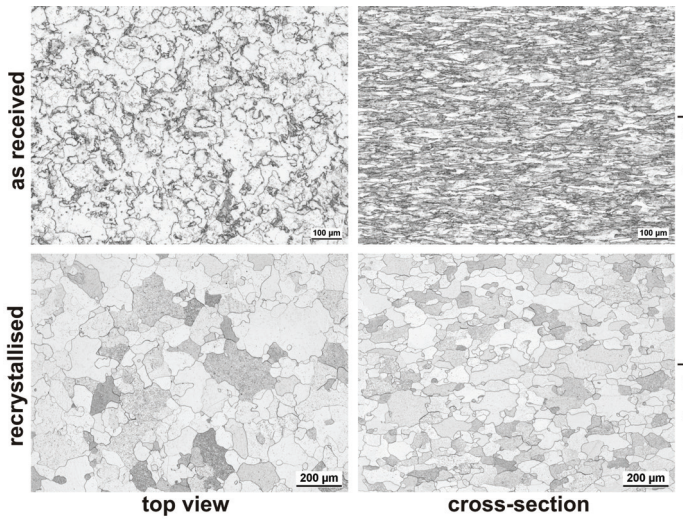

	feret min [µm]	feret max [µm]	ratio
tv	17.4	34.9	0.50
cs	10.2	45.8	0.22

	feret min [µm]	feret max [µm]	ratio
tv	40.9	68.0	0.60
cs	38.8	75.0	0.52

Figure 3.5: LM images of the as received and recrystallised WVMW microstructure. The average grain dimensions are given in the table on the right side.

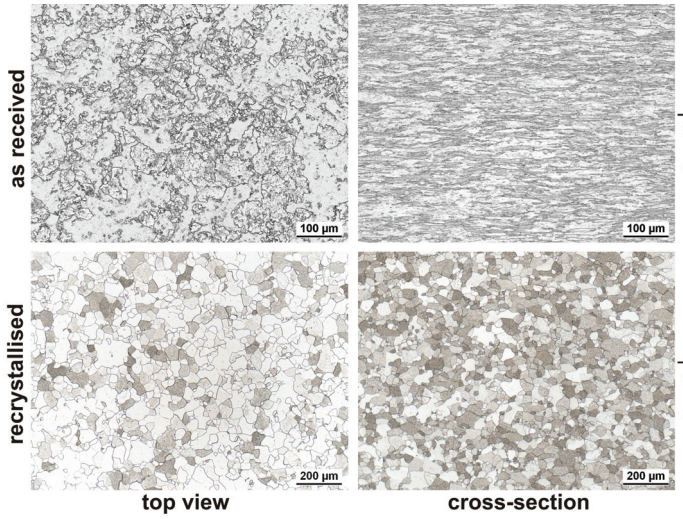

	feret min [µm]	feret max [µm]	ratio
tv	9.5	17.7	0.54
cs	5.6	16.4	0.34

	feret min [µm]	feret max [µm]	ratio
tv	18.0	27.2	0.66
cs	14.5	23.9	0.61

Figure 3.6: LM images of the as received and recrystallised WTa1 microstructure. The average grain dimensions are given in the table on the right side.

sults are very similar and at most 2 % smaller than the literature value of 19.25 gcm^{-3} [79]. The measured values are listed in appendix C.1.

Furthermore the grain areas for the cross section and the top view of the investigated tungsten grades were measured and the results are shown in figure 3.7. For each material the grain areas for cross section and top view are very similar. Both pure materials W-UHP and pure W without any doping or alloying elements have very similar grain areas and the largest grains in comparison to the other three materials. The grains of WVMW are more than five times smaller, because of the potassium doping and the impeding function of nano- and microbubbles on dislocation and grain boundary movement. The grains of WTa1 and WTa5 are even smaller. Possible reasons for that could be a slower grain growth because of the high amount of foreign atoms, which have a similar effect as the bubbles in WVMW or the use of finer powder during the manufacturing process to achieve a more homogeneous distribution of tantalum. There is no satisfying answer to this question, because the details of the manufacturing process are confidential.

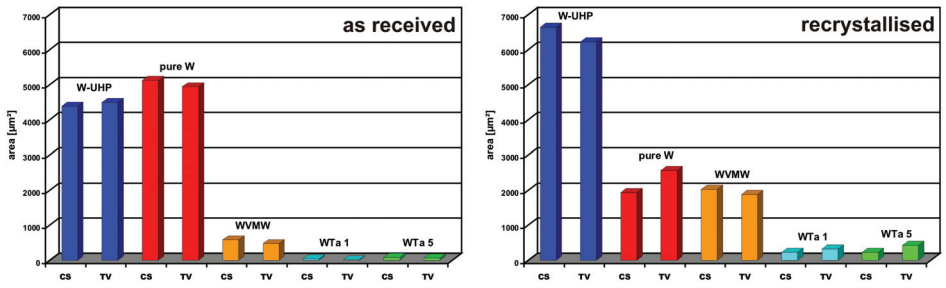

Figure 3.7: Overview of the average grain areas for all investigated tungsten grades in cross section and top view. Left: as received; Right: after recrystallisation at different temperatures for 1 h. All grains grow during recrystallisation except for pure W where the grains shrink.

For the recrystallised materials the grain sizes increased during the heating process by 50 % and for some materials even by more than 1200 % (e.g. WTa1). The only exception is pure W. Its grains did not grow, they even decreased in size by more than a factor of two. An explanation for this behaviour can be found in the mechanisms that take place during the recrystallisation process. Recrystallisation of a cold worked or heavily deformed metal means the nucleation and growth of new strain free grains and the movement of grain boundaries. Both mechanisms are driven by the stored deformation energies in the lattice and continue until the deformed lattice is completely replaced by the new grains or when the heat treatment stops. The recrystallisation speed depends on the amount of deformation energy in the lattice, the maximum temperature, the initial grain size as well as the amount and kind of foreign atoms in the

lattice. Pure W shows no significant differences in the first two parameters compared to the other materials, but the foreign atoms in combination with large grains provide an explanation for the smaller grain size. Foreign atoms accumulate predominantly at grain boundaries, especially if they are not of the same size as the matrix atoms. They impede the grain boundary movement and slow the recyristallisation process down. Additionally large grains provide less nucleation sites for new grains. For the other materials these effects are negligible. W-UHP has only a very small amount of foreign atoms, WVMW has the same amount of foreign atoms as pure W but a much smaller grain size and tantalum atoms do not accumulate at grain boundaries and have nearly the same size as tungsten atoms (W: 135 pm; Ta: 145 pm) [87, 88].

The angle distribution of minimum and maximum grain diameters was measured to quantify the elongated grain structure in the as received state and the homogenisation after the recrystallisation. Therefore the angle of feret min and max according to the same horizontal side was measured (cf. figure 3.8). A value of around 0° or 180° means that the diameter is parallel to the horizontal axis and 90° that it is vertical. The results are plotted in figure 3.9. The first and second column show the results for the as received state in top view and cross section, respectively. The grains have a homogeneous distribution in top view and are strongly elongated in cross section, i.e. there is a very discrete angle distribution, as a result of the forging in axial direction. For the recrystallised state (third column) only the cross section results are shown, because the top view shows an angle distribution very similar to the as received state. There is still a slight accumulation of feret min at 90° and feret max at 0° and 180°, but after the recrystallisation the grain anisotropy is much less pronounced as for the as received state.

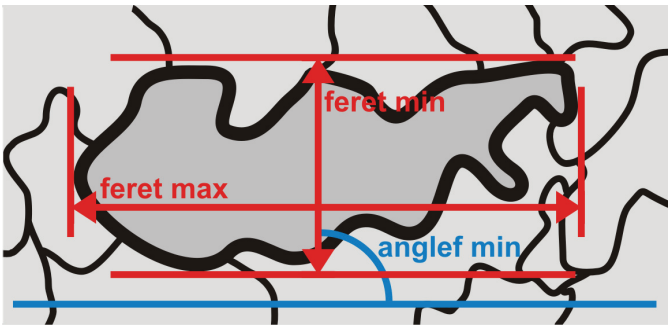

Figure 3.8: Schematic view of a typicall grain structure. Maximum and minimum grain diameters are measured with the sliding caliper principle feret min/max (red). The corresponding angles anglef min/max (blue) are determined according to the same horizontal side. The figure shows only anglef min, because for the depicted case anglef max is 0°/180°.

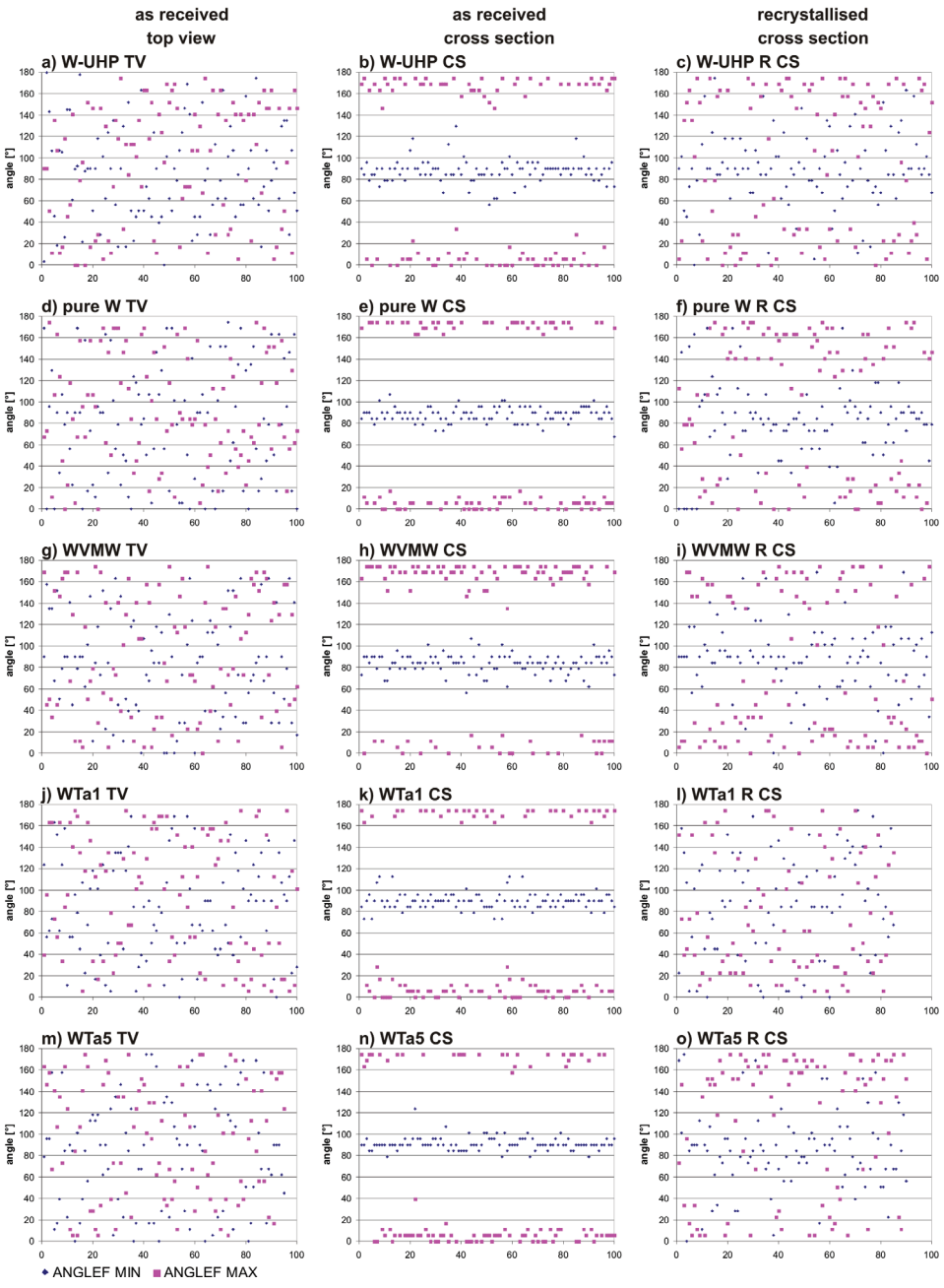

Figure 3.9: Angular distribution of the minimum (blue) and maximum (pink) grain diameter for all materials before (first and second column) and after the recrystallisation (third column). For the recrystallised state only the cross sections are shown, because both states show no significant differences in top view.

3.1.2 Mechanical properties

The tensile properties of the tungsten grades at elevated temperatures were investigated by using the high temperature vacuum furnace set-up at SCK•CEN, as described in subsection 2.1.1 [56]. The same test parameters were used for all materials. The deformation speed was 0.2 mm/min which results in a deformation rate of around 10^{-4} s^{-1}. The tests were performed at temperatures of 300 °C, 500 °C and 1000 °C. Tests at RT were not performed, because it is well known that tungsten is brittle at RT and the expected premature fracture provide no additional information. Furthermore the inhomogeneous grain structure had to be taken into account and therefore two different types of specimens were manufactured for each tungsten grade as shown in figure 3.10. Longitudinal specimens were manufactured with grains oriented parallel and transversal specimens with grains oriented perpendicular to the loading direction.

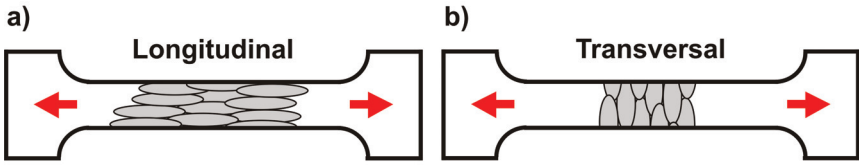

Figure 3.10: Grain orientation of the tensile test specimens. a) Grains orientated parallel to the loading direction (longitudinal); b) Grains orientated perpendicular to the loading direction (transversal). The loading direction is indicated by the red arrows.

The deformation of the specimens during the tests could not be measured with an extensometer, because of the high temperatures and lack of equipment. Instead, it was determined by the distance of the clamping jaws measured before and after the test. Additionally, the beginning of each curve does not show the expected linear stress strain dependency, because of the backlash of the tensile test device. Due to that the first data points are not shown. The results of all tests are plotted as engineering stress-strain curves in figure 3.11 for the longitudinal and 3.12 for the transversal specimens. The exact values of parameters like the ultimate tensile strength (UTS) σ_{UTS} or the fracture strain ϵ_U are not important for this work but the qualitative analysis of the curves allows a comparison of all tungsten grades.

One of the most obvious results is that all longitudinal samples (fugure 3.11) are plastically deformed before they fail, even at 300 °C. As a consequence, it can be assumed that for this test set-up all materials are above or at least in a temperature range around their DBTT. The general behaviour of a decrease in tensile strength with an increase in temperature is valid for all grades. However, most of the tungsten grades differ from each other in their tensile test behaviour. Pure W and WVMW have a very similar tensile strength and elongation for all temperatures. Both materials have nearly the

same composition, except for the higher potassium concentration of WVMW. The major difference is the grain size, which does not seem to have an influence on the tensile properties. In comparison to that, W-UHP exhibits a slightly lower tensile strength, but only one fifth of the fracture strain. Both can be explained by the much higher purity and the resulting lack of foreign atoms, which do not only improve the tensile strength but also have an influence on the DBTT regarding literature [79, 89]. This results in a higher DBTT of W-UHP and therefore in a reduced ductility at 300 °C. The difference in fracture strain nearly disappears for higher temperatures, while the difference in strength stays constant. This is a hint, that a small difference in DBTT is responsible for the varying elongation. The increase of tensile strength and the decrease of the total elongation of WTa1 and WTa5 can be explained by the amount of tantalum in the tungsten matrix, which causes solid solution hardening of these tungsten grades. While for WTa1 the effect is visible but less pronounced in comparison to e.g. pure W, the higher content of tantalum of 5 wt% improves the tensile strength by almost a factor of two compared to pure W. The total elongation is reduced for all test temperatures, but becomes less pronounced for increasing temperatures [79,90,91].

The results of the transversal tensile test specimens are shown in figure 3.12. In contrast to the longitudinal grain orientation the specimens with transversal grain orientation show no plastic deformation. Only at 1000 °C some materials show some strain in combination with a reduction of the cross section due to slow crack propagation through the specimen. Furthermore the tensile strength compared to the as-received state is reduced significantly for all materials. In general, grain boundaries are very susceptible areas for failure/crack formation in polycrystalline metallic materials. It can be resumed that due to the grain orientation perpendicular to the loading direction there is hardly any obstacle for the formation of cracks along grain boundaries and therefore the failure of the transversal specimen is more likely. This pronounced anisotropy of the mechanical properties due to the deformation during the production process is known as “texture strengthening” [79, 90, 92].

Tensile tests of the recrystallised tungsten grades were not performed, but the effect of recrystallisation on the mechanical properties can be predicted quite well referring to literature and other recrystallised reference tungsten grades tested at SCK•CEN. As described above recrystallisation means the nucleation and growth of deformation free grains within the deformed crystal lattice. The dislocation density which is amongst other parameters responsible for the increase in tensile strength, is reduced. Due to that the tensile strength of a recrystallised material will be reduced while the total elongation is increased. In case of tungsten it is also important to mention that the DBTT increases and the higher total elongation is only noticeable for elevated temperatures [79, 90].

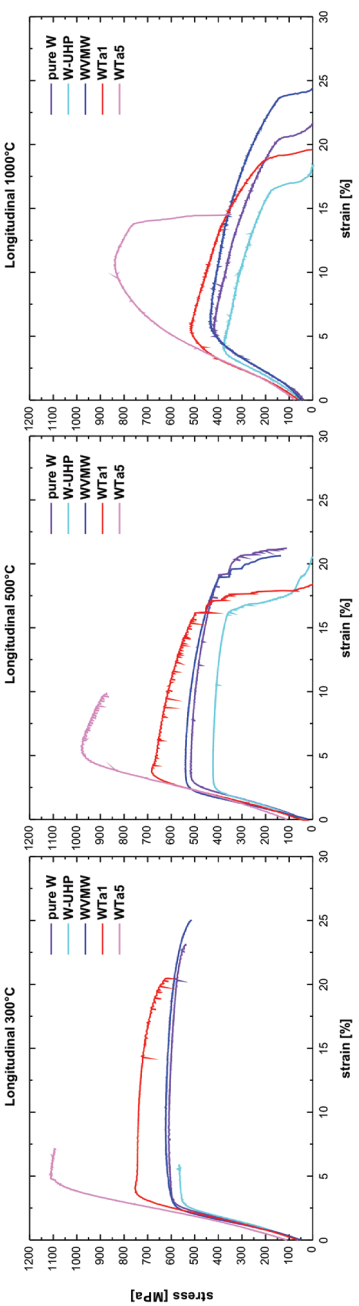

Figure 3.11: Stress-stain diagrams for the longitudinal grain orientation at 300 °C (left), 500 °C (middle) and 1000 °C (right) [56].

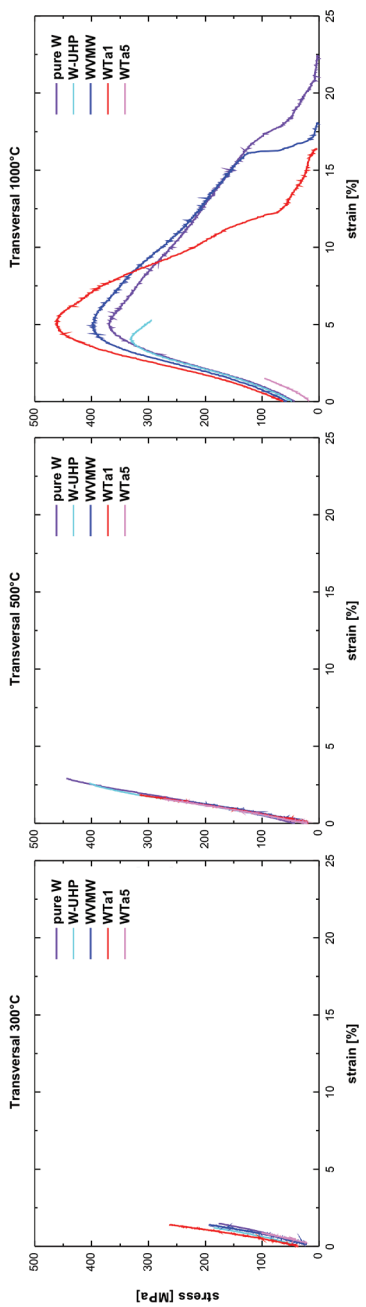

Figure 3.12: Stress-stain diagrams for the transversal grain orientation at 300 °C (left), 500 °C (middle) and 1000 °C (right) [56].

It is not possible to determine the Young's modulus from the stress-strain diagrams presented in figures 3.11 and 3.12 because the deformation of the samples could not be measured with an extensometer. Therefore the Young's modulus for all tungsten grades was determined by the impulse excitation method explained in subsection 2.1.2. For the calculation of the Young's modulus (formula 2.1) a Poisson's ratio of 0.3 according to [93] was used. The specimen dimensions were measured with an accuracy of 0.05 mm which corresponds to a systematic error of ±20 GPa or ±5 %. A crucial point is the aspect ratio of the sample to obtain correct results. Therefore is was not possible to measure the Young's modulus for the transversal grain orientation because the manufactured tungsten blocks were too small in height to cut samples with the necessary dimensions. All tests could only be performed at atmospheric pressure and atmosphere. Therefore the temperature range was limited from RT up to 400 °C because oxidation of tungsten starts at temperatures above 400 °C [79].

The results of the impulse excitation measurements are shown in figure 3.13. Each curve combines values that were measured during the heating and the cool down phase of the experiments (two lines for each material and grain structure). For the as received (figure 3.13a) and the recrystallised (figure 3.13b) materials it can be stated that the Young's modulus is very similar for all five materials if the error range of ±20 GPa and the broad range of literature values (390 GPa – 410 GPa [93]) are taken into account. However, the nearly identical behaviour of similar materials with respect to foreign atom concentration and grain size is significant. The reason for this is the improvement of the materials strength to withstand deformation due to the solid solution hardening (WTa1, WTa5) and the stabilisation of the grain boundaries (WVMW). Only W-UHP and pure W show a slight increase of the Young's modulus in the range of 10 GPa after the recrystallisation. This increase is still within the error margin of ±20 GPa and could originate from irregularities of the specimen dimensions such as insufficient plane parallelism of the surfaces.

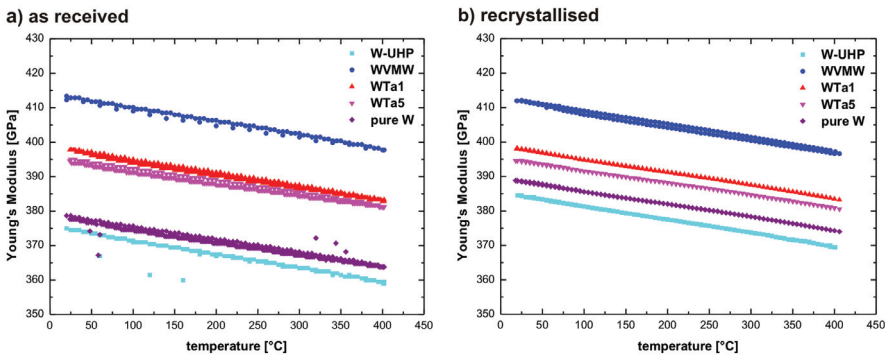

Figure 3.13: Temperature dependence of the Young's modulus for all five tungsten grades: a) for the as received state; b) for the recrystallised state.

3.1.3 Thermal properties

The temperature development of the specific heat capacity $c_p(T)$ and thermal diffusivity a(T) for all five tungsten grades was measured as explained in subsections 2.2.2 and 2.2.3. Based on these values it is possible to calculate the thermal conductivity for all tungsten grades by the formula $\lambda(T) = a(T) \cdot c_p(T) \cdot \rho(T)$ (cf. section 2.2). For the temperature dependence of the different material densities ρ literature values taken from [43] were used. This approximation is feasible because density measurements at RT of each tungsten grade (subsection 3.1.1) have shown that the deviation from the literature values is below 2 %. This error was considered for the calculation of the error margins of the calculated thermal conductivity values. The measured and literature values that were used for the calculations are given in appendix C.2.

Figure 3.14 shows the temperature profile of the calculated thermal conductivity values for all five tungsten grades. Especially the values at RT show a very large distribution which can be traced back to the scatter of the measured thermal diffusivities at low temperatures resulting from uncertainties of the laser-flash method (subsection 2.2.3). However, in combination with values at elevated temperatures it can be stated that the pure tungsten grades (W-UHP, pure W) and the potassium doped (WVMW) have very similar temperature profiles of the thermal conductivities. For WTa1 and WTa5 the thermal conductivity is smaller than for the other three tungsten grades. Especially for WTa5 and temperatures below 800 °C the thermal conductivity values are significantly smaller than for any other investigated tungsten grade. At higher temperatures this behaviour is less pronounced but WTa1 and WTa5 have still the smallest thermal conductivities of all investigated tungsten grades. The reason for this decrease of the thermal conductivity with increasing tantalum content is that the thermal conductivity/diffusivity depends on the level of impurities and the density of lattice defects in the material. With an increasing amount of foreign atoms in the crystal lattice the thermal conductivity decreases due to scattering of electrons by solute atoms (Wiedemann-Franz law) [94].

The CTE of all five tungsten grades was measured with the facility described in subsection 2.2.1 and the results are shown in figure 3.15. In contrast to the thermal conductivity values (figure 3.14), the materials show no technical relevant differences in their thermal expansion behaviour. The temperature range that could be covered during a measurement was limited from 300 °C up to 900 °C, because the thermocouple provides only reliable data for this temperature range and changes during the measurement are not possible. Furthermore the waviness of the measured data points has no physical reason. This is caused by the analysing software and do not appear in the raw data.

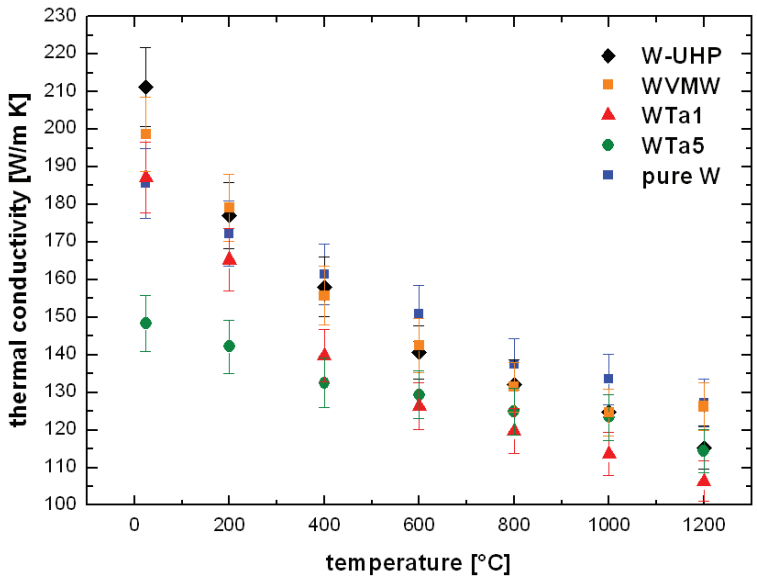

Figure 3.14: Calculated thermal conductivity values for all five tungsten grades. The tungsten grades show a very similar temperature dependence. Only WTa1 and WTa5 have a smaller thermal conductivities especially for low temperatures.

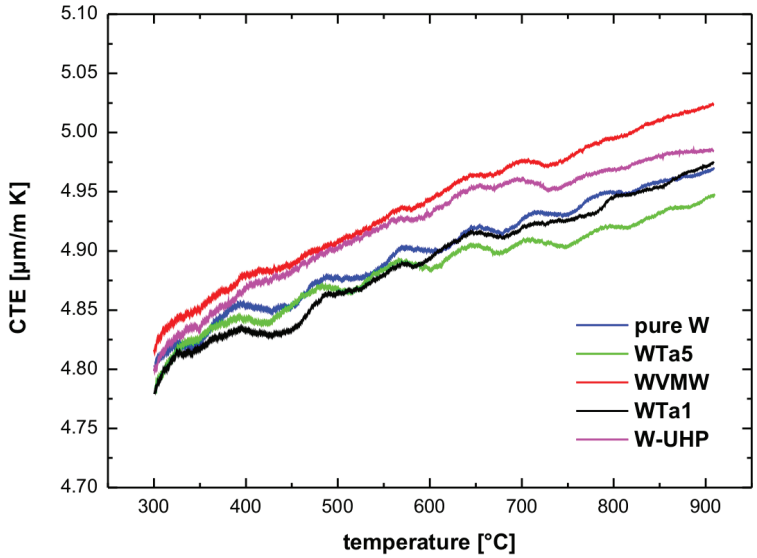

Figure 3.15: Results of the CTE measurements of the different tungsten grades. All materials show very similar thermal expansion behaviour.

3.2 Experimental conditions

All in section 3.1 characterised tungsten grades were exposed to ELM like thermal shock conditions in JUDITH 1 (see subsection 2.3.1). Samples were cut from the as received tungsten blocks with the dimensions 12 × 12 × 5 mm^3 by electric discharge machining (EDM). Due to the inhomogeneous grain structure (see subsection 3.1.1), two different sample types were cut from the block regarding to the grain orientation and one was recrystallised after cutting. An overview of the different sample types, their cutting scheme and the resulting grain orientation is given in figure 3.16. The loaded area is indicated by the red square in figures 3.16b, c and d. Longitudinal (L) samples (figure 3.16b) were cut in such a way, that the grain orientation is parallel to the e-beam exposed surface. Recrystallised (R) samples (figure 3.16c) had the same grain orientation as the longitudinal samples, but were subjected to a heat treatment (subsection 3.1.1) after cutting. For transversal (T) samples (figure 3.16d) the grains are oriented perpendicular to the loaded surface. After cutting or heat treatment all samples were polished to a mirror finish with diamond paste with a particle size down to 1 μm to remove surface damages and modifications as well as thermally induced defects by the EDM-cutting (electrical discharge machining) process. The obtained surfaces represent a defined undamaged reference state for all samples and materials and facilitate the comparison of the induced thermal shock damages and surface modifications.

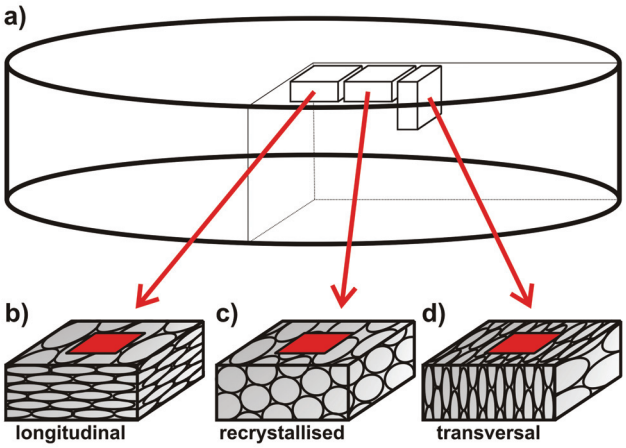

Figure 3.16: Cutting scheme and grain orientation relative to the loaded area (red square) for the thermal shock samples in JUDITH 1. a) Sample alignment during cutting from the as received block; b) Longitudinal samples (L) with grains oriented parallel to the loaded surface; c) Recrystallised samples (R) with grain structure after the heat treatment; c) Transversal samples (T) with grains oriented perpendicular to the loaded surfcae.

The experimental parameters for the cyclic thermal shock test in JUDITH 1 were set to values close to the expected ELM conditions in ITER (section 1.3.1). For that reason the samples were exposed to absorbed power densities between 0.16 GWm^{-2} and 1.27 GWm^{-2} using electrons with a kinetic energy of 120 keV. These values correspond to heat flux factor (F_{HF}) values between 5 $MWm^{-2}s^{1/2}$ and 40 $MWm^{-2}s^{1/2}$, which were calculated by the formula $F_{HF} = P_{abs} \cdot \sqrt{t}$ and is a common factor in the fusion community to quantify threshold values [95]. These values were calculated by formula 2.8 taking an electron absorption coefficient of 0.46 for W into account which corresponds to the value observed in in-situ absorbed current measurements during RT-tests. This conservative approximation was chosen to give a certain safety margin, since it neglects the influence of emitted thermal and secondary electrons which cannot be measured during the test. Their contribution to the calculation of the absorbed energy was determined by an experiment discussed in subsection 2.3.1 and Monte Carlo methods resulting in a combined absorption coefficient of 0.55.

A homogeneous loading of the samples was achieved by exposing a small area of 4×4 mm^2 with the focused electron beam at very high scanning frequencies of 47 kHz in the x-direction and 43 kHz in the y-direction. The pulse length was 1 ms, which is about double the length of an ELM in ITER, applying absorbed energy density between 0.16 MJm^{-2} and 1.27 MJm^{-2}. These lead to an estimated surface temperature increase ΔT for each individual pulse between approximately 300 K and 2400 K. In addition to the tests performed at RT, a graphite holder with a tubular heating cartridge and a new heating device (described in appendix B) were used to achieve base temperatures up to 600 °C. The total number of pulses was fixed to 100 except for 0.95 GWm^{-2} at RT at which additional tests were performed with pulse numbers between 1 and 1000. All tests were performed with an inter-pulse time of about 2 – 3 s to allow a complete cool down of the specimens to the respective base temperature.

Figure 3.17 gives an outline of all experimental conditions. The first tests were performed to get an overview of the damage behaviour for the longitudinal specimens (black diamonds). After that, additional power densities and base temperatures were chosen to localize the different damage and cracking thresholds (red squares). Based on these results transversal and recrystallised specimens were tested under selected conditions (blue frame) to quantify occurring differences of the thermal shock response. Longitudinal specimens were exposed to 1, 10, 100 and 1000 pulses (green dashed frame).

Furthermore longitudinal W-UHP samples were exposed to thermal shock events in a pulsed laser device (subsection 2.3.4) to investigate eventual differences to an electron beam exposure. It was not possible to heat the samples to different base temperatures (no heating device available for the laser) and for that reason the focus was to apply 100 pulses with comparable absorbed power densities, a pulse duration of 1 ms and an

inter-pulse time of 2 s. The major problem was to reach comparable power densities in combination with a similar geometry of the loaded area. Only 27 % of the incident laser energy are absorbed by the polished tungsten sample due to losses in the optical fibre and reflection losses at the lenses, mirrors and the sample itself. A circular loading area with a diameter of 2 mm was chosen. This results in absorbed power densities between 0.19 GWm^{-2} and 1.51 GWm^{-2} and corresponds to the absorbed power densities of the electron beam thermal shock events in JUDITH 1 with an absorption coefficient of 0.55.

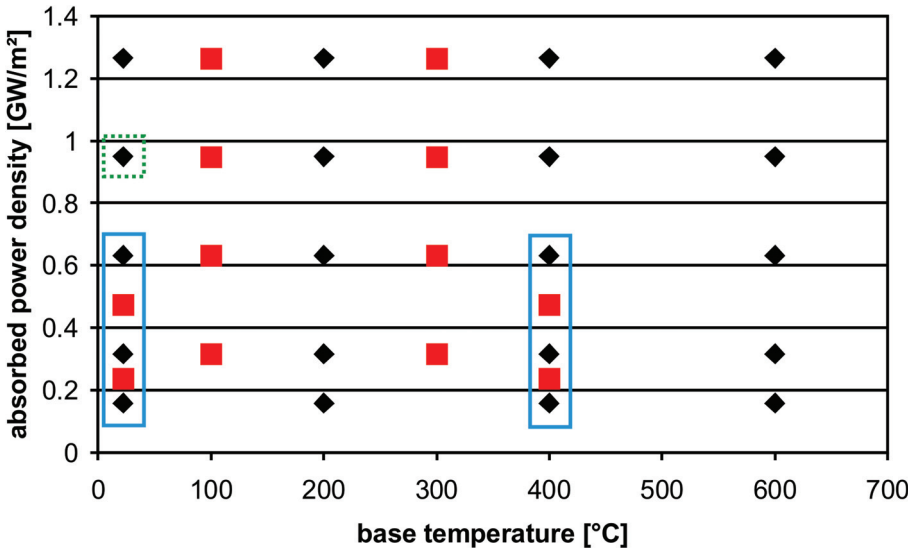

Figure 3.17: Schematic overview of all used experimental conditions. Tests of longitudinal specimens are indicated with black diamonds. Additional tests at intermediate power densities and base temperatures should localize the different thresholds (red squares). Transversal and recrystallised specimens' test conditions are framed in blue. Longitudinal specimens were exposed to varying pulse numbers (green dashed frame).

3.3 Simulation of temperature distributions

One of the major problems is the determination of the correct maximum temperature values during the simulation of transient thermal shock events in the electron beam device JUDITH 1. Reasons for that are the extremely short duration of such events in the ms range, the small exposed area (to achieve a homogeneous loading) and the change of the surface morphology during the experiment which has a strong influence on the emission coefficient of the sample's surface. To overcome these problems a pyrometer with a high time resolution, a small measuring spot and a two colour mode

would be necessary. However, even then it would be very difficult to adjust the pyrometer to the correct spot on the sample. Due to that the maximum temperatures for all loading conditions described in section 3.2 and the temperature developments during one pulse were simulated by finite element methods (FEM) (section 2.5). Both are very important for the interpretation of the experimental results. All simulations were done with material parameters for pure tungsten taken from [96]. Because of the symmetry of the sample and loaded area the simulation could be reduced to one eighth of the geometry and was used to simulate the temperature development during and after one pulse. An example of such a geometry and the temperature distribution for a heat load of 1.27 GWm^{-2} after 1 ms is shown in figure 3.18. These calculations were done for all applied power densities and base temperatures to determine maximum temperatures and the temperature evolution during the cooling period of 3 s between two thermal shocks. Losses due to radiation are not included in the simulation. They are negligible for temperatures below 2000 °C. Above this temperature they would not effect the maximum temperature and mainly contribute to the cooling down after the thermal shock event.

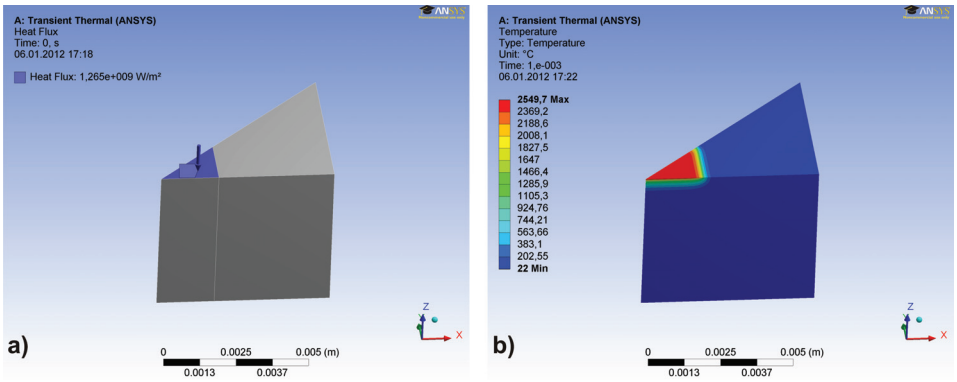

Figure 3.18: FEM simulation: a) One eighth of the sample geometry was used for the calculation. b) the maximum temperature and temperature distribution for 1.27 GWm^{-2} after 1 ms in °C.

A result of these simulations is that an inter-pulse time of 3 s is far enough time for a complete cool down of the sample even without radiation cooling. There is no risk of a significant increase of the base temperature as can be seen in figure 3.19a. The maximum temperatures for all experimental conditions after 1 ms are plotted in figure 3.19b. They comprise a temperature range from 300 °C at RT and 0.16 GWm^{-2} up to 3200 °C at 600 °C base temperature and 1.27 GWm^{-2}. It can be assumed that these loading conditions are not severe enough to melt the materials surface, but about half of the samples will reach surface temperatures close to their recrystallisation temperature or even above for < 1 ms.

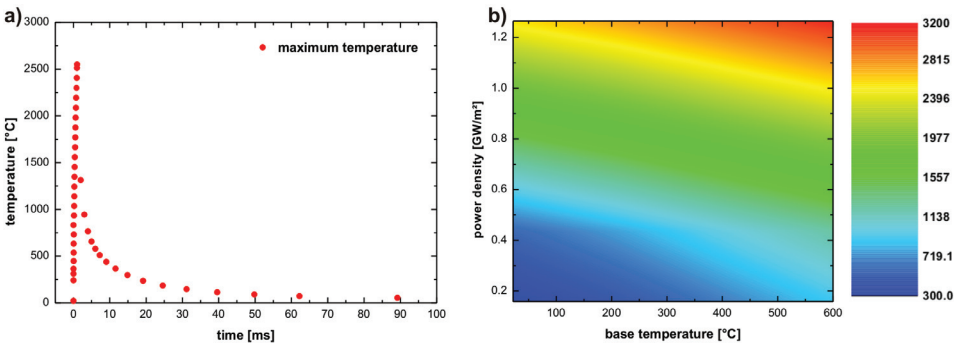

Figure 3.19: Results of the FEM simulations: a) Development of the maximum temperature during and after a thermal shock event at RT and 1.27 GWm^{-2}; b) Maximum temperatures for all loading conditions after 1 ms in °C.

Another issue is the volumetric heating within a thin layer instead of pure surface heating. The reason for this is the high energy of the electrons (120 keV) and the resulting penetration depth of about 7 μm mentioned in subsection 2.3.1. To estimate how severe the resulting temperature gradients are, a worst case scenario was simulated. Figure 3.20a shows the simulation geometry. The complete heat load of 0.63 GWm^{-2} was applied 7 μm below the top surface for 1 ms. An example for the temperature distribution after 1.2 μs is given in figure 3.20b. The temperature dependent material parameters of pure tungsten were used for these calculations.

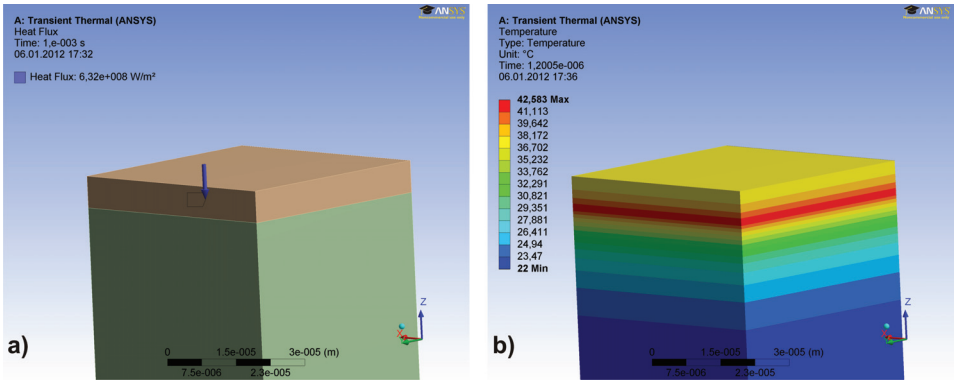

Figure 3.20: FEM simulation: a) Simulation geometry and loaded area 7 μm below the top surface; b) Temperature distribution after 1.2 μs at a heat load of 0.63 GWm^{-2} in °C.

The results of the simulation are shown in figure 3.21a and b. The difference between the maximum temperature (7 μm below top surface) and the top surface is at most

5.3 K or 12.4 % at the beginning of the pulse (1.2 μs) and rapidly decreases. After 0.033 ms the difference is below 1 %. Based on these results it can be assumed that the difference under real loading condition is even smaller and the thermal stresses induced by these temperature gradients in this small surface region can be neglected in comparison to the thermal stresses in the whole loaded area.

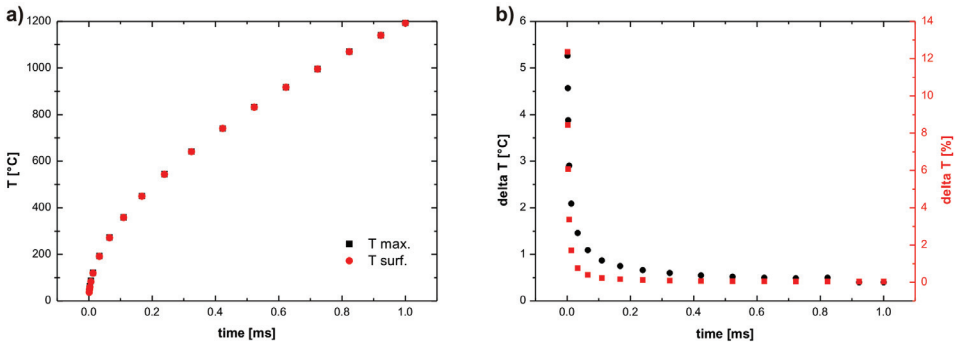

Figure 3.21: Results of the FEM simulations: a) Temperature values of the loaded surface (black square) and the top surface (red dots); b) Temperature difference between loaded and top surface in absolute number (black dots) and percentage (red squares).

3.4 Results and discussion

The thermal shock tests (section 3.2) were performed with five different tungsten grades (section 3.1) to investigate and compare their thermal shock response. Especially the comparison of the results should provide more information about the underlying mechanisms and material properties that influence the thermal shock behaviour of tungsten.

After the exposure to thermal shock events in JUDITH 1, the induced damages were investigated by SEM and laser profilometry. The observed damage types can be divided into four different groups which are represented by different symbols and colours as shown in figure 3.22. "No damage" (figure 3.22a) means that there are no observable changes in the surface morphology after the thermal shock loading. A sample is classified as surface modified (figure 3.22b), if the loaded surface shows significant changes of the surface morphology such as roughening and/or swelling after the exposure. Both groups were investigated by laser profilometry with an accuracy of 20 points/mm in order to examine to which group the sample belongs and to quantify the peculiarity of the surface modification. The difference between small cracks (figure 3.22c) and crack networks (figure 3.22d) is that small cracks are isolated and arbitrarily distributed in the loaded area. They are hardly visible to the naked eye and only observable by LMs

or SEMs, while crack networks consist of large cracks which form a continuous network over the whole loaded surface.

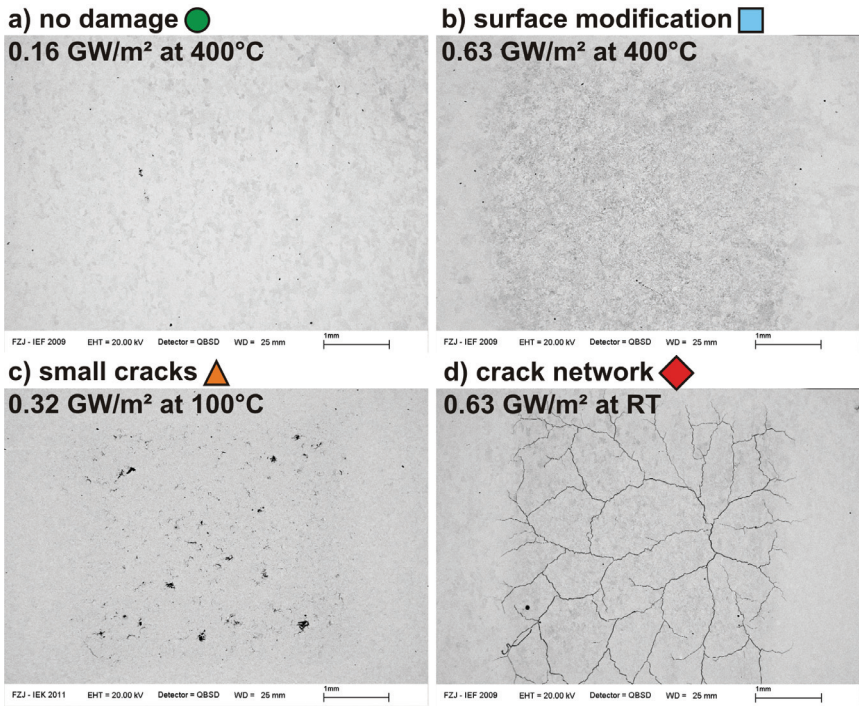

Figure 3.22: The four different damage types that can be observed after the exposure of tungsten to thermal shock events. a) No observable surface modifications or damages; b) Surface modifications like roughening; c) Small cracks that do not form a crack network; d) Thermal shock induced crack networks.

Beside the observation and classification of the induced damages, particular attention was paid to the thermal shock crack networks. SEM and LM images of the cracked surfaces and cross-sections were used to measure crack parameters such as median crack distance (figure 3.23a) of the whole cracked area, the crack width (figure 3.23b) and crack depth (figure 3.23c) as well as crack propagation into the bulk material after 100 thermal shock events. In figure 3.23 all crack parameters are indicated schematically for a cross section of a cracked sample. However, crack distance and width were determined on SEM and LM images of the cracked sample surfaces (top view).

It is very difficult to achieve statistically firm data for all of these crack parameters. It is nearly impossible to take a sufficient number of SEM images with a very high magnification and at different positions of the crack surface for a large number of samples. Especially for the crack width. Some of the later presented average crack

parameters have large error bars due a strong scatter of single values. This circumstance has to be taken into account for the interpretation of the obtained results.

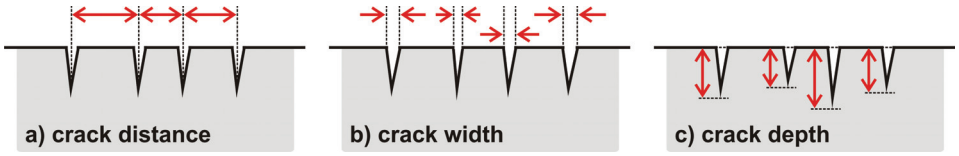

Figure 3.23: Different crack parameters: a) Crack distance: distance between adjacent cracks; b) Crack width: distance between the crack edges; c) Crack depth: distance between the surface and the crack tip.

3.4.1 Damage mapping

The damage mapping diagrams presented in this subsection follow the colour and shape coding introduced above. Every symbol represents one sample exposed to 100 thermal shock events at corresponding loading conditions. Based on these results, damage and cracking threshold values could be identified, valid for 100 pulses.

W-UHP

W-UHP has the highest purity of all investigated tungsten grades. Therefore it will be used as a reference material and all other tungsten grades will be compared with the thermal shock response of W-UHP. The different kinds of surface damages caused by thermally induced stresses in W-UHP with longitudinal grain structure (W-UHP L; figure 3.16b) are presented in figure 3.24 for 100 pulses and varying loading conditions. The induced damages strongly depend on the absorbed power density and the base temperature of the sample.

A main outcome of these investigations is that for W-UHP L two thresholds can be determined. The damage threshold is located between 0.16 GWm^{-2} and 0.24 GWm^{-2} and, in the investigated temperature region, independent of the base temperature. For loading conditions below this threshold the induced thermal stresses are not high enough to induce any visible damages such as surface modifications or cracks on the loaded surface. The region above this threshold is divided into two areas by the cracking threshold. This threshold depends on the base temperature and is located between 100 °C and 150 °C for W-UHP L. The material behaves brittle for base temperatures below this threshold. That means the material is not able to compensate thermal stresses by plastic deformation. Due to that brittleness thermal shock crack networks are formed to reduce these stresses. Above the cracking threshold the material provides sufficient ductility to deal with the occurring stresses by plastic deformation.

The tensile test results (subsection 3.1.2) and the large grain sizes of W-UHP (subsection 3.1.1) confirm that in this temperature region the material already shows ductile behaviour. Additionally, the large grain size reduces the grain boundary density at the loaded surface significantly and due to that the most susceptible points for crack initiation.

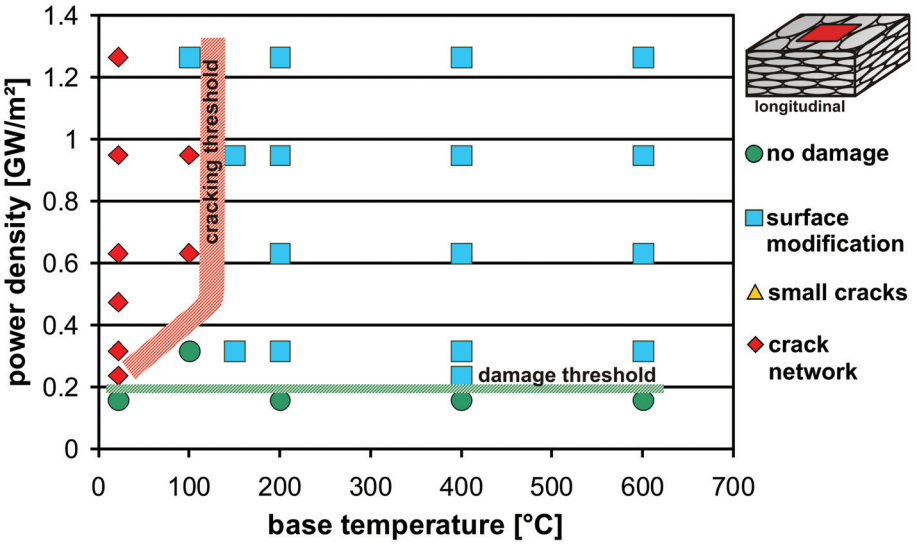

Figure 3.24: Thermal shock response of W-UHP L after 100 thermal shock events at different power densities and base temperatures. Below 0.16 GWm^{-2} no visible damage appears. Above a base temperature of 100 °C only surface modification occurs.

The results of the surface characterisation by laser profilometry are presented in figure 3.25. For every sample the arithmetic mean roughness R_a (DIN EN ISO 4287:1998) was determined and plotted in figure 3.25a with a reference value around R_a 0.1 μm (unloaded sample). The damage threshold defined in figure 3.24 is also visible in the R_a distribution. With increasing power density the surface roughness of the loaded samples increases for RT until 200 °C, but the location of the cracking threshold can be observed. The cracking of the samples has apparently no influence on the roughening of the surface, but above the cracking threshold the R_a values show a minimum for all power densities before they again increase with increasing power densities. This is an indication that the DBTT region is located in this temperature range. Based on these tests it is impossible to determine the sequence of the induced damages, i.e., if thermal shock crack networks are formed before or after roughening takes place. The pulse number dependence of the thermal shock damages will be discussed in subsection 3.4.3.

In figure 3.25b representative linear surface profiles of three different samples are shown. The comparison of the reference sample (black line) with the sample loaded below the damage threshold proofs again that there are no differences in the surface morphology. In contrast to that the sample loaded above the damage threshold and at temperatures above the cracking threshold (blue line) shows significant changes in surface morphology. None of the investigated samples shows swelling of the loaded surface.

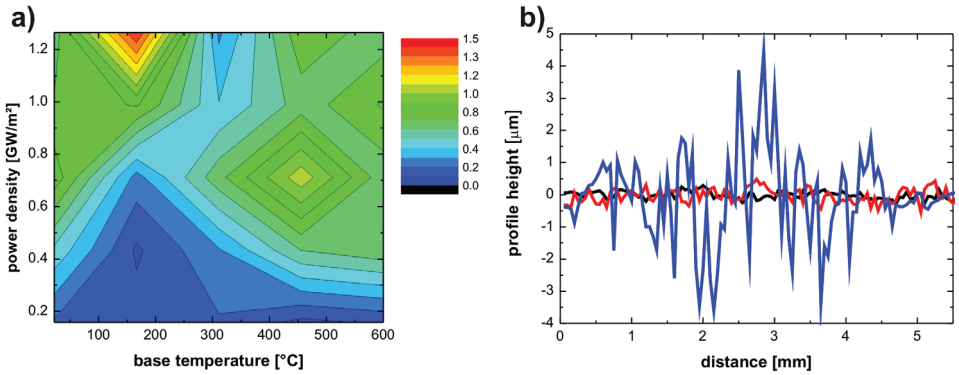

Figure 3.25: Surface roughness of W-UHP L after thermal shock loading; a) Overview of the arithmetic mean roughness R_a in μm of all samples at different power densities and base temperatures, the different values are colour coded; b) Surface profile of W-UHP L at three different testing parameters: no thermal load/reference (black line), below 0.16 GWm^{-2} at RT (red line) and 0.63 GWm^{-2} at 400 °C (blue line).

Based on the thermal shock behaviour of W-UHP L the other two specimen types with modified grain structure were only tested under more specific loading conditions around the damage threshold at 0.16 GWm^{-2} and 0.32 GWm^{-2} as well as below and above the cracking threshold at RT and 400 °C. The results of these test are shown in figure 3.26a for W-UHP with transversal grain structure (W-UHP T; figure 3.16d) and in figure 3.26b for recrystallised W-UHP (W-UHP R; figure 3.16c). The results show that thresholds determined for W-UHP L are not valid for the other grain structures.

The damage threshold of W-UHP T decreases below 0.16 GWm^{-2} at least at RT and the cracking threshold increases above 400 °C base temperature. For W-UHP R the damage threshold also drops below 0.16 GWm^{-2} at RT and shows small discontinuous crack formation at 400 °C. Reasons for the varying threshold values are the significant differences of the mechanical properties depending on the grain structure (subsection 3.1.2). W-UHP T shows brittle behaviour even above 400 °C and very low tensile strength in comparison to W-UHP L. The tensile strength of W-UHP R is reduced

because of the heat treatment which results in a decrease of the damage threshold. However, the material is still able to compensate thermal stresses by plastic deformation without the formation of thermal shock crack networks at 400 °C, but the formation of small cracks indicates that the DBTT increased due to the weakening of the grain boundaries during the recrystallisation process.

The comparison of the R_a values of W-UHP L, T and R outlines that the roughening of the longitudinal and transversal surfaces is very similar or lower for all test conditions. In contrast to that, the roughening of the recrystallised surfaces at 0.32 GWm^{-2} is more than five times bigger at RT and still twice as large at 400 °C. The reasons for these different roughening behaviours are, that the transversal samples have a much higher crack density (subsection 3.4.2) and therefore a stronger reduction of the thermal stresses, while the recrystallised samples have a much smaller yield strength. All measured R_a values are given in appendix C.3.

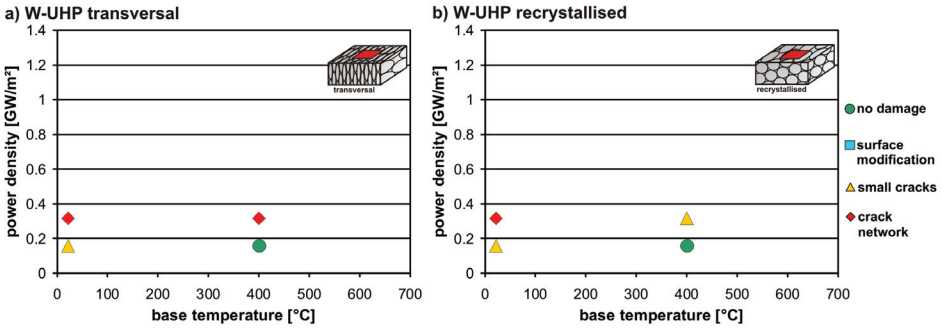

Figure 3.26: Thermal shock response of W-UHP T (a) and W-UHP R (b) after 100 thermal shock events at different power densities and base temperatures.

Pure W

The dependence of the induced thermal shock damages in longitudinal pure W (pure W L; figure 3.16b) after 100 thermal shock events is shown in figure 3.27. Based on this thermal shock damage mapping it is possible to determine two threshold values. The damage threshold is located between 0.16 GWm^{-2} and 0.24 GWm^{-2}. Pure W L can withstand loading conditions below this threshold without any surface modification or damages. Above this threshold damages such as crack networks and surface modifications are induced in dependence on the base temperature. Thermal shock crack networks are only formed in the loaded area for samples at RT. If the material is exposed to thermal shock events at 100 °C or higher only surface modifications like roughening occur. As a result is can be stated that the cracking threshold is located between RT and 100 °C.

A comparison with the thermal shock response and the resulting threshold values of W-UHP L shows that the damage threshold is in the same region while the cracking threshold for pure W L is lower. The major difference between these two materials is the higher amount of foreign atoms and the resulting improvement of the ductility (subsection 3.1.2), while the tensile strength and the grain size are very similar. As a result of the improved ductile behaviour, pure W L is able to compensate induced thermal stresses by plastic deformation at a lower temperature than W-UHP L. However, it still shows severe thermal crack formation at RT.

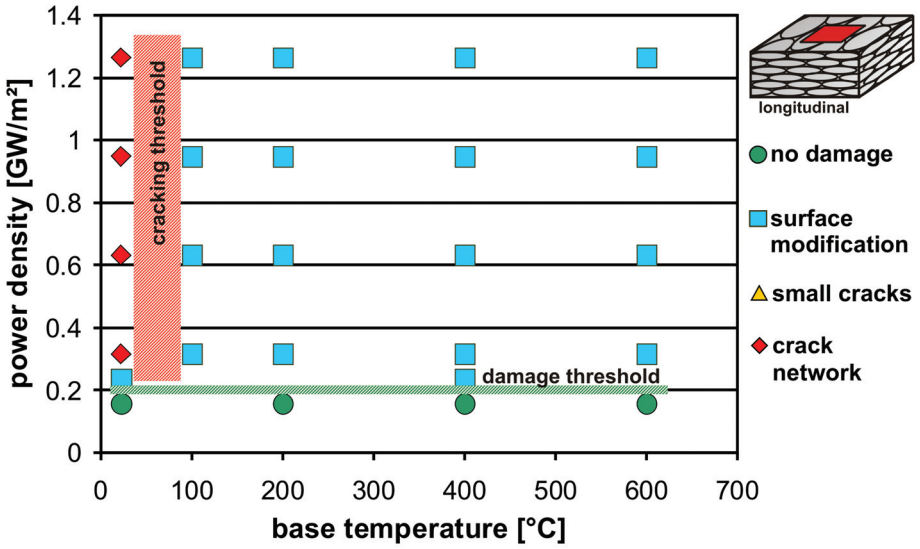

Figure 3.27: Thermal shock response of pure W L after 100 thermal shock events at different power densities and base temperatures. At 0.16 GWm^{-2} and below no visible damage appears. For base temperatures above RT only surface modification occurs.

The laser profilometry results are shown in figure 3.28. An overview of the arithmetic mean roughness R_a for every sample is given in figure 3.28a with an unloaded reference R_a value of 0.13 μm. For power densities below the defined damage threshold of the material no roughening of the loaded surface is observable. With increasing power density and for base temperature above cracking threshold R_a becomes more distinct and reaches its maximum at 1.27 GWm^{-2} and 600 °C. This corresponds to the increase of plastic deformation.

Figure 3.28b shows line scans of the loaded surface at the same loading conditions as for W-UHP L in figure 3.25b. For the reference sample (black line) and the sample loaded

below the damage threshold (red line) the conclusion as for W-UHP L is valid, namely there is no surface roughening below damage threshold. However, the sample loaded above the damage threshold (blue line) shows a pronounced surface roughening and no swelling, which is valid for all investigated samples. In comparison, the roughening for pure W L is less severe as for W-UHP L. This is owed to the improved ductility of the pure W L which allows the material a higher deformation/elongation before it fails.

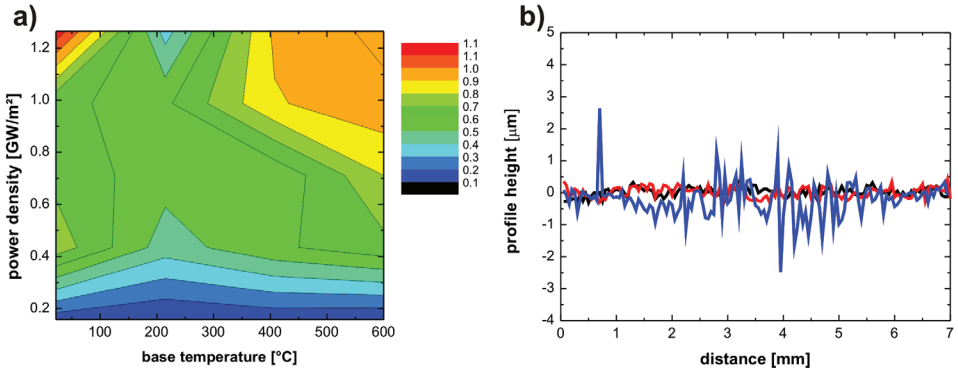

Figure 3.28: Surface roughness of pure W L after thermal shock loading; a) Overview of the arithmetic mean roughness R_a in μm of all samples at different power densities and base temperatures; b) Surface profile of pure W L at three different testing parameters: no thermal load/reference (black line), 0.16 GWm^{-2} at RT (red line) and 0.63 GWm^{-2} at 400 °C (blue line).

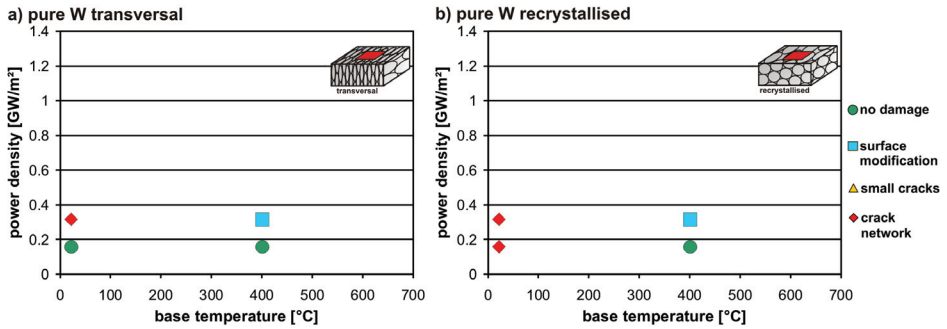

Figure 3.29: Thermal shock response of pure W T (a) and pure W R (b) after 100 thermal shock events at different power densities and base temperatures.

The transversal (figure 3.16d) and recrystallised (figure 3.16c) grain structures of pure W were also tested under the same loading conditions as for the W-UHP samples. In

figure 3.29a and b the results of these tests are shown. The threshold values of pure W T are located at the same positions as for the longitudinal grain orientation, while the damage threshold of pure W R decreases below 0.16 GWm^{-2} at RT as for W-UHP R. Especially the different behaviour of pure W T compared to W-UHP T is surprising. The cycle dependence of the induced thermal shock damages could be an explanation for this behaviour, which will be discussed in subsection 3.4.3 in more detail.

The comparison of the R_a values of pure W L, T and R gives the same general behaviour as it was observed for W-UHP. The roughening of the longitudinal and transversal surfaces is very similar or a bit smaller for the transversal for all test conditions. In contrast to that, the roughening of the recrystallised surfaces is twice as pronounced as for the other grain orientations, due to the same effects as explained for W-UHP. All measured R_a values are given in appendix C.3.

WVMW

The results of the thermal shock test with WVMW L (figure 3.16b) are presented in figure 3.30. The induced damages vary with the testing conditions. That allows the localisation of the damage and cracking threshold.

The damage threshold is located below 0.24 GWm^{-2} without any base temperature dependence. This corresponds to the materials tested before. For higher applied power densities, beside thermal shock crack networks and surface roughening, there was a third kind of surface damage induced in the loaded area. Small discontinuous and arbitrarily distributed cracks can be observed in the loaded area at base temperatures of 100 °C and 200 °C. Thermal shock crack networks only occur at RT and for base temperatures $\geq$ 300 °C the material modification is determined only by surface roughening. The cracking threshold of WVMW L is located between 200 °C and 300 °C due to this damage behaviour.

WVMW L shows the same or at least very similar mechanical properties as W-UHP L concerning tensile strength and fracture strain (subsection 3.1.2). This explains the agreement of the damage thresholds but not the much higher base temperature value for the cracking threshold. This is even above the value for W-UHP L, although this grade has a worse ductile behaviour than WVMW L. The increase of the cracking threshold can be explained by the smaller grain sizes of WVMW in comparison to the pure grades, due to the potassium doping (subsection 3.1.1). This results in an increase of the grain boundary density at the loaded surface and reduced resilience against initial crack formation. This assumption is supported by the change of the crack pattern with increasing base temperature. The formation of thermal shock crack networks at RT, according to W-UHP L and pure W L, is replaced by small cracks and changes into roughening of the surface with increasing temperature and ductility of the material.

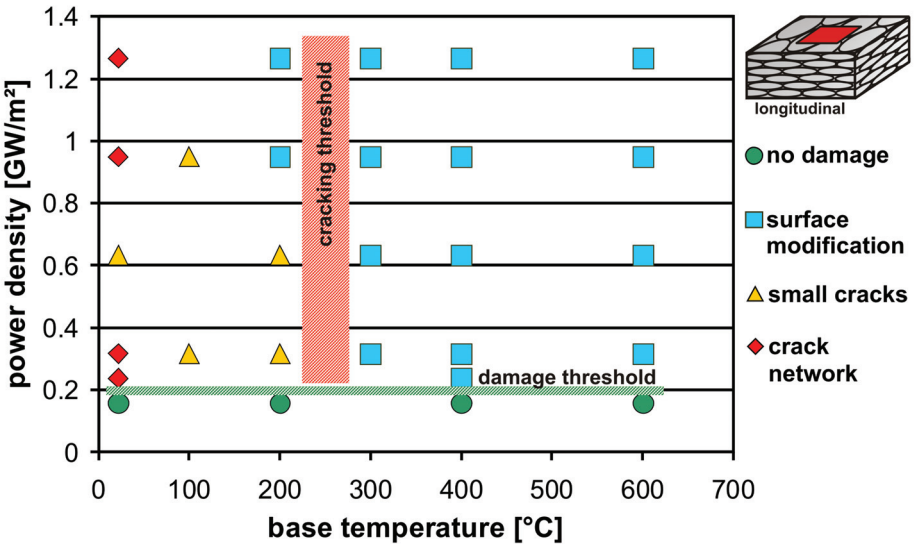

Figure 3.30: Thermal shock response of WVMW L after 100 thermal shock events. No visible damages are induced at 0.16 GWm^{-2} and below for all base temperatures. Thermal shock crack networks are formed at RT and change into small discontinuous cracks for temperatures up to 200 °C. Above this temperature only surface modifications occur.

Figure 3.31 shows the results of the laser profilometry. The arithmetic mean roughness R_a for every sample is plotted in figure 3.31a and representative examples of different surface profiles are shown in figure 3.31b. The reference R_a of an unloaded surface is 0.07 μm.

The overview of the R_a in dependence on the loading conditions shows that below the damage threshold no surface roughness occurs. In contrast to pure W the surface roughening of WVMW is less severe and this becomes even more obvious in comparison to W-UHP (cf. figures 3.31b and 3.25b). Main reasons for these differences are the combination of a more ductile behaviour at elevated temperatures and the very small grain sizes in comparison to the purer materials. These differences in surface modifications are also discernible in the surface profiles shown in figure 3.31b. The sample loaded below the damage threshold (red line) shows no deviation from the unloaded surface (black line), while the sample loaded above the damage threshold shows roughening, but not as severe as for the pure materials.

The transversal (figure 3.16d) and recrystallised (figure 3.16c) grain structures of WVMW were tested under the same loading conditions as for the materials before.

In figure 3.32a and b the results of these tests are shown. The threshold values for both grain orientations are located at the same positions as for the corresponding grain orientations in W-UHP. Also the general behaviour of the R_a values for WVMW L, T and R is the same as for W-UHP. While the roughening of the longitudinal and transversal samples is very similar, the recrystallised samples show an at least twice as high arithmetic mean roughness. All measured R_a values are given in appendix C.3.

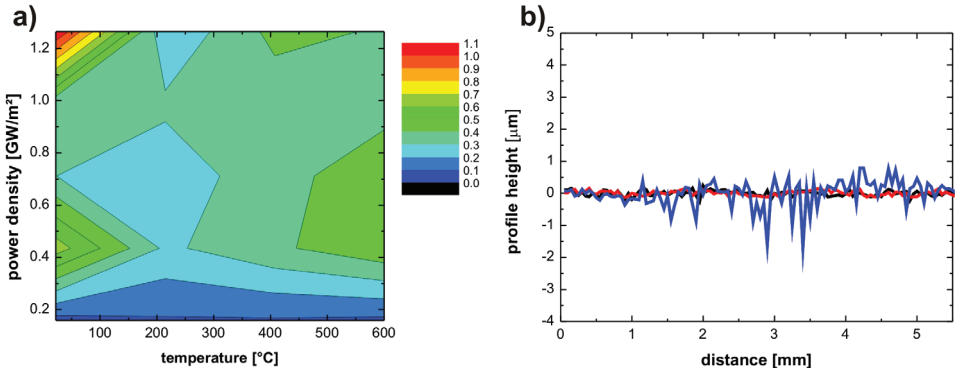

Figure 3.31: Surface roughness of WVMW L after thermal loading; a) Overview of the arithmetic mean roughness R_a in μm of all samples at different power densities and base temperatures; b) Surface profile of WVMW L at three different testing parameters: no thermal load/reference (black line), 0.16 GWm^{-2} at RT (red line) and 0.63 GWm^{-2} at 400 °C (blue line).

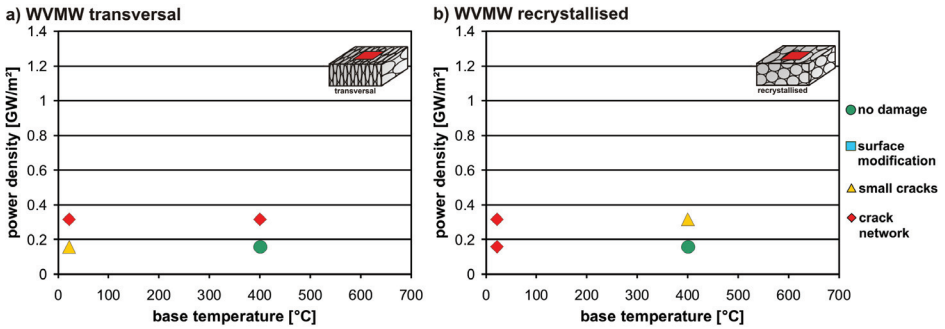

Figure 3.32: Thermal shock response of WVMW T (a) and WVMW R (b) after 100 thermal shock events at different power densities and base temperatures.

WTa1

Figure 3.33 gives an overview of the different damages that were induced on WTa1 L specimens (figure 3.16b) during the thermal shock tests in dependence on the test parameters.

No visible damages occur below 0.24 GWm^{-2} at elevated temperatures and at RT even below 0.32 GWm^{-2}. In this region the damage threshold for WTa1 is located. Thermal shock crack networks are formed for power densities of 0.63 GWm^{-2} and above at RT. At a base temperature of 200 °C small cracks are induced which merge into thermal shock crack networks with increasing power density. For samples loaded at base temperatures above 200 °C only surface modification occurs, which leads to a cracking threshold between 200 °C and 300 °C.

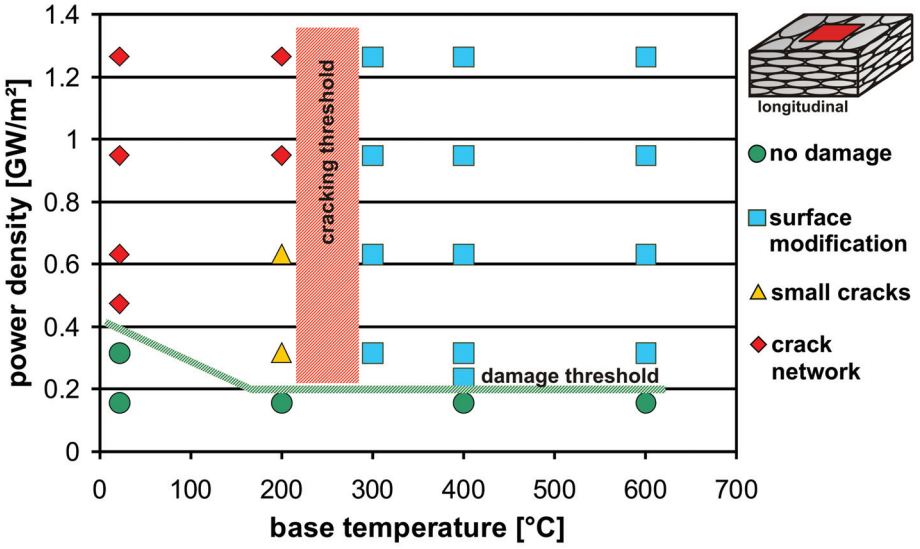

Figure 3.33: Material damage and surface modification of WTa1 L after thermal shock testing. The damage threshold is located between 0.24 GWm^{-2} and 0.32 GWm^{-2} at RT and between 0.16 GWm^{-2} and 0.24 GWm^{-2} at elevated temperatures. Crack networks occur for base temperatures up to 200 °C.

The location of the thresholds are very similar to the values for WVMW L. This similarity is confirmed by the comparison of the identified parameters which influence the thermal shock response of tungsten such as tensile strength, fracture strain, grain size and structure. The deviations in the thermal shock responds of WTa1 L and WVMW L like the formation of thermal shock cracks at 200 °C and the increased damage threshold at RT can be traced back to the slight differences in the before mentioned

parameters. An even smaller average grain size of WTa1 reduces the resilience against initial crack formation again. This effect is intensified by the reduced fracture strain of WTa1. The slightly higher tensile strength is not sufficient to compensate these effects, but results in an increase of the damage threshold at least at RT. The combination of these changes in material parameter results in a thermal shock crack network formation even at 200 °C in contrast to WVMW L.

The results of the surface characterisation via laser profilometry are presented in figure 3.34 with an unloaded reference value of 0.1 μm. The distribution of the arithmetic mean roughness R_a in dependence on the testing parameters is shown in figure 3.34a. Below the damage threshold no significant surface roughness occurs. With increasing power density the surface roughness increases, but is less pronounced in comparison to the pure materials as it was also observed for WVMW L. The reason for this is the even smaller grain size and the resulting reduction of possible induced stresses inside an individual grain.

Figure 3.34b compares different representative surface profiles. It is shown that at low power densities (red line) no modifications occur in comparison to the unloaded one (black line). At higher power densities (blue line) surface roughness occurs, but again less severe than for the before presented pure materials.

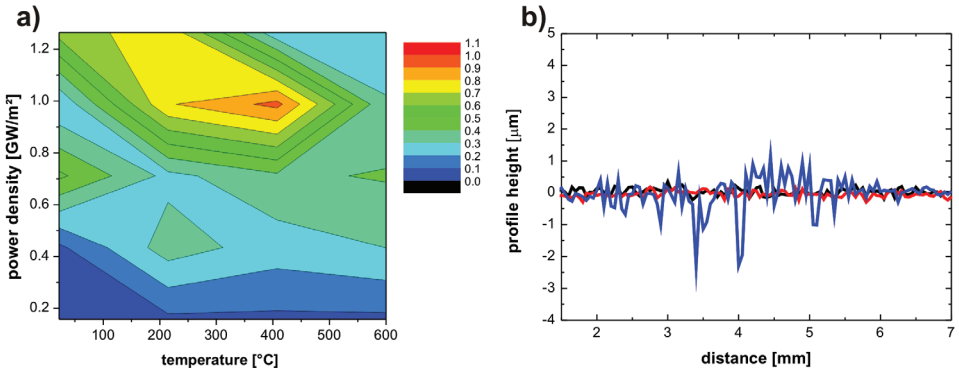

Figure 3.34: Surface roughness of WTa1 L after thermal loading; a) Overview of the arithmetic mean roughness R_a in μm of all samples at different power densities and base temperatures; b) Surface profile of WTa1 at three different testing parameters: no thermal load/reference (black line), 0.16 GWm^{-2} at RT (red line) and 0.63 GWm^{-2} at 400 °C (blue line).

An overview of the thermal shock response of the transversal (figure 3.16d) and recrystallised (figure 3.16d) grain orientation is shown in figure 3.35a and b. The damage mapping shows no significant differences in comparison to the reference material. All

damage thresholds are located in the same regions as for W-UHP, except the cracking threshold of the recrystallised material is below 400 °C, which can be explained with the higher UTS. The changes in surface roughness are also the same. There is no difference in the arithmetic mean roughness of the longitudinal and transversal samples, while the values show a significant increase for the recrystallised grain structure. All measured R_a values are given in appendix C.3.

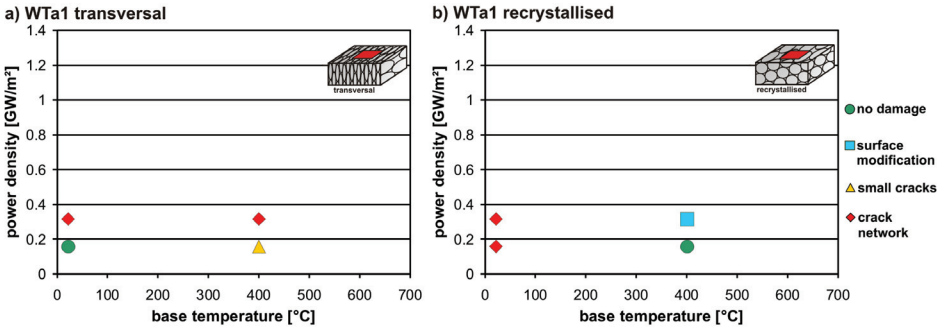

Figure 3.35: Thermal shock response of WTa1 T (a) and WTa1 R (b) after 100 thermal shock events at different power densities and base temperatures.

WTa5

An overview of the induced surface modifications and damages during the thermal shock testing of WTa5 L (figure 3.16b) is presented in figure 3.36. The damage threshold is located between 0.32 GWm^{-2} and 0.48 GWm^{-2}. Below this threshold no visible damages or modifications are induced on the samples surfaces. At RT and power densities above the damage threshold thermal shock networks are formed. If the base temperature is increased additionally the formation of crack networks will stop and only surface modifications will occur. Due to that the cracking threshold is located between RT and 100 °C.

Referring to these threshold values WTa5 L shows the most significant differences in comparison to the other tungsten grades. The cracking threshold is the lowest together with pure W L and even more remarkable is the nearly twice as high damage threshold in comparison to the other investigated tungsten grades. The very high tensile strength, which is twice as high as for the pure materials for the longitudinal grain orientation (3.1.2), is a reason for the improved ability to withstand thermally induced stresses and the resulting damages. The combination of this high tensile strength with an improved ductile behaviour at elevated temperatures results also in a low cracking threshold.

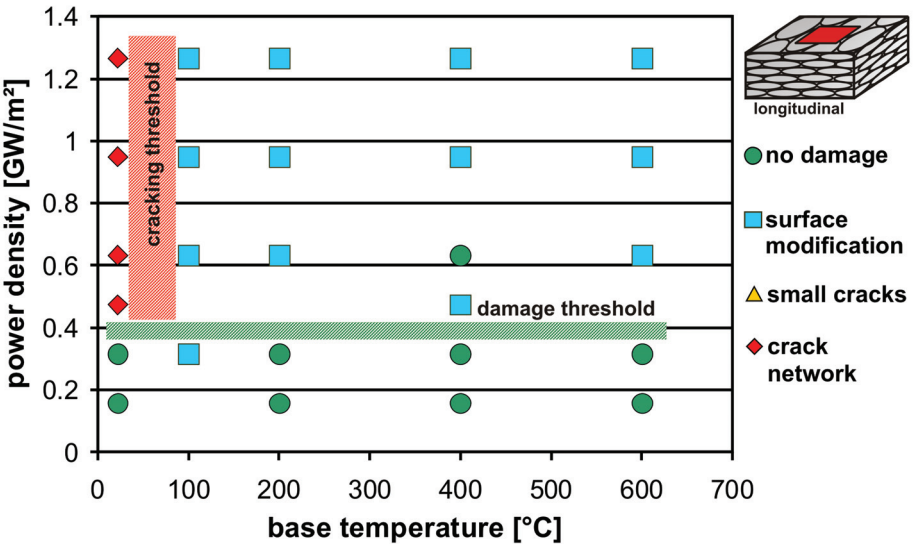

Figure 3.36: Overview of different surface modifications and damages of WTa5 L induced by cyclic thermal shock loading. Below a power density of 0.32 GWm^{-2} no visible damages appear. Crack networks are formed at higher power densities but only at RT. Only surface modification occurs at elevated temperatures.

The results of the laser profilometry scans of the loaded surfaces are shown in figure 3.37. An overview of the arithmetic mean roughness R_a in dependence on the loading conditions is given in figure 3.37a with a reference value for an unloaded surface of 0.07 μm. No surface modifications are measured below 0.48 GWm^{-2} at RT and for even higher power densities at elevated temperatures. This corresponds to the high damage threshold for this grade as observed in figure 3.36. The value of the arithmetic mean roughness at RT and 1.26 GWm^{-2} is not plotted, because the value exceeds the chosen range of values due to severe crack formation. For a better comparability with the other tungsten grades the range of values was not adjusted.

Figure 3.37b shows three different surface profiles. It is obvious that below the damage threshold (red line) no changes in surface height occur. At higher power densities (blue line) the changes become significant in comparison to the reference (black line). In contrast to the other four tungsten grades the representative line scan of the roughened sample is taken at higher power densities, because of the higher damage threshold. But the general damage behaviour observed for all investigated tungsten grades in this work is also valid for WTa5 L. Surface modifications due to thermal shock loading are limited to roughening and the samples show no swelling effects.

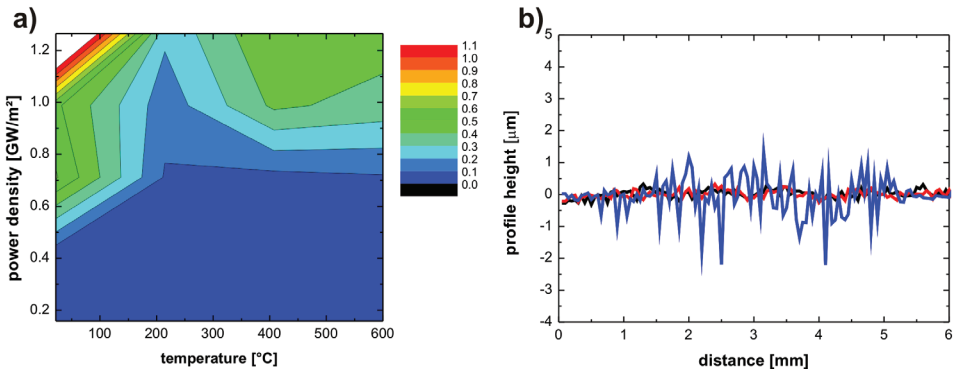

Figure 3.37: Surface roughness of WTa5 L after thermal shock loading; a) Overview of the arithmetic mean roughness R_a in μm of all samples at different power densities and base temperatures, the roughness value at RT and 1.26 GWm^{-2} exceeds the chosen range of values and therefore is not plotted; b) Surface profile of WTa1 at three different testing parameters: no thermal load/reference (black line), 0.16 GWm^{-2} at RT (red line) and 1.26 GWm^{-2} at 400 °C (blue line).

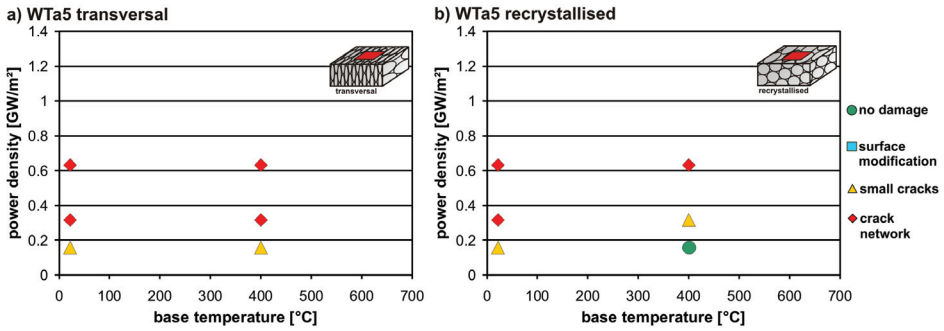

Figure 3.38: Thermal shock response of WTa5 T (a) and WTa5 R (b) after 100 thermal shock events at different power densities and base temperatures.

Because of the higher damage threshold, the investigation of the transversal (figure 3.16d) and recrystallised (figure 3.16d) grain orientations was performed in a broader power density range between 0.16 GWm^{-2} and 0.63 GWm^{-2}, but base temperatures maintained at RT and 400 °C. The results of these experiments are shown in figure 3.38. Contrary to WTa5 L, the samples WTa5 T and WTa5 R show a worse damage behaviour under thermal shock loads. The damage threshold decreases below 0.16 GWm^{-2} and the cracking threshold increases above 400 °C, but thermal shock

crack are also observed for the recrystallised material. This was never the case for the other recrystallised tungsten grades. However, these recrystallised grades were not exposed to 0.63 GWm^{-2}. The significant improvement of mechanical properties of one grain orientation seems to result in a severe degradation for the other one and even influences the material behaviour after recrystallisation. All measured R_a values are given in appendix C.3.

3.4.2 Investigation of thermal shock crack networks

The investigations of thermal shock crack networks are divided in two parts and the measured crack parameters are defined as shown in figure 3.23.

Power density dependence of thermal shock cracks

The dependence of the crack parameters on the absorbed power densities for all investigated tungsten grades with longitudinal grain orientation at RT is shown in figure 3.39. All three parameters, crack distance (figure 3.39a), crack width (figure 3.39b) and crack depth (figure 3.39c), grow with increasing power density for all materials. For pure W and WVMW this increasing trend is not so distinct for the crack distances, due to the higher plasticity of both materials, which has a strong influence on the crack formation and will be discussed in more detail in subsection 3.4.3. Also the crack width values show a less clear dependence on the absorbed power densities for all tungsten grades, because of the before mentioned low statistics. However, it is still visible and corresponds very well with the increase of the crack distance. As a consequence of the higher power density at constant pulse duration the materials have to compensate higher thermal stresses and higher strain rates. Due to the higher strain rate the tensile strength and fracture toughness of the material improves [97, 98]. Hence less cracks are formed which results in a lower crack density (inverse crack distance) but a larger crack width to maintain the same open volume. The remaining thermal stresses are not high enough to cause additional crack formation. The dependence of the crack density on the tensile strength is supported by the development of the crack distance and width of WTa5, which has the highest tensile strength of all investigated tungsten grades (subsection 3.1.2). Both parameters increase, but the crack distances are among the smallest, while the crack widths are among of the largest, especially at 1.27 GWm^{-2}.

In order to verify brittle crack formation the crack distances were compared with the grain diameter. For all tungsten grades the minimum crack distance was larger than the maximum grain diameter. In contrast to thermal fatigue induced crack formation, the crack distances and grain diameters are not directly related. The increase of the crack depth can be explained with the higher stresses at higher power densities. But while the crack depth for W-UHP, pure W and WVMW are all in the same range, the crack depth decreases with an increasing amount of tantalum. The crack depths of WTa1 are only a bit smaller than the other three, while WTa5 shows significant differences and has the

smallest values for all power densities. As shown in subsection 3.1.3, the alloying with tantalum has a strong influence on the thermal conductivity of tungsten. It decreases significantly with an increasing amount of tantalum. Consequently, a lower thermal conductivity leads to a steeper temperature gradient. Therefore the temperature and the induced thermal stresses do not propagate so deep into the material during the thermal shock which results in a smaller crack penetration depth.

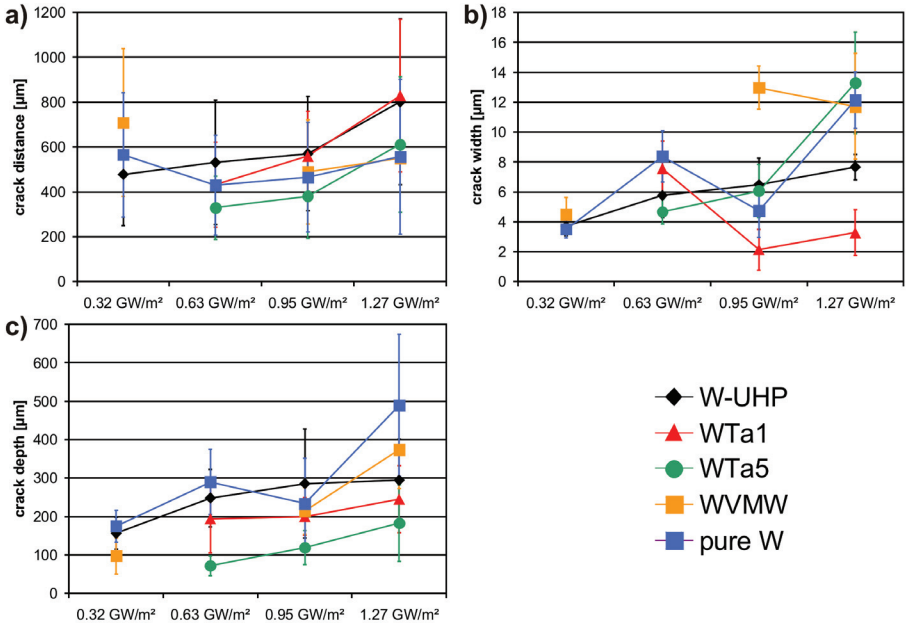

Figure 3.39: Power density dependence of crack parameters for all investigated tungsten grades with the longitudinal grain orientation: a) crack distance; b) crack width; c) crack depth.

Beside the thermal and mechanical properties, also the microstructure has a significant influence on the cracking behaviour and especially on the crack propagation. To clarify that, figure 3.40 shows representative cross sections of W-UHP (figure 3.40a) and WTa5 (figure 3.40b) at RT and 1.27 GWm^{-2}. The thermal shock cracks propagate perpendicular to the loaded surface into the material. They stop at a certain depth and start propagating parallel to the loaded surface. This kind of crack propagation was observed for all tungsten grades with a longitudinal grain orientation loaded in the range below the respective cracking threshold. Furthermore the crack propagation depends on the grain orientation and size. Cracks parallel to the loaded surface propagate predominantly intergranular into the material, while cracks perpendicular to the loaded surface show also transgranular crack propagation. For tungsten grades with larger grains such as W-UHP and pure W transgranular crack propagation is

more pronounced than for the other three with significantly smaller grains, because for small grain much smaller changes of the propagation direction are necessary to follow the grain boundaries. The cracking parallel to the loaded surface is a severe problem. These parallel cracks act as a thermal barrier and will, with increasing pulse number, lead to an overheating of the material surface. In the worst case the material will melt and/or whole surface parts will be eroded and contaminate the plasma. This is confirmed by visible recrystallisation and erosion of the surface near regions in figure 3.40b and the corresponding top view shown in figure 3.40c. There are small molten areas near the crack edges (black arrows), although the surface temperature during the thermal shock event stays below the melting temperature of tungsten (section 3.3).

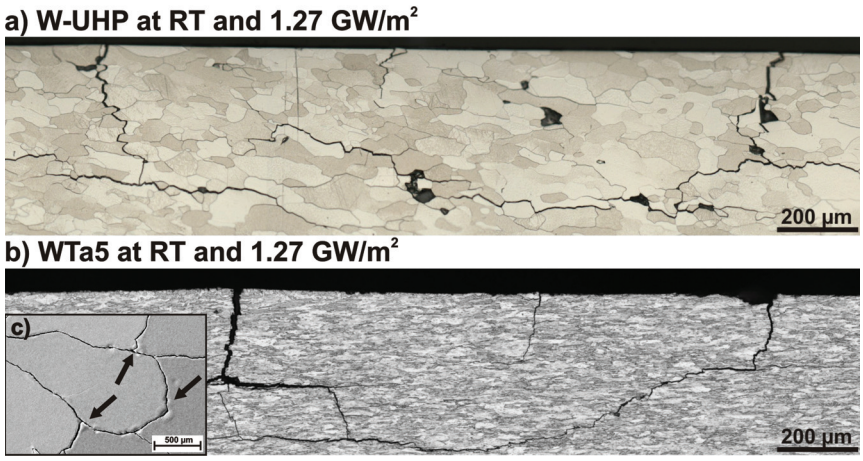

Figure 3.40: Cross section of W-UHP (a) and WTa5 (b) at RT and 1.27 GWm^{-2} and SEM top view image of the same WTa5 sample (c).

Comparison of longitudinal, transversal and recrystallised grain orientations

The pattern of the induced thermal shock crack networks depends not only on the mechanical and thermal properties of a material but also on their microstructure. In the previous subsection only the longitudinal grain orientation and their influence on the crack formation and pattern was investigated. Now all three grain structures will be investigated and compared with each other. Therefore, figure 3.41 and 3.42 give an overview of the thermal shock crack networks in dependence on different grain orientations.

A general comparison of the loaded surfaces presented in figure 3.41 shows, that the pattern of the crack networks for the longitudinal (left column) and recrystallised (right column) samples are very similar. The cracks form an arbitrary crack network within the loaded surface area. In contrast to that, the thermal shock crack networks of the

transversal samples show a completely different pattern. The cracks clearly follow the grain orientation. They are arranged parallel to each other and sometimes connected via nearly perpendicular cracks. A closer investigation of the crack networks and the loaded surfaces reveals even more differences. The crack density of the transversal samples is more than twice as high as for the longitudinal samples, at least in the direction perpendicular to the grain orientation (deformation direction). The crack density of the recrystallised samples is similar or lower than for the longitudinal samples. The differences in crack width according to the grain structure correspond to the crack densities. A higher crack density for the transversal samples is combined with a decrease of the crack width and vice versa for the recrystallised materials. A detailed overview of all crack parameter values is given in appendix C.4. Additionally, there are differences in the arithmetic mean roughness of the loaded surfaces. It decreases for the transversal and increases for the recrystallised materials as it was already discussed in section 3.4.1.

Beside the investigation of the cracked surfaces also the crack propagation into the materials and the influence of the different grain structures on the propagation was investigated (figure 3.42). Longitudinal and recrystallised materials show again a very similar behaviour. The thermal shock cracks propagate intergranular and transgranular perpendicular to the loaded surface into the materials, stop at a certain depth and continue to grow parallel to the loaded surface. However, there is no crack propagation parallel to the loaded surface for the transversal grain orientation. The cracks propagate along the grain boundaries and stop at a certain depth. A comparison of the crack depths shows that the average values for the longitudinal and transversal grain orientation are very similar, while the cracks propagate much deeper into the material for the recrystallised state. It is also important to mention the significant grain loss during the preparation of the cross section of the recrystallised samples. This grain loss could not be observed during the sample preparation of longitudinal or transversal specimens. It also seems to depend on the grain size after the recrystallisation, because for larger recrystallised grains (W-UHP) a grain loss was also not observed. That leads to the conclusion that recrystallised materials with smaller grains have a poor cohesion between single grains and are more prone to loss. The reason for this low cohesion is the agglomeration of vacancies at the grain boundaries during the recrystallisation process and the resulting increase of open volume between adjacent grains [99]. The observed differences in crack pattern and propagation are a result of the varying mechanical properties due to the grain structure. Transversal grain orientation leads to significant increase of crack densities, but reduces the roughening of the surface and the risk of parallel crack formation. Longitudinal and recrystallised materials show a very similar behaviour at the first glance. Closer investigations show that for the recrystallised samples the cracks propagate much deeper into the material and the risk of complete grain erosion increases significantly as a result of a reduced cohesion between grains. This risk is reduced with increasing grain size (W-UHP) or due to strengthening of grain boundaries (WVMW).

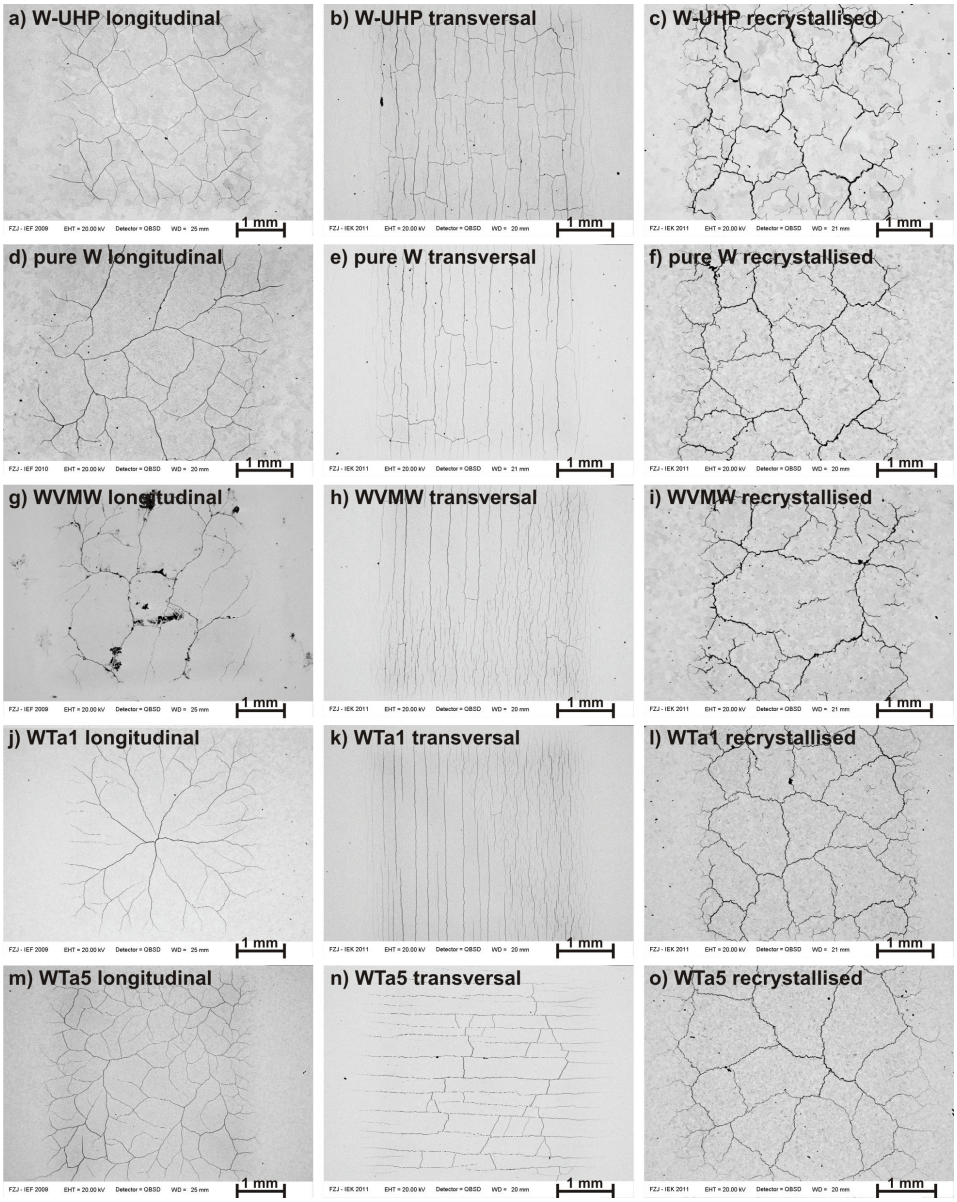

Figure 3.41: SEM images of loaded surfaces of all investigated tungsten grades with longitudinal (left column), transversal (middle column) and recrystallised (right column) grain structure. All samples were loaded at RT and 0.32 GWm^{-2}, except the samples in j), m), n) and o). These samples were loaded at RT and 0.63 GWm^{-2}. The grain orientation in n) is rotated by 90° compared to b), e), h) and k). Corresponding crack parameter values can be found in appendix C.4.

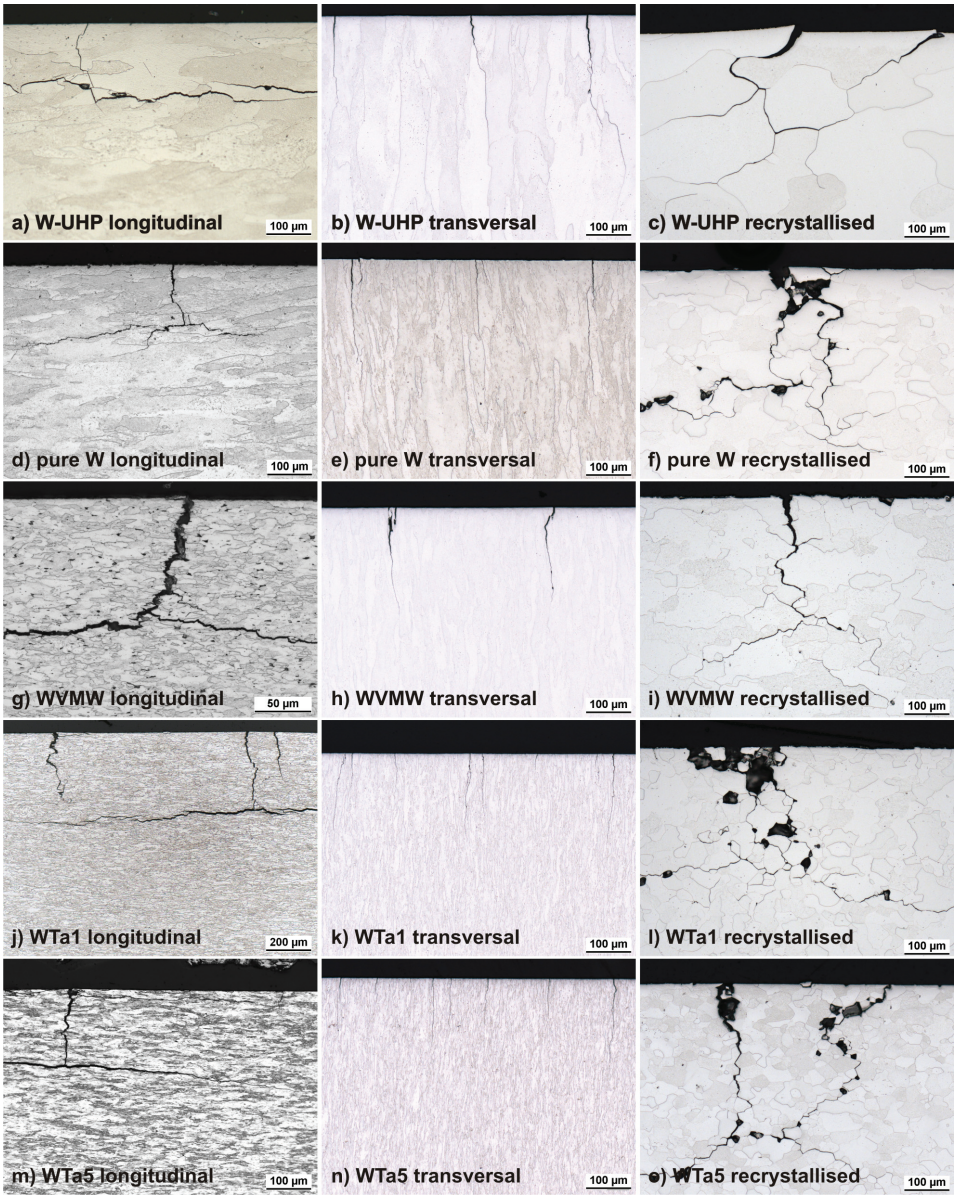

Figure 3.42: LM images of sample cross sections of all investigated tungsten grades with longitudinal (left column), transversal (middle column) and recrystallised (right column) grain structure. All samples were loaded at RT and 0.32 GWm^{-2}, except the samples in j), m), n) and o). These samples were loaded at RT and 0.63 GWm^{-2}. Corresponding crack parameter values can be found in appendix C.4.

3.4.3 Pulse number dependent thermal shock performance

The investigation of the thermal shock response in dependence on the number of pulses was done at a constant power density of 0.95 GWm^{-2} at RT. This test condition was chosen because the damage mapping for 100 pulses, presented in subsection 3.4.1, shows that for all investigated tungsten grades thermal shock crack networks are formed and a well pronounced surface roughening is induced under these loading conditions. Additional to the investigation at 100 pulses, all tungsten grades were exposed to 1, 10 and 1000 pulses at longitudinal grain orientation. The induced damages on each sample were classified and characterised as explained in section 3.4.

Based on the obtained results shown in figure 3.43 the investigated tungsten grades can be divided into two groups. The first group shows thermal shock crack formation already after the first pulse and consist of W-UHP, WTa1 and WTa5. In contrast to that, the second group, consisting of pure W and WVMW, stays completely undamaged after the first pulse and shows only surface roughening after 10 pulses. Thermal shock crack networks are observed for 100 pulses and higher. The reason for this could be the variation of the mechanical properties. Pure W and WVMW have the largest fracture strains for the longitudinal grain orientation. Due to this increased plasticity the materials are able to compensate the thermal stresses without any visible surface modification (1 pulse) or via a microscopically detectable plastic deformation (10 pulses). Pulse numbers above 10 are necessary to accumulate enough material damage to cause crack formation.

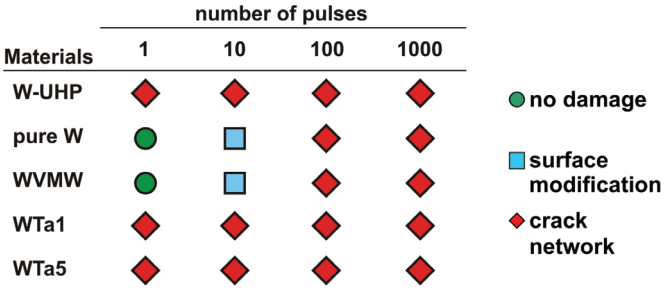

Figure 3.43: Induced thermal shock damage in dependence on the number of pulses of all investigated tungsten grades exposed to 0.95 GWm^{-2} at RT.

Furthermore the crack parameters such as distance, width and depth defined in section 3.4 were determined. Their pulse number dependence is shown in figure 3.44. As a result it can be stated that independent from the tungsten grade none of the crack parameters shows any dependence on the pulse number. The only observable increase of a crack parameter value is the crack width of W-UHP after 1000 pulses. However, this increase can be assessed as a statistical deviation due to already mentioned problems

to achieve statistically firm data (see section 3.4) and a corresponding increase of the crack distances for W-UHP as it was observed in subsection 3.4.2.

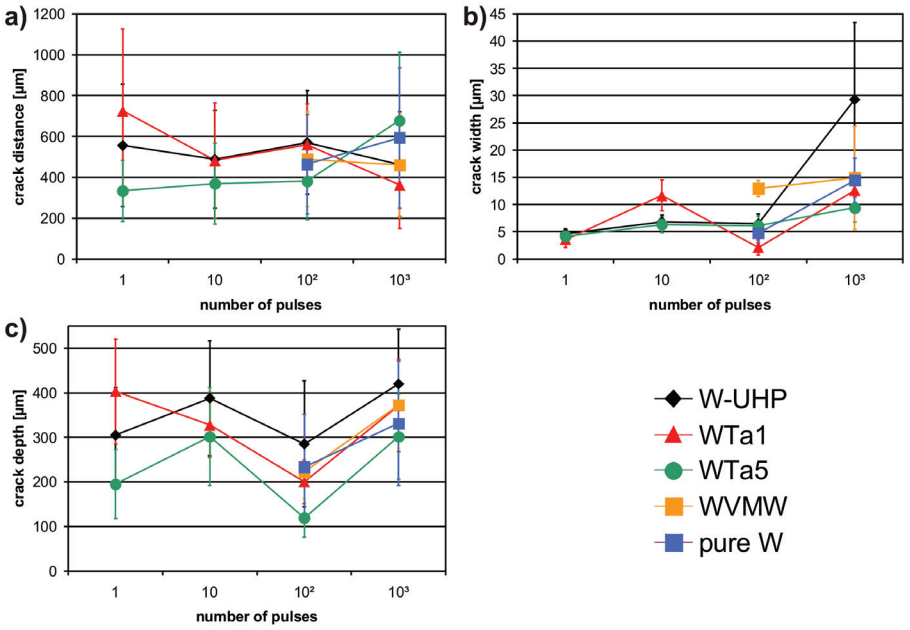

Figure 3.44: Pulse number dependence of crack parameters for all investigated tungsten grades with the longitudinal grain orientation exposed to 0.95 GWm^{-2} at RT: a) crack distance; b) crack width; c) crack depth.

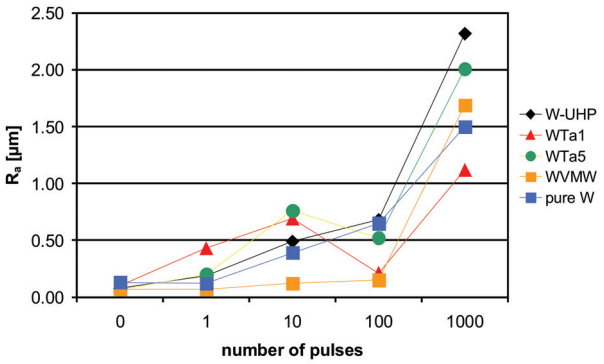

Figure 3.45: Pulse number dependence of the arithmetic mean roughness for all investigated tungsten grades with longitudinal grain orientation exposed to 0.95 GWm^{-2} at RT.

In contrast to the independence of the crack parameters from the number of pulses, the arithmetic mean roughness R_a of the loaded surfaces shows a significant increase with increasing pulse numbers. This dependence is shown in figure 3.45 and valid for all investigated tungsten grades. That means, even if thermal stresses are reduced by crack formation, the uncracked regions of the loaded area will continuously accumulate damages which result in stronger roughening. This behaviour has been found to be a very severe problem at higher pulse numbers [100]. The increasing amount of plastic deformation will lead to thermal fatigue effects such as transgranular crack formation and material erosion as well as melting effects, especially at high power densities.

3.4.4 Comparison of damages induced by laser and electron beam

W-UHP samples with longitudinal grain orientation were not only exposed to an electron beam, but also to a laser beam (subsection 2.3.4) as described in section 3.2. An overview of the sample surfaces after electron and laser beam loading is given in figure 3.46. The general damage behaviour of tungsten for both simulation methods is the same. At power densities of 0.19 GWm^{-2} the samples (figure 3.46a and f) show no changes in the surface morphology, which correspond to the damage thresholds of W-UHP L described in subsection 3.4.1. For higher power densities thermal shock crack networks are induced on every sample and independent of the simulation method.

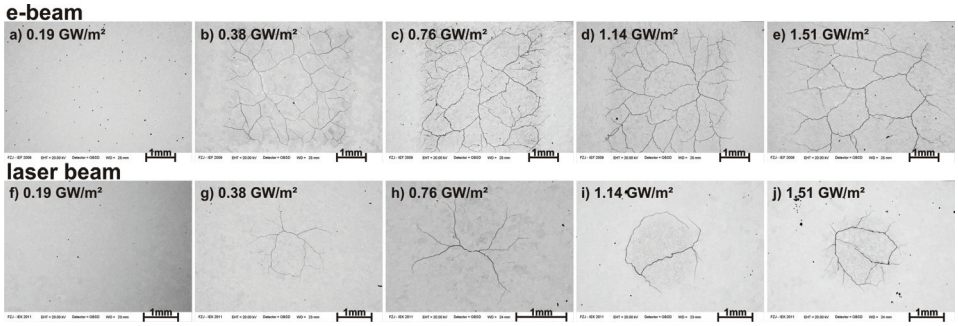

Figure 3.46: SEM images of the loaded surfaces after exposure to electron (first line) and laser (second line) beam at RT and different power densities.

The thermal shock crack networks induced by electron and laser beam show some differences in crack pattern and size of the cracked area. These obvious differences are a result of geometric effects such as the shape and the size of the loaded areas. A square of 4 x 4 mm^2 is scanned by the electron beam, while the laser beam loads a circular spot with a diameter of 2 mm which results in different power density gradients at the edges of the loaded areas. Additionally to these differences visible to the naked eye, the crack parameters defined in section 3.4 were determined and are depicted in figure 3.47.

All three parameters are very similar for both simulation methods at power densities of up to 0.76 GWm^{-2}. For higher power densities the deviation becomes larger, but the values are still within their respective error margin except the crack depth at 1.51 GWm^{-2}. The deviations are attributed to the problems to achieve statistically firm data mentioned in section 3.4, which becomes even more pronounced because of the even smaller loaded area for the laser experiments and the therefore limited number of observable cracks.

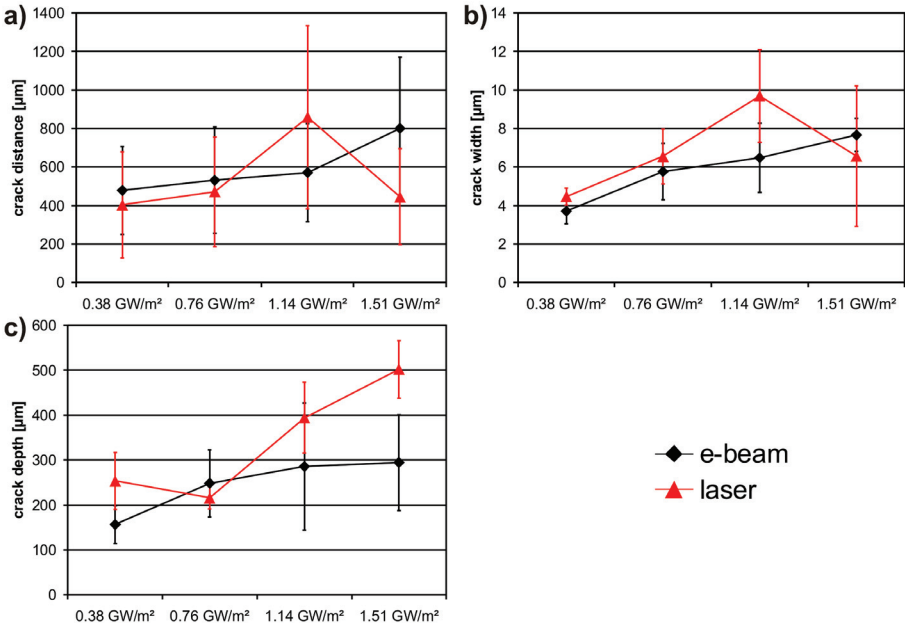

Figure 3.47: Power density dependence of crack parameters induced by electron (black diamond) and laser (red triangle) beam for W-UHP with longitudinal grain orientation: a) crack distance; b) crack width; c) crack depth.

Beside the determination of the crack parameters also the pattern of the crack propagation into the bulk material was investigated. Figure 3.48 shows two representative cross sections after electron (figure 3.48a) and laser (figure 3.48b) beam exposure. Independent of the simulation method and the loading conditions it can be stated that the thermal shock crack first grows perpendicular to the loaded surface, stops at a certain depth and than propagates parallel to the surface. This behaviour and the reasons for that were already explained in detail in subsection 3.4.2 and all of them are also valid for the thermal shock crack induced by a laser beam. The apparently less pronounced cracking parallel to the surface has the same reason as the differences of crack pattern on the surface. A much smaller and circular loaded area in case of the laser beam results in a modified thermal stress distribution.

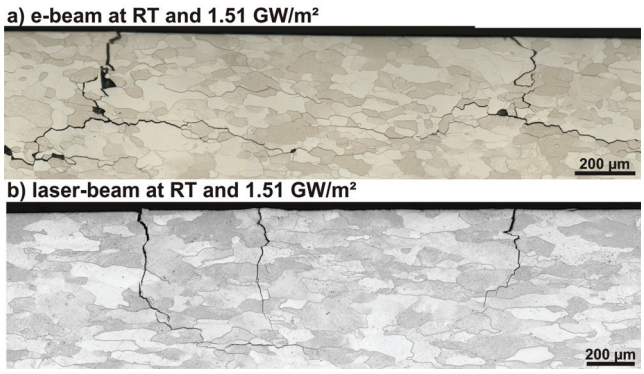

Figure 3.48: Cross section of W-UHP exposed to 100 electron (a) and laser (b) beam pulses at RT and 1.51 GWm^{-2}.

Those changes in geometry and size of the loaded areas and the resulting differences in power density gradients at the edges might also be the reason for the different surface modifications of the electron and laser beam loaded samples. Figure 3.49 shows the power density dependence of the arithmetic mean roughness R_a for both simulation methods and an unloaded reference value of 0.08 μm. The roughness of the electron beam loaded surfaces increases very fast and than stays more or less constant, while the behaviour of the laser exposed samples is quite different. They only show a slight increase at low power densities and increase very fast to a value twice a high as the maximum of the electron beam loaded samples. The homogeneous exposure by the laser in contrast to the scanning in case of the electron beam could be an additional reason for this.

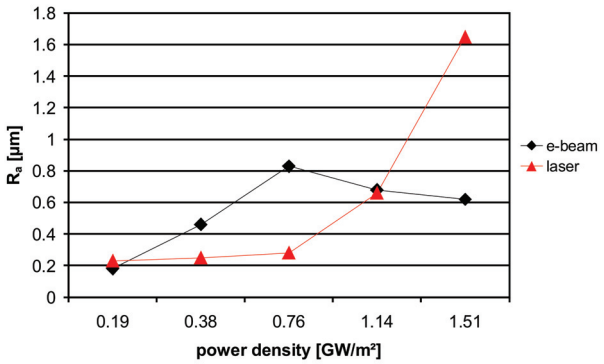

Figure 3.49: Power density dependence of the arithmetic mean roughness for W-UHP with longitudinal grain orientation after electron and laser beam exposure. Unloaded reference value is 0.08 μm.

3.5 Summary and conclusion

The two general mechanisms occur during a thermal shock event and are responsible for different kinds of surface modifications. First, a transient thermal load is applied to the specimen and induces thermal stresses at the surface of the material. Due to the rapid heating the affected surface area expands. The expansion is limited by the colder surrounding and interior material. This leads to compressive stresses which induce plastic deformation. Second, after the rapid heating the area cools down and the surface stresses are reversed into tensile stresses. These stresses can be compensated by plastic deformation (surface modifications/roughening) if the material is ductile. For a brittle material these stresses lead to serious surface damages such as cracks and crack networks, especially for high tensile stresses during the cool down.

The results presented in subsection 3.4.1 show that damages and surface modifications induced by thermal shock loads strongly depend on the test parameters like power density and base temperature. In terms of the chosen base temperature and power density ranges it is possible to define two threshold values for each investigated tungsten grade valid for 100 pulses. On the one hand the **damage threshold** depends on the power density of the thermal shock events. A material exposed to a power density below this threshold shows no visible damages or surface modifications. On the other hand the **cracking threshold** and its location depends on the base temperature of the loaded material and divides the region above the damage threshold in two parts. Below the cracking threshold the loaded surfaces show crack networks or at least the formation of small cracks. Above the cracking threshold there are no cracks or crack networks observable anymore. An overview of the location and loading condition ranges for both thresholds based on the obtained results presented in subsection 3.4.1 is given in figure 3.50. Furthermore, the observed dependence of both thresholds on the loading conditions can be traced back to material parameters which are also mentioned in this figure.

All investigated tungsten grades have to withstand an increasing amount of thermal stresses with increasing power densities values. If these thermal stresses exceed a certain value, the damage threshold, the loaded area shows crack formation or at least roughening due to plastic deformation. The location of the damage threshold depends on the mechanical properties of the material such as yield and tensile strength. For tungsten grades with a very high yield/tensile strength such as WTa5 L the damage threshold is significantly higher than for the other tungsten grades. The opposite effect can be observed for transversal and recrystallised grain structures. For both grain structures the yield/tensile strength is significantly reduced which results in a decrease of the damage threshold.

One of the most important material parameters that influences the position of the cracking threshold of the investigated tungsten grades is the ductile/brittle behaviour

of the material. The ductility of tungsten strongly depends on the material temperature and is related to the DBTT. Especially at low temperatures tungsten behaves in general brittle which is confirmed for all investigated tungsten grades by the damage mapping (subsection 3.4.1). At RT all tungsten grades are unable to compensate the thermal stresses by plastic deformation and therefore show severe thermal shock crack formation that reduces these stresses. At elevated temperatures the tungsten grades become more ductile and are able to compensate the stresses by plastic deformation without exceeding the fracture strength. A very good example for this dependence gives the comparison of W-UHP L and pure W L. The cracking threshold of pure W L is located at a 100 °C lower base temperature than for W-UHP L and the stress-strain diagrams for these materials (subsection 3.1.2) show that the fracture strain of pure W L is much higher than for W-UHP L. But also the combination of a moderate or low plastic behaviour with a very high tensile strength as it is the case for WTa5 L leads to a low cracking threshold because the stresses do not exceed the tensile strength. Another example for the significant impact of the ductile/brittle behaviour on the location of the cracking threshold give the samples with transversal grain structure. The cracking threshold for all tungsten grades with transversal grain structure is located above at least 400 °C and they show a classic brittle behaviour in their stress-strain diagrams (figure 3.12).

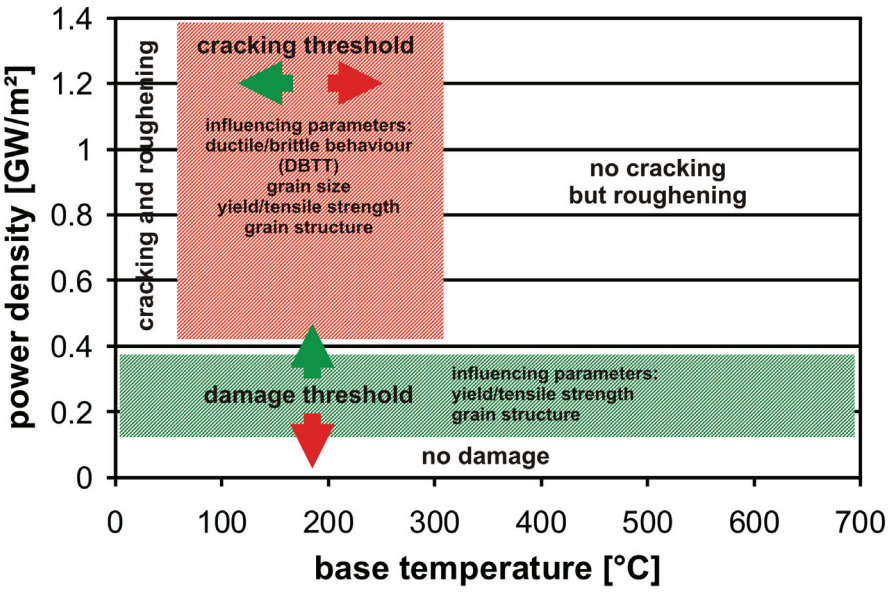

Figure 3.50: Threshold ranges (valid for the longitudinal grain structure and 100 pulses) and their influencing material parameters based on the obtained results presented in subsection 3.4.1. The arrows indicate the improvement (green) or degradation (red) direction for the respective threshold value.

Beside the deformation behaviour also the grain size has an influence on the cracking threshold. WVMW L and pure W L have nearly identical mechanical properties but the cracking threshold of WVMW L is much higher than for pure W L. The significant difference in grain size of these tungsten grades is an explanation for this (subsection 3.1.1). In comparison to pure W, WVMW has very small grains. This increases the grain boundary density at the loaded surface significantly. These boundaries are very susceptible for crack initiation. Therefore the probability of crack formation is higher for smaller grain sizes (subsections 3.1.2). Another result supporting the observation that the influence of the grain size is, that no crack networks are formed on WVMW L at 100 °C and 200 °C, but small randomly distributed cracks. This is of course only valid for the investigated range of grain sizes. If the grain size becomes very small (nano grains) or large (single crystal) additional effects have to be taken into account.

A closer investigation of the induced thermal shock damages and surface modifications showed that the respective damage characteristics depend on the loading conditions as well as on material parameters. The observed surface modifications were identified as roughening due to plastic deformation of the loaded surfaces. Above the damage and cracking threshold all materials show roughening of the loaded surface which becomes more pronounced for higher power density and related thermal stresses as well as reduced yield strength for higher base temperatures. These surface modifications are reduced if the material has a high fracture strain (e.g. pure W L), a high yield strength (e.g. WTa5 L) and/or a small grain size (e.g. WVMW L). The influence of the first two material parameters is very obvious because fracture strain and yield strength are a measure of how strong a material can be plastically deformed before it cracks. However, the influence of the grain size represents a complex process. A possible explanation for a less pronounced surface roughness of materials with smaller grains is a combination of three effects: first, smaller grains result in a the finer distribution of lattice orientations and therefore varying mechanical properties on the loaded surface [79, 101], which lead to stronger variations of the surface modifications; second, a larger grain size causes a stronger thermal gradient within a single grain and therefore larger thermal stresses, especially in the material depth; third, grain boundaries are weak points in the material lattice structure due to accumulation of defects and therefore allow the grains to compensate a small amount of thermal stresses by expansion in these open volumes. Despite brittleness at low temperatures the cracked samples loaded below the cracking threshold show also plastic deformation induced roughening of surfaces between the cracks. Although tungsten should be brittle at low temperatures, the combination of reduced stresses due to crack formation with the elevated temperatures during the thermal shock event enables the material to compensate additional thermal stresses by plastic deformation.

These dependencies are also valid for the transversal and recrystallised grain structures. However, the roughening of the transversal samples is less pronounced than for

the longitudinal samples due to the higher crack density and the resulting lower thermal stresses in the remaining connected areas. The roughening of the recrystallised samples is more pronounced because of the low yield strength in combination with the much larger grain sizes observed for four of the five tungsten grades. Roughness values increase for higher pulse numbers independent of the tungsten grade due to the repeated plastic deformation of the material and the accumulation of lattice defects until the material fails.

Furthermore, the formation and characteristics of thermal shock crack networks depend on the loading conditions as well as on the material properties as shown in subsections 3.4.2 and 3.4.3. An overview of all influencing factors is given in figure 3.51. The investigation of crack parameters such as distance, width and depth for the longitudinal samples at RT show that all experience a more or less distinct increase with increasing power density. Crack distance or crack density (inverse crack distance) and crack width are also depending on each other. If the crack density decreases the crack width increases to maintain the same open volume after the relaxation of thermal stresses due to crack formation. The reason for this dependence between loading conditions and crack parameters is that for higher power densities also the thermal stresses and therefore the strain rates increase. This leads to an improvement of the materials tensile strength and fracture toughness which directly influences the crack parameters. Beside the influence of the loading conditions also the addition of alloying elements like tantalum has a strong influence, especially for WTa5. WTa5 has the highest tensile strength of all investigated tungsten grades but the smallest fracture strain. Due to that its crack densities are among the largest which is also accompanied by the large crack widths. A second important parameter that influences the crack depth is the thermal conductivity of the material. A lower thermal conductivity leads to a steeper temperature gradient at the loaded surface. The thermal stresses can not propagate so deep into the material during a thermal shock event which results in a smaller crack penetration depth. This dependence was observed for WTa1 and even more pronounced for WTa5.

Beside the loading conditions and the material properties also the microstructure has a strong influence on the crack formation, especially on the surface pattern and propagation into the material. The thermal shock crack pattern at the loaded surface is strongly influenced by the grain shape/orientation. While the crack networks for the longitudinal and recrystallised grain structures are arbitrary and very similar, the cracks of the transversal samples follow the grain orientations and are oriented parallel to each other with a few nearly perpendicular connecting cracks. There are also similarities of the crack propagation into the material for the longitudinal and recrystallised grain structures. Both show a perpendicular crack propagation into the material which stops and propagates parallel to the loaded surface. These perpendicular cracks are intergranular for smaller grains and also transgranular if the grain size increases. The

cracking parallel to the loaded surface involves the risk of overheating and enhanced erosion of whole surface parts. In contrast to that, there is no parallel crack formation for the transversal grain structure and all cracks propagate along the grain boundaries. There are also significant differences between the grain structures regarding crack parameters. For the transversal grain structure the crack density is much higher which results in a less distinct surface roughening. The recrystallised samples show a significant increase of crack width and depth as well as an increased risk of complete grain erosion, especially for the tungsten grades with small grains. Reasons for these differences are the degradation of the material's properties because of the loss of the texture strengthening effect for the transversal grain orientation and the reduction of UTS and yield strength as well as apparently reduced cohesion between the grain boundaries for the recrystallised samples.

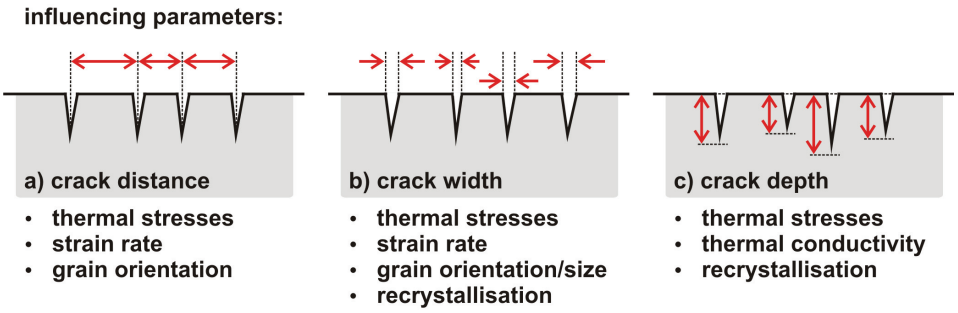

Figure 3.51: Overview of the crack parameters and their influencing parameters: a) crack distance; b) crack width; c) crack depth.

None of the crack parameters of the investigated tungsten grades shows a pulse number dependence, after the thermal crack network is initially formed. However, the initiation of thermal shock crack networks depends on the cycle numbers. For W-UHP L, WTa1 L and WTa5 L the thermal shock crack networks are formed after the first thermal shock event, while for pure W L and WVMW L thermal shock crack networks are formed between 10 and 100 thermal shock pulses, due to their high fracture strain. This enables the materials to withstand a single thermal shock without macroscopically visible damage formation and just roughening after 10 pulses. A combination of a high fracture strain with a small grain size with respect to the investigated tungsten grades leads to the formation of small discontinuous cracks (WVMW L and WTa1 L). These small cracks are supposed to act as initial state for the formation of a thermal shock crack network that will form on the loaded surface at higher pulse numbers. This was also observed in high pulse number experiments on tungsten and can be characterised as a material fatigue effect [100, 101].

The comparison of the thermal shock damages induced by laser and electron beam in subsection 3.4.4 proves the assumption based on FEM-simulations in section 3.3 that the volumetric loading in case of the electron beam (penetration depth for electrons in tungsten in the range of μm) instead of a more surface near loading valid for the laser beam (light decay length in the range of nm) has no significant influence on the damage behaviour and pattern at least at RT. Observed differences can be traced back to geometric effects due to the variations in size and shape of the exposed areas. Damage thresholds as well as the observed severe cracking and roughening of samples exposed above these tresholds are very similar and show just slight differences for the measured crack parameters. The differences in the arithmetic mean roughness are on the one hand also related to the geometric differences and the resulting variations of the crack parameters but also to high frequency scanning of the samples with the electron beam while a steady and homogeneous loading was applied by the laser.

Summarizing, it can be stated that the thermal shock response of tungsten is a very complex interaction of a lot of parameters comprising among others the loading conditions itself, the thermomechanical properties and the microstructure. Important connections and interactions could be identified, which give objections and suggestions for new material compositions and manufacturing processes. On the basis of the results presented in this chapter it is very difficult to decide on a ranking of the investigated tungsten grades one being better than the other. WTa5 L showed the best performance regarding the threshold values but show a very severe parallel crack formation, which has to be prevented in a device like ITER, because of the risk of surface erosion and melting. In contrast to that it behaves worst of all investigated tungsten grades for the transversal and recrystallised grain structure. A more general result of this chapter is that recrystallisation of the material, which will take place during steady state loading, if only affecting a small surface area will increase the erosion of complete grains significantly and could therefore cause an intolerable contamination of the plasma. But the most important result is that under these loading conditions, i.e. very high power density (up to 1.27 GWm^{-2}) for low pulse numbers (100 pulses), all investigated tungsten grades show severe damage formation, namely roughening and cracking. Even for WTa5 the damage threshold is not high enough to prevent this damage formation. Based on this it can be stated that for cycle numbers of 10^6 or more, as expected for ITER, tungsten as a PFM will fail under these high thermal loads. Of course the threshold value can be improved, but only in a limited range which will not cover the expected power densities. Furthermore, the exposure to particle fluxes such as hydrogen, helium and neutrons has to be taken into account which will lead to an additional material degradation. The solution of this problem could be an improvement of material properties in combination with plasma control. Mitigation of ELMs to lower power densities and a prevention of off-normal events like VDEs and plasma disruptions or at least a limitation to very small numbers would be a very promising approach.

4 Influence of hydrogen on the thermal shock behaviour of tungsten

PFMs in future fusion devices, such as ITER and DEMO, will not only have to withstand high heat fluxes (subsection 1.3.1), but also high particle fluxes consisting of hydrogen, helium and neutrons (subsection 1.3.2). The results presented in chapter 3 and previous studies on different materials and simulation methods have shown that transient thermal loads induce severe damages such as surface modifications (roughening), thermal shock crack networks, enhanced erosion and melting of the loaded surface [54, 55]. In this chapter tungsten was exposed to high flux hydrogen plasma and electron beam successively to achieve more realistic loading conditions and to study the influence of hydrogen on the thermal shock behaviour.

4.1 Tungsten grade

The investigated material is also an industrially available tungsten grade with a purity of 99.97 wt% (metallic purity excluding molybdenum 100 μg/g) manufactured by the Plansee AG, Austria. With regards to the chemical composition it is very similar to the pure W presented in chapter 3. The major difference is the manufacturing process and the resulting microstructure of the material. While the manufacturing process including the sintering is the same for both materials (subsection 3.1.1), the thermo mechanical treatment and densification afterwards are completely different. The investigated tungsten is a rod material hammered in radial direction with a diameter of 12 mm as schematically shown in figures 4.1a and b. Afterwards the material was annealed at 1000 °C for 1 h to relieve the mechanical stresses induced during hammering.

Due to this manufacturing processes the grains of the material have a strongly elongated needle like shape perpendicular to the deformation direction as shown in figure 4.1b. The grain structure was investigated by metallographic means (section 2.4) to characterise the inhomogeneous structure and to determine the average grain size. LM images of the grain structure are shown in figures 4.1c and d. The resulting average grain dimensions are 23 μm in diameter and 56 μm in length (average grain area: top view $\approx$ 420 μm^2; cross section $\approx$ 817 μm^2). This much smaller grain size than for the pure W investigated in chapter 3 is a major reason why this tungsten grade was used for

the experiments. Because of the heavily deformed grain structure, the grain boundary density is significantly increased for the top view, which has a strong influence on the hydrogen retention and transportation in tungsten [102].

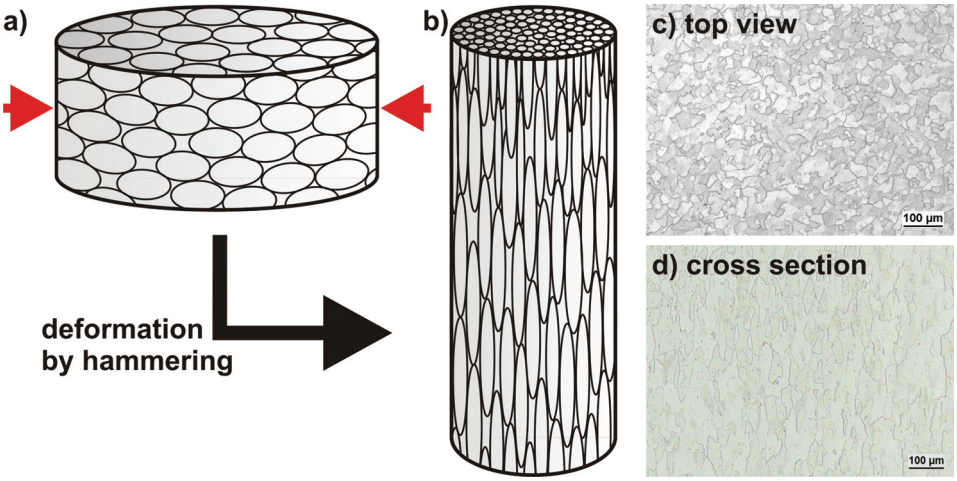

Figure 4.1: Schematic overview of the manufacturing process and the resulting grain structure of the material before (a) and after (b) the thermomechanical treatment. LM images of the grain structure in top view (c) and cross section (d).

4.2 Experimental conditions

The experiments were carried out in collaboration between DIFFER and FZ-Jülich. Tungsten targets were exposed to hydrogen-plasma in the linear plasma devices Pilot-PSI (subsection 2.3.2) and MARION (subsection 2.3.3). The cyclic thermal shock tests were performed with the electron beam facility JUDITH 1 (subsection 2.3.1). An overview of the samples mounted in the respective devices is given in figure 4.2.

Small disc shaped samples were cut form the received tungsten rod (figure 4.1b). The samples that were used in all three devices have a diameter of 12 mm and a height of 5 mm. This sample geometry guarantees that the grains are oriented perpendicular to the loaded surface to ensure the maximum retention of hydrogen during the exposure. Before the samples were mounted in any of the test facilities, the front side of each sample was polished to a mirror finish as described in 3.2 to obtain a predefined reference surface structure. The stresses induced in the material due to the final polishing are negligible in comparison to the stresses resulting from the manufacturing process. After the sample preparation they were exposed to hydrogen plasma and/or the electron beam. For a better overview which loading scenario was applied to a particular sample and in which sequence, the target name is divided into two parts. The first part

is the sample label (two to four letters or numbers). It shows the conditions the target was exposed to, while the second part (one or two letters after the blank) indicates in which sequence the exposure was done, e.g. PE means that the sample first was exposed to hydrogen plasma (P) and subsequently to the electron beam (E).

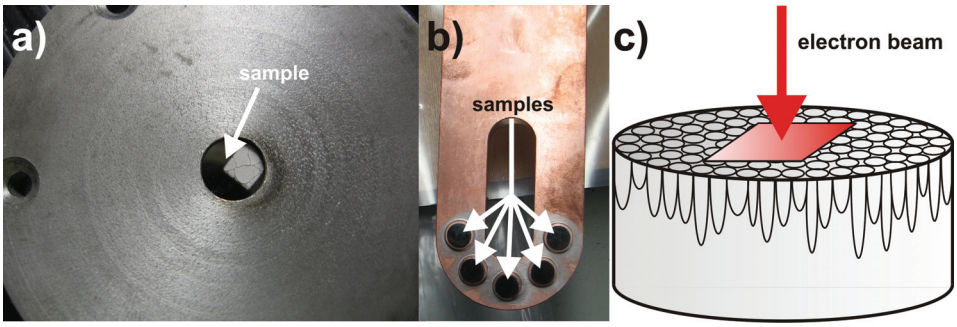

Figure 4.2: Tungsten samples during exposure: a) sample mounted in Pilot-PSI; b) samples brazed on copper heat sink for the exposure in MARION; c) schematic view of the tungsten sample exposed in JUDITH 1 with grains oriented perpendicular to the loaded surface (red square).

Nine samples were exposed to high flux hydrogen-plasma in the linear plasma device Pilot-PSI. All targets were mechanically clamped to an actively cooled copper heat sink and electrically floating for the plasma exposure. Therefore it can be assumed that the flux entering the sheath is equal to the flux at the target surface. During the exposure the plasma conditions were recorded by Thomson scattering at ~21 mm in front of the target. The surface temperature was measured by a multi-wavelength pyrometer in the centre of the target with a spot size of about 2 mm. The different exposure conditions are shown in table 4.1. As already mentioned in subsection 2.3.2, the electron density n_e and temperature T_e, which corresponds to T_i in Pilot-PSI, as well as the surface temperature is not constant over the plasma beam width. The plasma beam has a Gaussian profile with a FWHM of approximately 10 mm. To minimise this effect the exposed area of the tungsten targets is limited to a circular area with a diameter of 8 mm (figure 4.2a) which is smaller than the FWHM of the n_e and T_e profiles. Sequential plasma discharges with identical plasma parameters are used to accumulate high fluence (flux integrated over time). The plasma provides all the target heating power and reaches steady state conditions within $\leq$0.5 s after it is turned on. The cool down of the sample after the plasma exposure is in the same time range. Due to this rapid heating and cooling all diffusion and release processes are frozen since they depend exponentially on temperature. The distribution of hydrogen in the tungsten samples is identical to longer and continuous shots. However, it has to be taken into account that during the shorter, sequential shots, the tungsten targets undergo thermal cycles from the plasma heating.

Table 4.1: Exposure conditions in Pilot-PSI recorded by Thomson scattering at ∼21 mm and a multi-wavelength pyrometer.

Target	$n_{e,centre}$ [m^{-3}]	$T_{e,centre}$ [eV]	$t_{exposure}$	$T_{surf,centre}$ [°C]	flux [D^+/m^2s]
184A EP	2.1×10^{20}	1.1	30 s	500±50	2.4×10^{23}
184E PE	1.0×10^{20}	1.0	30 s	500±50	2.4×10^{23}
184G PE	6.0×10^{20}	1.6	10 s	700±50	1.4×10^{24}
184F EP	8.5×10^{20}	1.9	4×20 s	800±50	4.2×10^{23}
184F PE	0.85×10^{20}	0.95	5×6 s	500±50	2.2×10^{23}
184H PE	5.2×10^{20}	1.5	5×10 s	700±50	7.3×10^{23}
184J P	7.5×10^{20}	1.75	6 s	700±50	2.5×10^{24}
F2 PE	1.1×10^{20}	0.9	5×6 s	150±50	2.2×10^{23}
F8 PE	1.1×10^{20}	1.2	30 s	150±50	2.2×10^{23}

Beside the plasma exposure in Pilot-PSI additional samples were loaded in the ion beam test facility MARION. The major difference is that the ion particle energies are much higher, but the particle densities and therefore the fluence is much smaller in comparison to Pilot-PSI. First of all, a new actively cooled sample holder had to be designed and constructed (figure 4.2b). With this holder it is possible to expose five samples simultaneously. Because of the decreasing power densities in radial direction of the plasma beam, the samples have to be arranged circular to ensure that they are exposed to the same plasma conditions. The sample holder is described in more detail in appendix A. All targets were exposed to hydrogen-plasma with a particle energy of about 20 keV and a flux of ca. $2{\cdot}10^{21}$ D^+/m^2s, which results in a power density of around 6 MWm^{-2} and base temperature of approximately 500 °C. To achieve a comparable fluence to Pilot-PSI, the samples were exposed to 110 pulses with a duration of 20 s and an average single beam fluence of ca. $4{\cdot}10^{22}$ m^{-2}. This results in a total fluence of ca. $4.2{\cdot}10^{24}$ m^{-2}.

The cyclic thermal shock tests were carried out at the electron beam facility JUDITH 1. In contrast to the ELM like thermal shock events simulated in chapter 3.1, the intention here is to simulate disruption like events with much longer pulse duration and a very severe crack formation. All samples were grounded via a 100 Ω resistor and the current through the samples was measured. The electrons hit the samples with an energy of 120 keV. Because of this high energy the electrons penetrate up to 7 μm deep into the W sample and cause (within this thin layer) volumetric heating instead of pure surface heating. To achieve a homogeneous loading of the W target the exposed area was small (4×4 mm^2) and scanned with high frequencies (47 kHz in x-direction and 43 kHz in y-direction) using a focused electron beam (diameter of 1 mm). To ensure that crack networks are generated, all targets were exposed at room temperature (RT) to electron currents of 70 mA and 120 mA which corresponds to average incident power densities of 525 MWm^{-2} and 900 MWm^{-2}, respectively. Due to an electron absorption

coefficient of 0.46 for tungsten (obtained by current measurements and neglecting the emission of secondary electrons, see subsection 2.3.1), this leads to absorbed power densities of 242 MWm^{-2} and 414 MWm^{-2}. The simulation of disruption like events made it necessary to set the pulse length to 5 ms resulting in deposited energy densities of 1.21 MJm^{-2} and 2.1 MJm^{-2} and a temperature rise of $\Delta T \sim 1000$ K and 1700 K, respectively, for a single disruption. In contrast to the test in Pilot-PSI and MARION, the samples were not actively cooled. For that reason the inter pulse time was set to 3 s to prevent the samples from overheating. Each sample was exposed to 100 cycles.

4.3 Results and discussion

After the exposure in Pilot-PSI, MARION and JUDITH 1 all samples were investigated by LM, SEM and laser profilometry. Therefore the same accuracy and definitions were used as described in section 2.4 and subsection 3.4.

An overview of the induced surface modifications and damages after the exposure to hydrogen plasma and electron beam is given in figure 4.3. Areas that show no surface modification after loading appear black (still polished) and lighter areas have changed their surface morphology and reflect more light. All plasma loaded samples in this figure were exposed in Pilot-PSI. The plasma and electron beam loaded areas are indicated by the red circle and the blue square, respectively. Targets made from the same materials and exposed to the same plasma conditions were investigated by SEM at high magnification to ensure that there were no visible surface modifications like roughening or blister formation after the exposure to hydrogen plasma either in Pilot-PSI or MARION. Samples 184C E and 184D E (figures 4.3a and f) were additionally exposed to a single thermal shock pulse next to the area exposed to 100 pulses (blue square) which has no influence on the results presented below.

The investigation of the tungsten targets after loading shows that there are significant differences in the surface morphology and damage structure in dependence on the particular load and the sequence of the loading. Generally, it can be stated that the induced damages such as crack formation and roughening become more severe for high thermal shock power densities as it was already shown in chapter 3. Furthermore thermal shock crack networks either with or without subsequent exposure to hydrogen-plasma lead to crack formation that is limited to the thermal shock loaded area. The comparison of the thermal shock crack networks shown in figure 4.3a, b, f and g with the in chapter 3 presented results shows that there are no significant differences regarding the size of the cracked area or pattern. Therefore it can be deduced that the exposure to the chosen hydrogen-plasma conditions has no influence on already existing crack networks and does not cause any other surface modification. This is confirmed by sample 184J P (figure 4.3e), which was exposed to hydrogen-plasma only and shows no visible damages or surface modifications. The lighter areas in figure 4.3a and e are

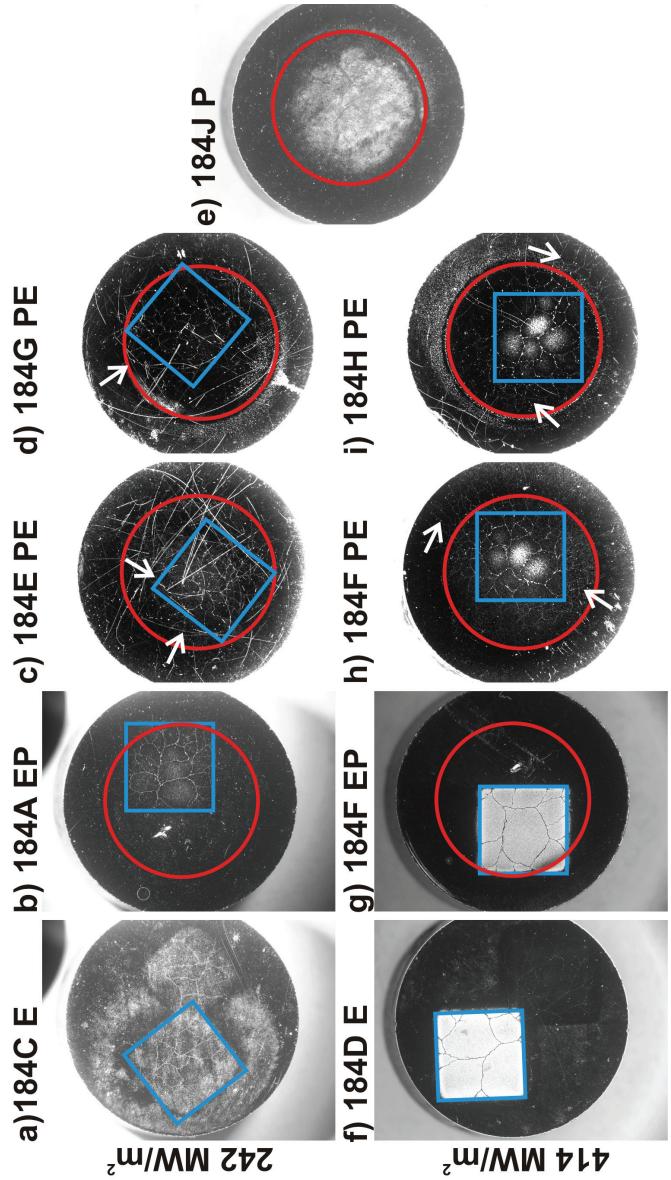

Figure 4.3: LM images of the loaded tungsten surfaces after exposure to hydrogen.plasma (Pilot-PSI) and/or electron beam (power density a – d: 242 MWm^{-2}; f – i: 414 MWm^{-2}). The plasma and electron beam loaded areas are indicated by the red circle (d = 8 mm) and the blue square (4 × 4 mm^2), respectively. Cracks outside the electron beam and plasma loaded areas are highlighted by the white arrows. a/f) samples 184C E/184D E exposed to electron beam only; b/g) samples 184A EP/184F EP first exposed to electron beam and afterwards to hydrogen plasma; c/d) and h/i) samples 184E PE/184G PE and 184F PE/184H PE first exposed to hydrogen plasma afterwards to electron beam; e) sample 184J P only exposed to hydrogen plasma.

not a result of the hydrogen or electron beam loading. It is a small oxide layer (determined by EDX) which was probably formed due to contamination after the exposure. In contrast to that the pre-exposure with hydrogen-plasma has a significant influence on the thermal shock response of the material (figures 4.3c, d, h and i). The thermal shock crack networks are much finer and not anymore limited to the thermal shock loaded area itself but also cover a large part of the only hydrogen-loaded area (white arrows). Some cracks even extend over the complete unloaded area at the edge of the sample.

In order to identify plasma parameters which influence this different thermal shock response of tungsten, additional samples were pre-exposed in Pilot-PSI and only some parameters were modified (see table 4.1), while the electron beam conditions were kept constant at an absorbed power density of 414 MWm^{-2}.

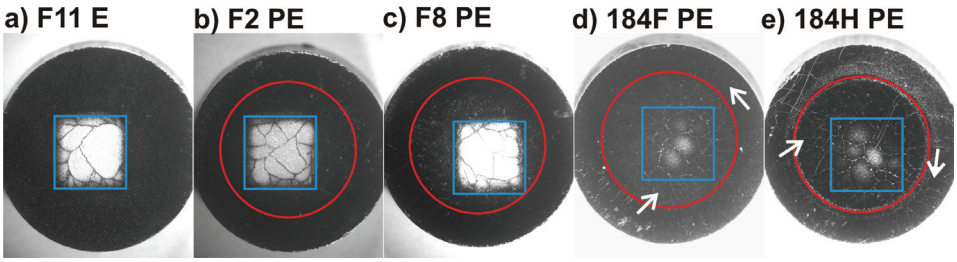

Figure 4.4: LM images of the W targets after the exposure to hydrogen-plasma and/or electron beam (power density: 414 MWm^{-2}). The loaded areas are indicated by a red circle (d = 8 mm) for plasma exposure and a blue square (4×4 mm^2) for the electron beam loading. a) sample F11 E exposed to electron beam only, b) sample F2 PE exposed to hydrogen plasma (pulsed, at 150 °C) and electron beam, c) sample F8 PE exposed to hydrogen plasma (continuous, at 150 °C) and electron beam, d) sample 184F PE exposed to hydrogen plasma (pulsed, at 500 °C) and electron beam, e) sample 184H PE exposed to hydrogen plasma (pulsed, at 700 °C) and electron beam.

Samples F2 PE and F8 PE (figures 4.4b and 4.4c), which were preloaded with hydrogen-plasma at 150 °C, show no visible differences in their cracking pattern to the only electron beam loaded sample F11 E (figure 4.4a) which was exposed at the same time in JIDITH 1. Furthermore, the pulsed (F2 PE) and continuous (F8 PE) exposure to hydrogen-plasma at this temperature seems to have no significant influence on the damage behaviour. In contrast to this similar appearance of the induced damages on samples F11 E, F2 PE and F8 PE, the samples 184F PE and 184H PE (figures 4.4d and e) show significant differences. Both samples were preloaded with hydrogen-plasma but at higher surface temperatures during the exposure (184H PE at 500 °C and 184H PE at 700 °C). They show a much finer and less pronounced thermal shock crack network,

which is not limited to the electron beam loaded area anymore. Some thermal shock cracks propagate through the only hydrogen-plasma and even unloaded area (white arrows in figures 4.4d and e).

The LM images presented in figure 4.3 and 4.4 show that the induced surface modifications are more pronounced for higher power densities during the thermal shock events. Therefore the characterisation of the surface morphology by laser profilometry presented in figure 4.5a and b focusses on samples exposed to these loading conditions. Both figures show one line scan of each sample while the same unloaded and polished reference sample was used.

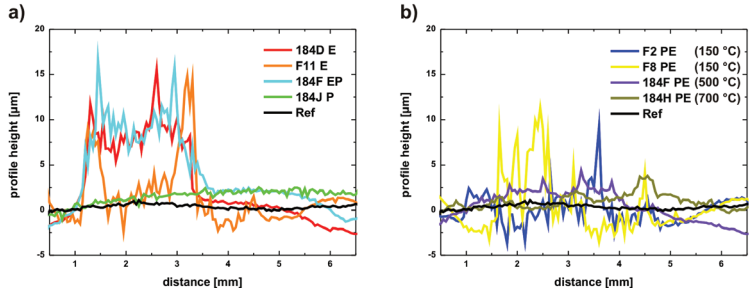

Figure 4.5: Laser profilometry line scans of the samples exposed to hydrogen plasma (Pilot-PSI) and thermal shock events (power density: 414 MWm^{-2}) with an accuracy of 20 points/mm. The reference (Ref) is an unloaded, polished sample in both diagrams. The roughening of the samples becomes less distinct for hydrogen-plasma pre-exposed samples and increasing surface temperature during the plasma exposure (values in brackets).

The line scans show that the surface modification is related to surface roughening with different characteristic depending on the loading conditions. The comparison of the only plasma exposed sample 184J P with the unloaded reference confirms the optical impression that the hydrogen-plasma does not induce any surface modifications on the loaded surface. In contrast to that, the roughening of the first electron beam exposed specimen or of a just electron beam loaded sample is severe. The surface profiles of 184D E, F11 E and 184F EP shown in figure 4.5a are very similar with maximum values between 15 μm and 17 μm. Additionally, the roughening is limited to a width of approximately 4 mm which corresponds to the electron beam loaded area of 4×4 mm^2. The surface roughening of the samples pre-exposed with hydrogen-plasma (figure 4.5b) is less pronounced and not so strictly limited to a certain width, but also shows a surface temperature dependence. At lower surface temperature of 150 °C (F2 PE and F8 PE) the roughening is more distinct with maximum values around 10 μm than for temperatures of 500 °C and above (184F PE and 184H PE) were the maximum profile height is ca. 3 μm.

An explanation for the different surface modifications can be found in the accompanying effect of an increase of the cracked surface area and changes of the crack parameters. In chapter 3 it was found that the surface modifications are a result of plastic deformations of the tungsten surface due to compressive and tensile stresses induced by cyclic thermal shock loading. These stresses are reduced by crack networks which are formed during the first thermal shock event under these loading conditions as it can be seen in figure 4.3a and f. A higher crack density and a cracking of the unloaded surrounding material act as a natural castellation. This leads to a reduction of thermal stresses and therefore a reduced plastic deformation and less pronounced surface roughness.

SEM images at very high magnification of the roughened surface around the thermal shock cracks are shown in figure 4.6 and prove the differences and their dependence on the loading sequence as well as of the surface temperature. Samples which were only exposed to the electron beam (figure 4.6a), pre-exposed to the electron beam (figure 4.6b) or pre-exposed to hydrogen-plasma at low temperatures (figure 4.6c) show severe surface roughening in the non-cracked areas, while the samples pre-exposed to hydrogen-plasma at high temperatures (figure 4.6d and e) show only slight surface modifications. The samples only exposed to hydrogen-plasma show no damages or surface modifications at all.

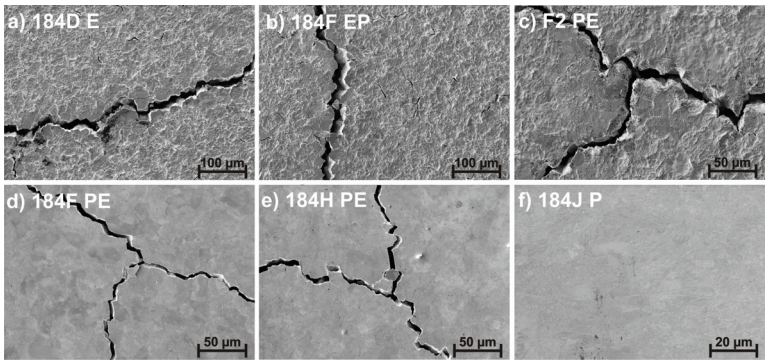

Figure 4.6: SEM images of the loaded surfaces after the exposure to hydrogen-plasma and/or thermal shock events. The different thermal shock responses in dependence on the loading conditions are clearly visible.

Beside the characterisation of the surface modifications, these and other SEM images as well as LM pictures of the top surface and cross sections were used to determine the crack parameters such as distance, width and depth as defined in section 3.4. An overview of the determined maximum and average crack parameter values is given in table 4.2 for an absorbed thermal shock power density of 242 MWm^{-2} and in table 4.3 for an absorbed thermal shock power density of 414 MWm^{-2}.

Table 4.2: Maximum and average values for crack distance, width and depth of tungsten exposed in JUDITH 1 (power density: 242 MWm^{-2}) and Pilot-PSI successively.

sample name	184C E	184A EP	184E PE	184G PE
$T_{surf,centre}$ [°C]	-	500	500	700
max. crack distance [μm]	2065	1871	1486	1482
avg. crack distance [μm]	598	667	568	563
max. crack width [μm]	5	10	4	4
avg. crack width [μm]	3	4	3	3
max. crack depth [μm]	480	751	573	555
avg. crack depth [μm]	379	486	340	267

Table 4.3: Maximum and average values for crack distance, width and depth of tungsten exposed in JUDITH 1 (power density: 414 MWm^{-2}) and Pilot-PSI successively, except F17 PE which was exposed in MARION.

sample name	184D E	F11 E	Ref E	184F EP	F2 PE	F8 PE	184F PE	184H PE	F17 PE
$T_{surf,centre}$ [°C]	-	-	-	800	150	150	500	700	500
max. crack distance [μm]	3140	3101	3140	2961	2110	2422	1890	1989	2444
avg. crack distance [μm]	1217	873	1039	1005	629	667	562	686	653
max. crack width [μm]	30	63	63	31	40	58	7	8	60
avg. crack width [μm]	20	32	27	25	16	19	5	6	24
max. crack depth [μm]	1240	1394	1394	1201	1038	1236	629	524	1091
avg. crack depth [μm]	817	1107	959	981	847	726	350	303	844

For the lower power density of 242 MWm^{-2} it can be stated that there are no significant differences in the crack parameters. There are only slight differences in crack distances which leads to a higher crack density (reciprocal crack distance) for the hydrogen pre-exposed samples. But this increase of the crack density is not accompanied by an increasing crack width as it was found in chapter 3. This suggests that this development is dominated by statistical deviations due to the poor statistics (section 3.4). A more pronounced development is observed for the crack depth, which decreases significantly for the intensive hydrogen pre-exposure (184G PE).

More pronounced changes and dependences on the loading conditions can be observed for the higher power density of 414 MWm^{-2}. The comparison of the electron beam pre-loaded sample (184F EP) with the only electron beam exposed reference (Ref E), which is a combination of the reference samples 184D E and F11 E, shows that there is no difference in the crack parameters as it was also valid for the lower power density. But the additional comparison of the hydrogen pre-loaded samples shows that all crack parameters are slightly or even significantly smaller than for the only or electron beam pre-loaded samples. From this, it follows that the pre-loading with hydrogen-plasma has a general effect on the damage behaviour of tungsten. A closer comparison among the preloaded samples shows that this effect is influenced by the plasma parameters. Samples F2 PE and F8 PE were preloaded at the same surface temperature of 150 °C but F2 PE was exposed to a pulsed and F8 PE to continuous plasma beam with the same total exposure time of 30 s (see table 4.1). The crack parameters of these samples are similar and therefore the pulsed plasma loading has no influence on the thermal shock behaviour at least for these low cycle numbers. In contrast to that the samples preloaded at higher temperatures (184F PE at 500 °C, 184H PE at 700 °C; see table 4.1) show a significantly different material response. Especially the values for crack width and depth are half the size or less than for the preloaded specimens at lower surface temperatures.

Beside the investigation of samples exposed to hydrogen-plasma in Pilot-PSI there have also been some samples that were hydrogen pre-loaded in MARION and afterwards exposed to thermal shock events of 414 MWm^{-2} in JUDITH 1. Figure 4.7 shows an overview of the whole loaded surface of such a sample (a) and a SEM image at high magnification of a thermal shock crack (b). The determined crack parameters are listed in the last column of table 4.3 and show a similar decrease as it was observed for the hydrogen pre-exposed samples in Pilot-PSI. But the crack parameters (see table 4.3) correspond more to the pre-loaded samples with lower surface temperature, although a surface temperature of 500 °C was measured during the plasma exposure. Furthermore the thermal shock crack network is limited to the electron beam exposed area and does not propagate in the only hydrogen-plasma exposed region, which is also in contrast to the thermal shock response of the hydrogen pre-loaded samples in Pilot-PSI at the same temperatures.

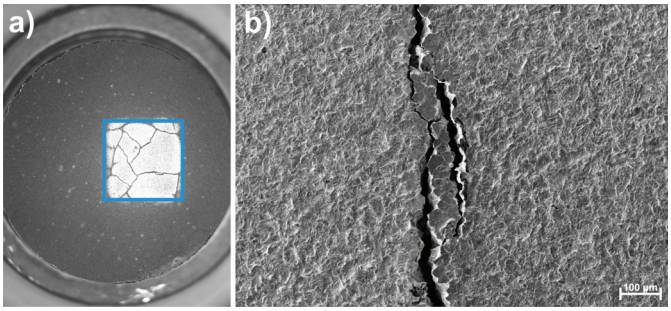

Figure 4.7: LM (a) and SEM (b) images of sample F17 PE which was preloaded with hydrogen-plasma in MARION and afterwards exposed to 414 MWm^{-2} thermal shocks in JUDITH 1. The electron beam exposed area is indicated by a blue square (4×4 mm^2). In contrast to the loading in Pilot-PSI, the whole surface was exposed to hydrogen-plasma.

All presented results show that the successive exposure of tungsten with hydrogen-plasma and electron beam has a strong influence on its thermal shock response. One reason for the different thermal shock behaviour of tungsten that was preloaded with hydrogen plasma might be the diffusion of hydrogen into the tungsten lattice and the formation of hydrogen molecules. Hydrogen and hydrogen molecules are trapped by lattice defects like vacancies, dislocations, grain boundaries etc. and cause a distortion of the lattice structure that generates stresses in the material. Due to these additional stresses the critical stresses for crack formation and propagation are lowered. This effect is called hydrogen embrittlement [103, 104]. Despite the amount of hydrogen retention in the material being typically low for these plasma exposure conditions [105] another explanation could be, that the high rate of hydrogen implantation causes the tungsten to be in a state of super-saturation during plasma exposure and this also leads to stresses in the material lattice [46]. These super-saturation stresses can result in the formation of vacancies, dislocations and vacancy clusters, which can then be "frozen" into the lattice due to the rapid cooling once the plasma is removed. This may also contribute to the embrittlement and enhanced crack formation. Both effects reduce the resistance against crack formation and therefore have a direct influence on the thermal shock response of the materials. The degradation of the mechanical properties as well as the fracture toughness leads to crack propagation in the only hydrogen-plasma exposed and even the unexposed surface areas.

The surface temperature has also a strong influence on hydrogen retention and diffusion properties of tungsten [106, 107]. Even for the very low hydrogen retention under these loading conditions (table 4.1) there is a temperature dependence of the retention [71, 105]. According to this it is likely that the changes in the thermal shock behaviour of the material after the pre-exposure with hydrogen-plasma also show a

surface temperature dependence as the presented results suggest. Both mechanisms, embrittlement and super-saturation stresses, are based on temperature dependent processes like diffusion or implantation of hydrogen, mobility of lattice defects and hydrogen trapping mechanisms in tungsten. The hydrogen retention is enhanced for high fluences when the irradiation temperature is high and hydrogen can diffuse deeper into the material. At temperatures above 300 °C the ion-induced and natural defects in tungsten, which act as trap sites for hydrogen, become mobile. They can diffuse deeper into the material and/or agglomerate to vacancy clusters. When these vacancy clusters are formed in tungsten hydrogen can also be retained by chemisorption [46, 103, 108]. The combination of a higher mobility of hydrogen and lattice defects with an agglomeration of vacancies and a new absorption mechanism could be responsible for the observed temperature differences in the thermal shock response of hydrogen preloaded tungsten. Beside the influence of the surface temperature during the hydrogen preloading also the fluence during the exposure has an influence on the thermal shock response. It was much smaller for a single shot in MARION than in Pilot-PSI. Therefore hydrogen can diffuse deeper into the material during the inter shot time and this seems to compensate the super-saturation effect at elevated temperatures.

The embrittlement and/or the super-saturation stresses reduce the resistance of the material against crack formation and therefore have a direct influence on the thermal shock behaviour and the crack propagation on the thermal shock loaded, just hydrogen-plasma loaded and unloaded material's surface. The degradation of the mechanical properties even leads to the formation of cracks outside the loaded area, which indicates a significant reduction of the fracture toughness of the hydrogen-affected surface-near volume. The cracking at lower stresses leads to a "natural" castellation of the material. This results in a smaller crack width and depth compared to the initial material without hydrogen-induced embrittlement.

4.4 Summary and conclusion

The obtained results show that the combined loading of tungsten with hydrogen-plasma and electrons has a significant influence on its thermal shock response. However, the order of the loading conditions seems to be the most important parameter. The exposure of a thermal shock crack network, induced by an electron beam, to hydrogen-plasma has no measurable effect on the crack pattern and parameters. In contrast to that the pre-exposure of tungsten to hydrogen-plasma results in case of a following cyclic thermal shock loading of the material for all investigated conditions in a significant change of the thermal shock response. All hydrogen preloaded samples show higher crack densities, lower crack width and smaller crack penetration depth in the cyclic thermal shock exposed area. How distinct these modifications are depends on the plasma parameters during the exposure such as surface temperature, fluence and number of pulses. Beside the modification of crack parameters an additional effect was observed

at surface temperatures above 500 °C during the plasma exposure. The thermal shock cracks are not limited to the electron beam exposed area anymore but propagate also through the only hydrogen-plasma exposed area and even the unloaded material at the sample edges. This "natural" castellation of the material leads to a reduction of thermal stresses and therefore to a less pronounced plastic deformation. But this extensive crack propagation seems to be suppressed or shifted to higher surface temperatures if the fluence per plasma pulse is reduced.

Reasons for these observed effects are assumed to be hydrogen embrittlement of tungsten and/or super-saturation of stresses in the crystal lattice. Both effects are based on temperature dependent mechanisms such as diffusion, mobility of lattice defects and hydrogen trapping in dislocations, vacancies or defect agglomerations. Furthermore the mobility and agglomeration of vacancies are temperature activated processes which are initiated at temperatures above 300 °C and therefore could play an important role for the explanation of this effect.

The observed changes in cracking pattern and crack parameters, especially the higher crack density and the finer crack structure of tungsten can be an advantage and disadvantage for an application as PFM in future fusion devices. An improved compensation of thermal stresses during a thermal shock event due to "natural" castellation of the materials surface leads to a reduced plastic deformation. Surface modifications due to thermal fatigue would be reduced and the life time of the PFC could increase. But the increase of the cracked area and the higher crack density could lead to severe problems for the operation of ITER and DEMO, especially for very high pulse numbers of more than 10^6. The compressive and tensile stresses induced during a thermal shock event causes enhanced erosion of surface material due to the cyclic closing and opening of crack edges [100]. Additionally, the effective thermal conductivity of surface parts is reduced, which results in recrystallisation or even melting of the material. This will lead to an accelerated degradation of the PFC as well as involves the danger of enhanced plasma contamination with tungsten which causes a collapse of the fusion reaction in the worst case [34, 39].

Although the PFM in fusion devices will not be exposed to hydrogen-plasma and thermal shock events successively, these tests are application oriented especially for the beginning of ITER operation. The first plasma in ITER will be hydrogen-plasma in L-mode during which no superimposed thermal shock events are expected. During this operation mode the PFMs are "pre-loaded" with hydrogen before ITER will run in H-mode with thermal shock events. Furthermore the results show that induced thermal shock damages such as crack formation and surface modification are strongly influenced by particle fluxes and its parameters. It has to be kept in mind that PFCs are not only exposed to hydrogen but also to helium and neutron fluxes which will also have severe influence on the thermal shock response of tungsten.

5 Overall conclusion and outlook

The focus of this work is to investigate the thermal shock response of tungsten grades under severe loading conditions in terms of power densities and preconditions such as base temperature and hydrogen loading. For that reason this work is divided in two parts. First, the comparison of five different tungsten grades at short pulse numbers but very high power densities (chapter 3) and second, the effects of successive hydrogen and electron beam exposure on the thermal shock response of tungsten were investigated. The results of each individual part were already discussed at the end of the corresponding chapter (cf. section 3.5 and 4.4). In this chapter both parts will be combined to give a more general overview of the expected material modifications and damages in future fusion devices such as ITER and DEMO.

The exposure of tungsten exclusively to ITER relevant ELM like thermal shock events with very high power densities shows that very severe surface modifications and damages are induced in the loaded material even after a limited number of 100 pulses. Based on the obtained results and the surface characterisation after exposure it was possible to define damage and cracking threshold values: at a power density of 0.16 GWm^{-2} and below none of the tested materials showed any visible surface modification or damage formation. Additionally, none of the investigated tungsten grades showed crack formation if the material was heated to a base temperature of above 400 °C before and during the exposure to thermal shock events. At the first glance these values sound quite promising, but these threshold values are only valid for 100 pulses. Further loading at values above the damage threshold will lead to an accumulation of plastic deformation which will become more severe for higher power densities and in the end lead to a failure of the material and in the worst case of the whole PFC.

Beside the thermal shock tests also the determination of the thermomechanical properties as well as the characterisation of the microstructure of all investigated tungsten grades were implemented. Material parameters could be identified which influence the location of threshold values as well as the pattern of induced thermal shock damages (details can be found in section 3.5). These results implement concepts to improve the thermal shock performance of tungsten and its alloys to withstand higher power densities without any severe damage formation, but the expected transient heat loads of 1 GWm^{-2} and above in ITER will still induce non-tolerable material degradation.

Additionally to these pure thermal loading conditions tungsten was exposed to high flux hydrogen-plasma and transient thermal shock events successively. It was shown that pre-exposure of tungsten with hydrogen has a significant influence on its thermal shock response. Thermal shock cracks propagate even in completely unexposed areas and crack parameters such as distance, width and depth decrease. These changes can be an advantage or disadvantage. A "natural" castellation of the material because of the extended cracked region reduces thermal stresses and leads to reduced plastic deformation. On the other hand this can also lead to an enhanced erosion at higher pulse numbers, especially at the crack edges. Anyhow, the pre-exposure of tungsten to hydrogen induces additional damages in the crystal lattice which degrade the material properties such as crack resistance significantly. This will lead to decreasing damage and increasing cracking thresholds in terms of power density and base temperature values. These effects will become more severe, if tungsten is not only exposed to hydrogen but also to helium and neutron fluxes as it will be the case in ITER and even especially in DEMO.

The results presented in this work show that problems of tungsten as a PFM under these severe loading conditions as they are expected today for ITER, consisting of steady state heat loads up to 20 MWm^{-2}, transient events with power densities of more that 1 GWm^{-2} and high hydrogen, helium and neutron fluxes, can not be solved from the materials science side alone. Much more important and promising is a close collaboration with plasma physicists as well as component designers and manufactures, to improve the PFC design and properties to enhance the thermal shock response even under high particle fluxes and to mitigate the power densities of transient ELM like events. Additionally the occurrence of off-normal events like disruptions and VDEs has to be prevented or at least mitigated and limited to a small number of events.

A Appendix: Hydrogen implantation in MARION

As mentioned in section 4.2 a new actively cooled sample holder had to be designed and manufactured for the exposure of tungsten samples to hydrogen plasma in the ion beam test facility MARION (subsection 2.3.3). Due to the shape of the plasma beam in MARION the samples are arranged in a circular manner to ensure that they are exposed to the same plasma conditions. A picture of the complete sample holder is shown in figure 1.1.

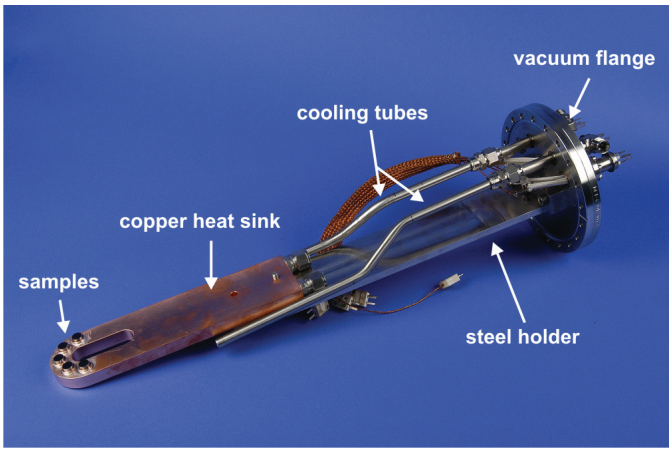

Figure 1.1: Picture of the complete MARION sample holder set-up as it is mounted in the machine. The cooling tubes are not finally connected to the copper heat sink.

The most important part of this sample holder set-up is the copper heat sink. A design drawing of the heat sink is shown in figure 1.2. The circular arrangement of the samples made is necessary to mill the cooling channel into back side turned away from the plasma. For the upper straight part the cooling channel was completed by drilling. After milling, a corresponding lid is attached by electron-beam welding to close the channel. A special oxygen free copper grade had to be used to prevent bubble formation

during the welding process which could lead to a water leakage. The tungsten samples are brazed to a copper base which is than brazed to the copper heat sink. Former works have shown the brazing metal VH780GC, which is a silver based solder (Ag: 71–73 wt%; Cu: 27–29 wt%; Ge: 1.9–2.1 wt%; Co: 0.2–0.4 wt%) with melting temperature of 780 °C, is the most suitable for joining these material combinations and therefore was used here [109].

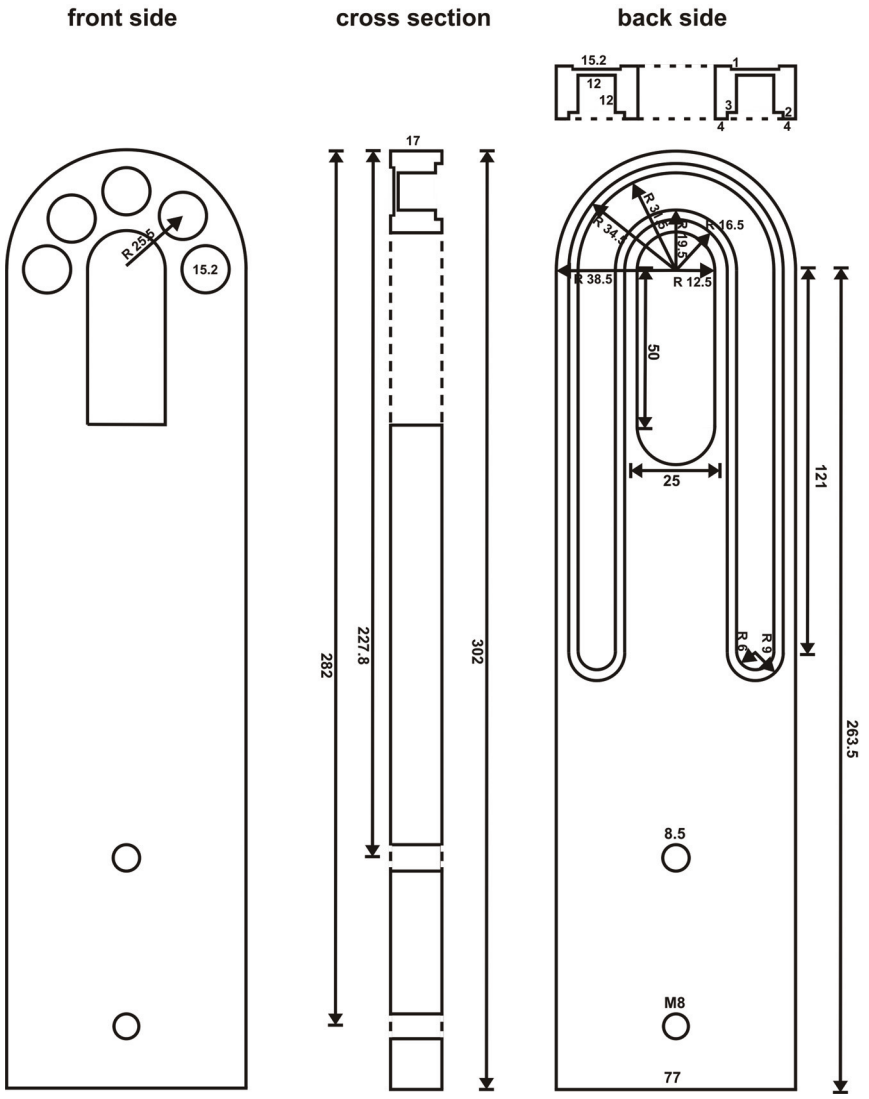

Figure 1.2: Schema of the copper heat sink for the MARION sample holder and cylindrical samples (d=12 mm; h=5 mm). All dimension in mm.

The tungsten samples were brazed to the heat sink by using a copper spacer (h = 3 mm), because the cooling would have been too good and the desired surface temperature of 500 °C could not haven been reached. Another reason is that the copper base makes it possible to remove the targets from the heat sink for later exposure in other machines and/or examination by cutting without destroying the whole device or the sample itself. The combination of these advantages makes it possible to use the copper heat sink for several experiments and to adjust the maximum surface temperature by varying the height of the copper base.

The surface temperatures of the tungsten samples were determined by a single wavelength pyrometer during the plasma exposure. However, the temperature measurement with this method is influenced by a lot of parameters such as the emissivity of the sample, the correct adjustment of the pyrometer spot and the focus. All these parameters had to be determined and verified for the new sample holder set-up. For that reason one of tungsten samples was mounted on a copper plate with a thermocouple and heated by a filament combined with heat shield and thermocouple to predefined temperatures. The pyrometer parameters were adjusted until the deviation of the temperature values measured by the pyrometer and the thermocouples was below 5 %.

B Appendix: Tests at high temperatures in JUDITH 1

For thermal shock experiments in the electron beam device JUDITH 1 (subsection 2.3.1) at elevated temperatures a graphite holder with a tubular heating cartridge was used achieving a maximum temperature of 600 °C. A new heating device had to be bought and adjusted to the conditions in JUDITH 1 to achieve higher temperatures and heating rates. The most suitable heater was the HTR1003 by tectra GmbH in combination with a heat shielding kit as shown in figure 2.1.

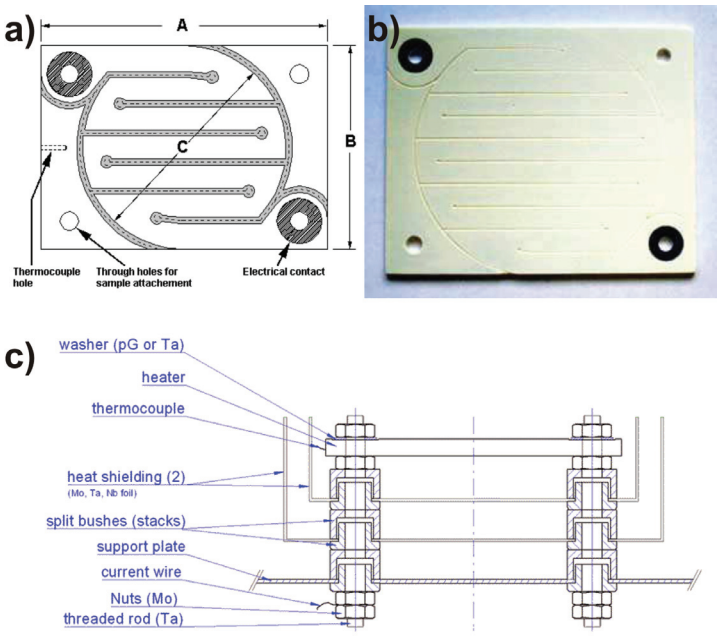

Figure 2.1: Schematic drawings and real picture of the boralectric heating element HTR1003 by tectra GmbH. a) dimensions of the heater A = 93.4 mm, B = 75 mm and C = 75 mm; b) picture of the real heater; c) schema of the heater and heat shielding setup [110].

The heater consists of pyrolytic Boron Nitride (pBN), a dielectric ceramic material, with deposited pyrolytic graphite (PG), an electrical conductor, on both sides and a typical thickness of 2 mm. This material combination makes it a high purity resistance heating element with high heating rates of more than 100 K/s and a power density output of 45 W/cm^2. It is suitable for an application in ultra high vacuum and is inert to corrosive gases, liquids and most molten metals. The maximum operating temperature is 1800 °C but at temperatures above 700 °C the oxidation of pBN becomes a significant problem [110]. Therefore the maximal allowed temperature depends on the oxygen partial pressure and is shown in table B.1.

Table B.1: Overview of the maximal allowed temperatures in dependence on the oxygen partial pressure [110].

atmospheric pressure		700 °C
in vacuum	(oxygen partial pressure $< 10^{-3}$ mbar)	800 °C
in vacuum	(oxygen partial pressure $< 10^{-4}$ mbar)	1000 °C
in vacuum	(oxygen partial pressure $< 10^{-9}$ mbar)	1800 °C

These threshold values in combination with the in subsection 2.3.1 described machine parameters for JUDITH 1 lead to a safe maximum operation temperature of 1200 °C. For temperature above 1000 °C it is important to protect parts other than the samples from being excessively heated. This can be done by a heat shielding kit consisting of two tantalum boxes and ceramic spacers, which shield the heat form the back and the sides of the heater. The schematic setup of this heat shielding is shown in figure 2.1c and the modified setup for JUDITH 1 in figure 2.2.

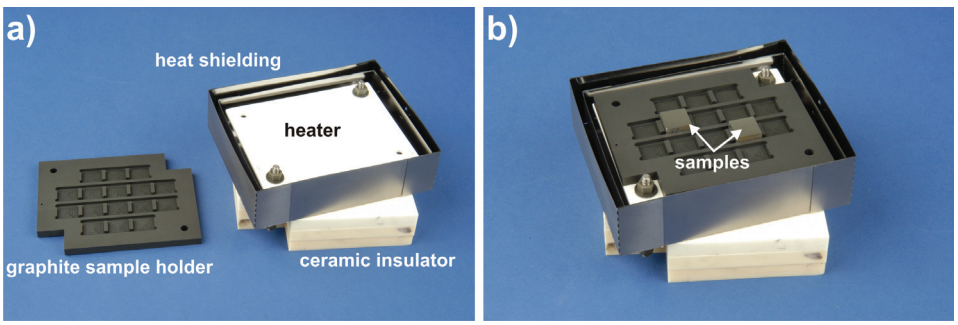

Figure 2.2: New heating system as it is installed in JUDITH 1: a) heater and sample holder separately; b) complete setup with two standard samples.

Additionally to the heat shielding, the heating device is placed on three ceramic plates with three ceramic spacers to protect the back side and especially the xyz-table from overheating. Furthermore a sample holder was designed and manufactured to keep

the samples at fixed positions during the experiments and to protect the heater from the electron beam in case the beam does not hit the sample correctly. A schematic view of the sample holder with all important dimensions is shown in figure 2.3. It is designed for the standard sample geometry of 12 × 12 × 5 mm^3 (subsection 3.2). Graphite was chosen as material for the holder because of its high thermal conductivity and convenient handling in terms of weight and processing. Also important is the fact that graphite is a conductor and will prevent the samples from charging during the exposure, if the holder is grounded. The combination of these properties ensures a fast and homogeneous heating of the samples as well as an easy manufacturing of sample holders adjusted to the current sample geometry. Due to the very high heating rate, controlled by a PID (proportional-integral-derivative) controller the heater is not convenient for temperatures below 400 °C because of a very high overshoot at these low temperatures. Therefore the tubular heating cartridge is used for the temperature range up to 400 °C and the pBN/PG heater for temperatures between 400 °C and 1200 °C. Another reason for the application at temperatures above 400 °C is the bad thermal contact between sample and sample holder and therefore cooling problems during cyclic loading. This problem is less severe at elevated temperatures and becomes negligible at very high temperatures of above 700 °C due to additional radiation cooling effects.

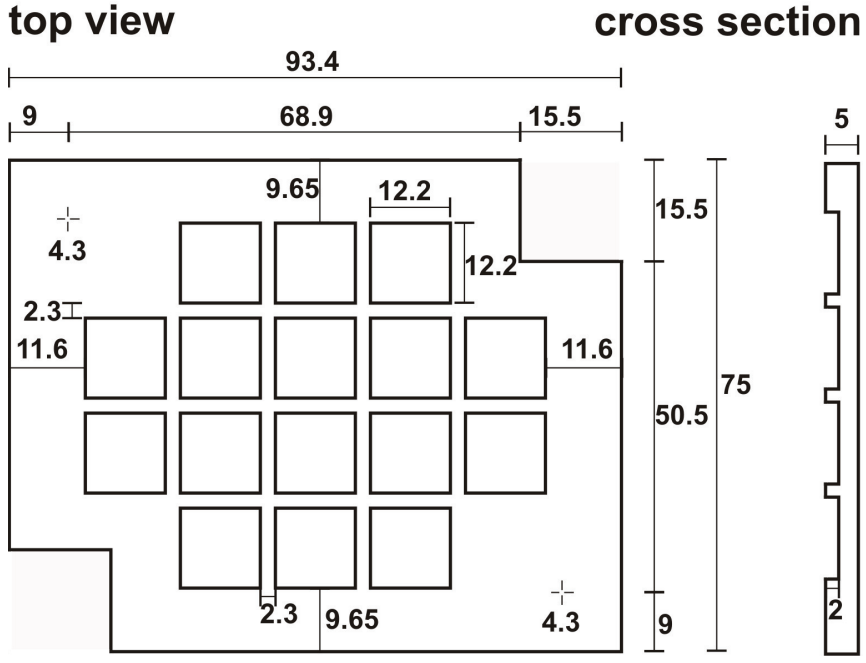

Figure 2.3: Schema of the graphite sample holder for sample geometries of 12 × 12 × 5 mm^3. All dimension in mm.

C Appendix: Detailed measurement results

C.1 Microstructure and density

Table C.1: Average grain dimension for WTa5 before (as received) and after recrystallisation.

	as received			recrystallised		
	feret min [μm]	feret max [μm]	ratio	feret min [μm]	feret max [μm]	ratio
tv	10.5	16.0	0.65	19.1	33.2	0.58
cs	4.9	25.3	0.19	15.3	23.0	0.67

Table C.2: Densities of the as received tungsten grades at RT.

	W-UHP	pure W	WVMW	WTa1	WTa5
density [gcm^{-3}]	18.94	19.03	18.97	18.92	18.80

C.2 Database for the calculation of the thermal conductivities

Temperature profile of the density, specific heat capacity and thermal diffusivity to calculate the thermal conductivity for all five tungsten grades in subsection 3.1.3.

Table C.3: Literature values for the temperature dependence of the density of tungsten [43].

temperature [°C]	RT	200	400	600	800	1000	1200
density [gcm^{-3}]	19.30	19.25	19.20	19.15	19.10	19.04	18.98

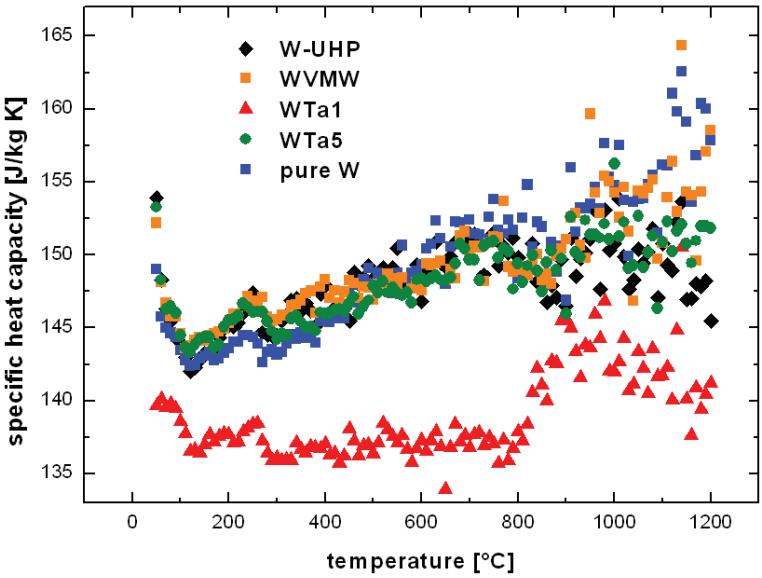

Figure 3.1: Specific heat capacity for all five tungsten grades measured with the DSC (subsection 2.2.2). The measurement error for each value is in the range of ±5 %.

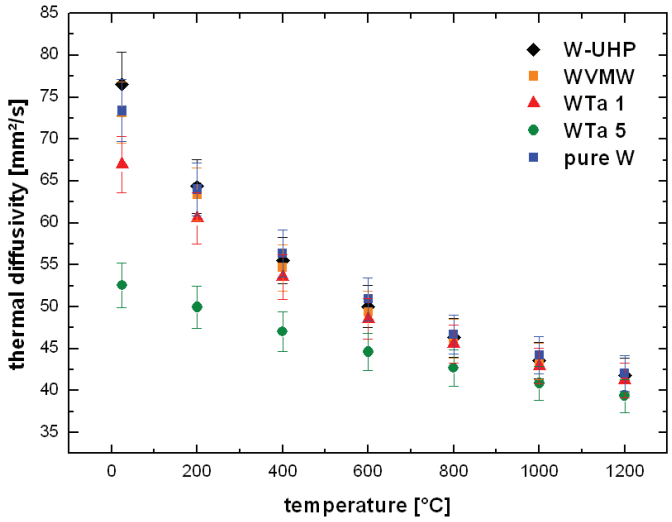

Figure 3.2: Thermal diffusivity for all five tungsten grades measured with the laser-flash method (subsection 2.2.3).

C.3 Arithmetic mean roughness of tungsten with different grain structures

Table C.4: Arithmetic mean roughness R_a in μm for the samples presented in figure 3.26 and the corresponding longitudinal samples.

W-UHP	RT			400 °C		
grain structure	L	T	R	L	T	R
0.16 GWm^{-2}	0.18	0.24	0.22	0.07	0.19	0.24
0.32 GWm^{-2}	0.46	0.38	2.22	0.58	0.68	1.14

Table C.5: Arithmetic mean roughness R_a in μm for the samples presented in figure 3.29 and the corresponding longitudinal samples.

pure W	RT			400 °C		
grain structure	L	T	R	L	T	R
0.16 GWm^{-2}	0.12	0.10	0.28	0.11	0.12	0.29
0.32 GWm^{-2}	0.74	0.42	1.11	0.59	0.49	0.97

Table C.6: Arithmetic mean roughness R_a in μm for the samples presented in figure 3.32 and the corresponding longitudinal samples.

WVMW	RT			400 °C		
grain structure	L	T	R	L	T	R
0.16 GWm^{-2}	0.06	0.10	0.21	0.09	0.08	0.29
0.32 GWm^{-2}	0.65	0.31	1.27	0.38	0.46	0.98

Table C.7: Arithmetic mean roughness R_a in μm for the samples presented in figure 3.35 and the corresponding longitudinal samples.

WTa1	RT			400 °C		
grain structure	L	T	R	L	T	R
0.16 GWm^{-2}	0.08	0.08	0.19	0.08	0.08	0.29
0.32 GWm^{-2}	0.08	0.20	0.89	0.25	0.45	0.62

Table C.8: Arithmetic mean roughness R_a in μm for the samples presented in figure 3.38 and the corresponding longitudinal samples.

WTa5	RT			400 °C		
grain structure	L	T	R	L	T	R
0.16 GWm^{-2}	0.08	0.09	0.11	0.06	0.09	0.15
0.32 GWm^{-2}	0.07	0.18	0.63	0.06	0.27	0.60
0.63 GWm^{-2}	0.61	0.45	0.80	0.07	0.46	0.80

C.4 Crack parameters for tungsten with different grain structures

Crack parameters for the thermal shock crack networks presented in subsection 3.4.2 for different grain structures (figures 3.41 and 3.42).

Table C.9: Maximum and average values for crack distance, width and depth of W-UHP with different grain orientations.

W-UHP	longitudinal	transversal	recrystallised
max. crack distance [μm]	1740	2989	1612
avg. crack distance [μm]	481	246	392
max. crack width [μm]	6	4	35
avg. crack width [μm]	4	2	23
max. crack depth [μm]	227	354	447
avg. crack depth [μm]	156	230	183

Table C.10: Maximum and average values for crack distance, width and depth of pure W with different grain orientations.

pure W	longitudinal	transversal	recrystallised
max. crack distance [μm]	1638	3139	2005
avg. crack distance [μm]	503	242	482
max. crack width [μm]	6	6	30
avg. crack width [μm]	3	3	14
max. crack depth [μm]	208	275	414
avg. crack depth [μm]	175	114	388

Table C.11: Maximum and average values for crack distance, width and depth of WVMW with different grain orientations.

WVMW	longitudinal	transversal	recrystallised
max. crack distance [μm]	2044	446	2657
avg. crack distance [μm]	656	118	494
max. crack width [μm]	6	4	26
avg. crack width [μm]	5	2	16
max. crack depth [μm]	200	245	370
avg. crack depth [μm]	97	105	313

Table C.12: Maximum and average values for crack distance, width and depth of WTa1 with different grain orientations.

WTa1	longitudinal	transversal	recrystallised
max. crack distance [μm]	1379	360	1457
avg. crack distance [μm]	429	124	475
max. crack width [μm]	14	2	17
avg. crack width [μm]	8	2	11
max. crack depth [μm]	350	214	428
avg. crack depth [μm]	194	88	365

Table C.13: Maximum and average values for crack distance, width and depth of WTa5 with different grain orientations.

WTa5	longitudinal	transversal	recrystallised
max. crack distance [μm]	1019	1849	1864
avg. crack distance [μm]	335	243	529
max. crack width [μm]	6	6	17
avg. crack width [μm]	5	3	11
max. crack depth [μm]	175	429	529
avg. crack depth [μm]	72	183	392

Bibliography

[1] J. Ongena, G. van Oost; Energy for future centuries; *Fusion Science and Technology* 53 (2T) 3–15 (2008); http://www.carolusmagnus.net/papers/2007/docs/IN1_Ongena_paper.pdf. (citation on page: 1)

[2] M. P. Fewell; The atomic nuclide with the highest mean binding energy; *American Journal of Physics* 63 (7) 653–658 (1995); doi: 10.1119/1.17828; http://ajp.aapt.org/resource/1/ajpias/v63/i7/p653_s1. (citations on pages: 1 and 2)

[3] K. Niu; Nuclear fusion; Cambridge university press (1989). (citations on page: 2)

[4] F. Ajzenberg-Selove; Energy levels of light nuclei A = 5-10; *Nuclear Physics A* 490 (1) 1–225 (1988); ISSN 0375-9474; doi: 10.1016/0375-9474(88)90124-8; http://www.sciencedirect.com/science/article/pii/0375947488901248. (citation on page: 2)

[5] R. A. Gross; Fusion energy; John Wiley & sons (1984). (citation on page: 2)

[6] S. Glasstone, R. H. Loveberg; Controlled thermonuclear reactions : an introduction to theory and experiment; Huntington, N.Y. : R. E. Krieger Pub. Co. (1975). (citation on page: 3)

[7] K. Pinkau, U. Schuhmacher; Kernfusion mit magnetisch eingeschlossenen Plasmen; *Physik in unserer Zeit* 13 (5) 138–154 (1982). (citations on page: 3)

[8] J. Ongena, G. Van Oost; Controlled thermonuclear fusion; EUROATOM association (1999). (citation on page: 4)

[9] http://www.bmbf.de/de/2270.php; Bundesministerium für Bildung und Forschung (2011). (citation on page: 4)

[10] R. Aymar; ITER R&D: Executive Summary: Designe Overview; *Fusion Engineering and Design* 55 (2–3) 107–118 (2001). (citations on pages: 4 and 6)

[11] N. Holtkamp; The status of the ITER design; *Fusion Engineering and Design* 84 98–105 (2009). (citations on pages: 4 and 6)

[12] Summary of the ITER Final Design Report; presented by the ITER director (2001). (citations on pages: 4 and 6)

[13] ITER Organisation (2009); http://www.iter.org. (citations on pages: 5 and 6)

[14] G. Janeschitz; Plasma-wall interaction issues in ITER; *Journal of Nuclear Materials* 290-293 (0) 1–11 (2001); doi: 10.1016/S0022-3115(00)00623-1; http://www.sciencedirect.com/science/article/pii/S0022311500006231. (citation on page: 5)

[15] M. Merola, W. Dänner et al.; European contribution to the development of the ITER divertor; *Fusion Engineering and Design* 66–68 211–217 (2003). (citation on page: 6)

[16] J. Roth, E. Tsitrone et al.; Recent analysis of key plasma wall interactions issues for ITER; *Journal of Nuclear Materials* 390-391 (0) 1 – 9 (2009); ISSN 0022-3115; doi: 10.1016/j.jnucmat.2009.01.037; http://www.sciencedirect.com/science/article/pii/S0022311509000506. (citations on pages: 6, 9, and 10)

[17] A. Kleyn, W. Koppers et al.; Plasma-surface interaction in ITER; *Vacuum* 80 1098–1106 (2006). (citation on page: 7)

[18] G. Federici, H. Wuerz et al.; Erosion of plasma-facing components in ITER; *Fusion Engineering and Design* 61–62 (0) 81–94 (2002); ISSN 0920–3796; doi: 10.1016/S0920-3796(02)00298-3; http://www.sciencedirect.com/science/article/pii/S0920379602002983. (citation on page: 7)

[19] M. Merola, G. Vieider et al.; European achievements for ITER high heat flux components; *Fusion Engineering and Design* 56–57 173–178 (2001). (citations on pages: 7 and 8)

[20] J. Linke; High heat flux performance of plasma facing components under service conditions in future fusion reactors; *Transactions of Fusion Science and Technology* 49 455–464 (2006); http://www.carolusmagnus.net/papers/2005/docs/linke_plasma_facing_materials.pdf. (citations on pages: 7 and 9)

[21] A. Loarte, G. Saibene et al.; Characteristics of type I ELM energy and particle losses in existing devices and their extrapolation to ITER; *Plasma Physics and Controlled Fusion* 45 1549–1569 (2003). (citation on page: 7)

[22] D. Hill; A review of ELMs in divertor tokamaks; *Journal of Nuclear Materials* 241–243 182–198 (1997). (citation on page: 8)

[23] M. Becoulet, G. Huysmans et al.; Edge localized modes control: experiment and theory; *Journal of Nuclear Materials* 337–339 (0) 677–683 (2005); doi: 10.1016/j.jnucmat.2004.09.074; http://www.sciencedirect.com/science/article/pii/S0022311504009705. (citation on page: 8)

[24] J. Linke, P. Lorenzetto et al.; EU development of high heat flux components; *Fusion Science and Technology* 47 678–658 (2005). (citations on page: 8)

[25] O. Gruber, K. Lackner et al.; Vertical Displacement Events and Halo Currents; *Plasma Phys. Controls* 35 B191–B204 (1993). (citation on page: 8)

[26] A. Hassanein, T. Sizyuk et al.; Vertical displacement events: A serious concern in future ITER operation; *Fusion Engineering and Design* 83 1020–1024 (2008). (citation on page: 8)

[27] A. Kukushkin, H. Pacher et al.; Effect of neutral transport on ITER divertor performance; *Nuclear Fusion* 45 608–616 (2005); doi: 10.1088/0029-5515/45/7/008. (citation on page: 9)

[28] G. Federici, J. Brooks et al.; Assessment of erosion and tritium codeposition in ITER-FEAT; *Journal of Nuclear Materials* 290-293 (0) 260 – 265 (2001); ISSN 0022-3115; doi: 10.1016/S0022-3115(00)00627-9; http://www.sciencedirect.com/science/article/pii/S0022311500006279. (citation on page: 9)

[29] H. Bolt, V. Barabash et al.; Plasma facing and high heat flux materials - needs for ITER and beyond; *Journal of Nuclear Materials* 307–311 43–52 (2002); doi: 10.1016/S0022-3115(02)01175-3; http://www.sciencedirect.com/science/article/pii/S0022311502011753. (citations on pages: 9 and 11)

[30] J. Wesson; Tokamaks; Oxford : Clarendon Press (2004). (citation on page: 9)

[31] B. T. Kelly; Irradiation damage to solids; Oxford, Pergamon Press (1966). (citation on page: 9)

[32] C. Wong; Neutron wall loading of Tokamak reactors; *Journal of Nuclear Materials* 283-287, Part 1 (0) 588 – 592 (2000); ISSN 0022-3115; doi: 10.1016/S0022-3115(00)00145-8; http://www.sciencedirect.com/science/article/pii/S0022311500001458. (citation on page: 9)

[33] C. Wu, C. Alessandrini et al.; Progress of the European R&D on plasma-wall interactions, neutron effects and tritium removal in ITER plasma facing materials; *Fusion Engineering and Design* 56-57 (0) 179 – 187 (2001); ISSN 0920-3796; doi: 10.1016/S0920-3796(01)00255-1; http://www.sciencedirect.com/science/article/pii/S0920379601002551. (citation on page: 9)

[34] L. Singheiser, T. Hirai et al.; Plasma-facing materials for thermo-nuclear fusion devices; *Transactions of The Indian Institute of Metals* 62 (2) 123–128 (2009). (citations on pages: 10, 11, and 102)

[35] J. Pamela, G. Matthews et al.; An ITER-like wall for JET; *Journal of Nuclear Materials* 363–365 (0) 1–11 (2007); ISSN 0022-3115; doi: 10.1016/j.jnucmat.2006.12.056; http://www.sciencedirect.com/science/article/pii/S0022311506006283; Plasma-Surface Interactions-17. (citation on page: 10)

[36] F. Scaffidi-Argentina, G. Longhurst et al.; Beryllium R&D for fusion applications; *Fusion Engineering and Design* 51-52 (0) 23 – 41 (2000); ISSN 0920-3796; doi: 10.1016/S0920-3796(00)00312-4; http://www.sciencedirect.com/science/article/pii/S0920379600003124. (citations on pages: 11 and 12)

[37] J. Linke, M. Akiba et al.; Performance of beryllium, carbon, and tungsten under intense thermal fluxes; *Journal of Nuclear Materials* 241–243 (0) 1210–1216 (1997); ISSN 0022-3115; doi: 10.1016/S0022-3115(97)80222-X; http://www.sciencedirect.com/science/article/pii/S002231159780222X. (citations on pages: 11 and 12)

[38] V. Barabash, M. Akiba et al.; Carbon fiber composites application in ITER plasma facing components; *Journal of Nuclear Materials* 258-263 (Part 1) 149–159 (1998); ISSN 0022-3115; doi: 10.1016/S0022-3115(98)00267-0; http://www.sciencedirect.com/science/article/B6TXN-45JC0B6-J/2/e4322ebc147b20c8bd741db60e5beea5. (citations on pages: 11 and 12)

[39] V. Philipps; Tungsten as material for plasma-facing components in fusion devices; *Journal of Nuclear Materials* 415 (1, Supplement) S2 – S9 (2011); ISSN 0022-3115; doi: 10.1016/j.jnucmat.2011.01.110; http://www.sciencedirect.com/science/article/pii/S0022311511001589; Proceedings of the 19th International Conference on Plasma-Surface Interactions in Controlled Fusion. (citations on pages: 11, 12, and 102)

[40] ITER Materials Assessment Report (MAR); ITER Doc. G 74 MA 10 W0.3: internal project document distributed to the ITER Participants (2004). (citations on pages: 11 and 35)

[41] S. Schider; Refractory Metals - Powder Metallurgical Materilas for High Tech Usage; verlag moderne industrie (1991). (citations on pages: 11 and 37)

[42] K. B. Shedd; Tungsten; U.S. Geological Survey, Mineral Commodity Summaries (January 2007); http://minerals.usgs.gov/minerals/pubs/commodity/tungsten/tungsmcs07.pdf. (citation on page: 11)

[43] J. W. Davis et al.; ITER Material Properties Handbook (1997). (citations on pages: 11, 48, and 113)

[44] V. Barabash, M. Akiba et al.; Selection, development and characterisation of plasma facing materials for ITER; *Journal of Nuclear Materials* 233–237 718–723 (1996). (citation on page: 12)

[45] P. Varga, E. Taglauer; Preferential sputtering of compounds due to light ion bombardmnet; *Journal of Nuclear Materials* 111–112 726–731 (1982). (citation on page: 12)

[46] O. Ogorodnikova, J. Roth et al.; Ion-driven deuterium retention in tungsten; *Journal of Applied Physics* 103 034902 (2008). (citations on pages: 12, 100, and 101)

[47] M. R. Gilbert, J.-C. Sublet; Neutron-induced transmutation effects in W and W-alloys in a fusion environment; *Nuclear Fusion* 51 043005 (2011); doi: doi:10.1088/0029-5515/51/4/043005. (citation on page: 12)

[48] V. Barabash, G. Federici et al.; Material/plasma surface interaction issues following neutron damage; *Journal of Nuclear Materials* 313–316 42–51 (2003). (citation on page: 12)

[49] E. Wessel; Private communication (2009). (citations on pages: 13 and 27)

[50] J. Linke, H. Bolt et al.; High heat flux simulation experiments with improved electron beam diagnostics; *Journal of Nuclear Materials* 283-287 (PART II) 1152–1156 (2000); www.scopus.com; Cited By (since 1996): 13. (citation on page: 13)

[51] G. van Rooij, V. Veremiyenko et al.; Extreme hydrogen plasma densities achieved in a linear plasma generator; *Applied Physics Letters* 90 121501 (2007). (citations on pages: 13 and 30)

[52] B. Schweer, F. Irrek et al.; In situ diagnostic for monitoring of deuterium and tritium in re-deposited carbon layers by laser induced desorption; *Journal of Nuclear Materials* 363-365 1375–1379 (2007); doi: 10.1016/j.jnucmat.2007.01.247; http://www.sciencedirect.com/science/article/pii/S0022311507002760. (citations on pages: 13 and 32)

[53] T. Hirai, G. Pintsuk et al.; Cracking failure study of ITER-reference tungsten grade under single pulse thermal shock loads at elevated temperatures; *Journal of Nuclear Materials* 390–391 751–754 (2009). (citation on page: 15)

[54] K. Wittlich, T. Hirai et al.; Damage structure in divertor armor materials exposed to multiple ITER relevant ELM loads; *Fusion Engineering and Design* 84 1982–1986 (2009). (citations on pages: 15 and 89)

[55] K. Umstadter, R. Doerner et al.; Enhanced erosion of tungsten plasma-facing components subject to simultaneous heat pulses and deuterium plasma; *Journal of Nuclear Materials* 386-388 (0) 751 – 755 (2009). (citations on pages: 15 and 89)

[56] I. Uytdenhouwen; Degradation of First Wall Materials under ITER Relevant Loading Conditions; Ph.D. thesis Universiteit Gent (2010). (citations on pages: 18, 19, 44, and 46)

[57] http://www.grindosonic.com; GrindoSonic (2003). (citation on page: 19)

[58] H. Czichos, T. Saito et al.; Springer Handbook of Materials Measurement Methods; Springer, Berlin (2006). (citation on page: 20)

[59] JW Lemmens Geldenaaksebaan 456 B-3001 Leuven; Operating Instructions for the GrindoSonic MK5i instrument (2010). (citation on page: 21)

[60] K. Maglic, A. Cezairliyan et al.; Compendium of Thermophysical Property Measurement Methods, 2: Recommended Measurement Techniques and Practices; Plenum Press, New York 1st edition (1992). (citations on pages: 22 and 24)

[61] B. Wunderlich; Thermal Analysis; Academic Press, MA (1990). (citation on page: 22)

[62] C. Kittel; Introduction to solid state physics; New York, NY : Wiley 8th edition (2005). (citations on page: 23)

[63] W. J. Parker, R. J. Jenkins et al.; Flash Method of Determining Thermal Diffusivity, Heat Capacity, and Thermal Conductivity; *Journal of Applied Physics* 32 (9) 1679 –1684 (sep 1961); ISSN 0021-8979; doi: 10.1063/1.1728417. (citation on page: 23)

[64] Y. S. Touloukian, R. W. Powell et al.; Thermophysical Properties of Matter Volumen 10: Thermal Diffusivity; IFI/Plenum Press New York-Washington (1973). (citation on page: 23)

[65] A. K. Knudsen, H. Delzer et al.; Laser flash thermal conductivity apparatus and method (1990). (citation on page: 24)

[66] R. Duwe, W. Kuehnlein et al.; The new Electron Beam Facility for Materials Testing in Hot Cells; *Fusion Technology* pp. 356–358 (1995). (citations on page: 26)

[67] S. Schiller, U. Heisig et al.; Elektronenstrahltechnologie; Wissenschaftliche Verlagsgesellschaft Stuttgart, Lizenz des Verlag Technik, VEB Berlin (1977). (citations on pages: 26 and 27)

[68] M. von Ardenne; Tabellen zur angewandten Physik volume 1; Deutscher Verlag der Wissenschaften 2nd edition (1973). (citations on pages: 26, 27, and 28)

[69] S. Flügge; Handbuch der Physik, Band XXI; Springer-Verlag (1956). (citation on page: 27)

[70] J. Westerhout, W. R. Koppers et al.; PSI research in the ITER divertor parameter range at the FOM PSI-lab; *Physica Scripta* T128 18–22 (2007); doi: doi:10.1088/0031-8949/2007/T128/004. (citation on page: 30)

[71] G. Wright, A. Kleyn et al.; Hydrogenic retention in tungsten exposed to ITER divertor relevant plasma flux densities; *Journal of Nuclear Materials* 390-391 610 – 613 (2009). (citations on pages: 30 and 100)

[72] G. De Temmerman, J. J. Zielinski et al.; ELM simulation experiments on Pilot-PSI using simultaneous high flux plasma and transient heat/particle source; *Nuclear Fusion* 51 (7) 073008 (2011); doi: doi:10.1088/0029-5515/51/7/073008. (citation on page: 30)

[73] H. van der Meiden, R. Al et al.; High sensitivity imaging Thomson scattering for low temperature plasma; *Review of Scientific Instruments* 79 013505 (2008). (citation on page: 30)

[74] M. Lochter, R. Uhlemann et al.; High heat flux ion beam test facility for material research and development; *Fusion Technology* 19 2101–2111 (1991). (citations on page: 31)

[75] D. Nicolai, A. Charl et al.; Upgrade of the material ion beam test facility MARION for enhanced requirements of JET and ITER; *Fusion Engineering and Design* 86 (9–11) 2791–2794 (2011); doi: 10.1016/j.fusengdes.2011.05.005; http://www.sciencedirect.com/science/article/pii/S092037961100490X; Proceedings of the 26th Symposium of Fusion Technology (SOFT-26). (citations on page: 31)

[76] M. Zlobinski; Laserinduzierte Desorption an plasmaerzeugten Wandbeschichtungen; Master's thesis Heinrich-Heine-Universität Düsseldorf (March 2009). (citations on page: 32)

[77] K. J. Bathe; Finite Element Procedures; Prentice Hall 2nd edition (1995). (citation on page: 34)

[78] V. Barabash, A. Peacock et al.; Materials challenges for ITER - Current status and future activities; *Journal of Nuclear Materials* 367–370, Part A (0) 21–32 (2007); doi: 10.1016/j.jnucmat.2007.03.017; http://www.sciencedirect.com/science/article/pii/S0022311507003340. (citation on page: 35)

[79] E. Lassner, W.-D. Schubert; Tungsten: Properties, Chemistry, Technology of the Element, Alloys, and Chemical Compounds; Kluwer Academic / Plenum Plublishers, New York (1999); ISBN 978-0-306-45053-2. (citations on pages: 35, 36, 39, 41, 45, 47, and 84)

[80] A. Giannattasio, S. G. Roberts; Strain-rate dependence of the brittle-to-ductile transition temperature in tungsten; *Philosophical Magazine* 87 (17) 2589–2598 (2007); doi: 10.1080/14786430701253197; http://www.tandfonline.com/doi/abs/10.1080/14786430701253197. (citation on page: 35)

[81] J. Davis, V. Barabash et al.; Assessment of tungsten for use in the ITER plasma facing components; *Journal of Nuclear Materials* 258-263, Part 1 (0) 308 – 312 (1998); ISSN 0022-3115; doi: 10.1016/S0022-3115(98)00285-2; http://www.sciencedirect.com/science/article/pii/S0022311598002852. (citation on page: 35)

[82] http://www.plansee.com/; Plansee Group homepage (2009). (citations on pages: 36, 37, and 39)

[83] M. Rieth, A. Hoffmann; Fracture behaviour of ungsten based alloys depending on microstructure and notch fabrication method; *Fusion Science and Technology* 56 1018–1022 (August 2009). (citation on page: 39)

[84] B. Bewlay, N. Lewis et al.; Observations on the Evolution of Potassium Bubbles in Tungsten Ingots during Sintering; *Metallurgical Transactions A* 23A 121 (January 1992). (citation on page: 39)

[85] K. H. Matucha; Structure and properties of nonferrous alloys; VCH Verlagsgesellschaft mbH (1996). (citation on page: 39)

[86] S. V. Nagender Naidu, P. Rama Rao; Phase diagrams of binary tungsten alloys; Calcutta : Indian Institute of Metals (1991). (citation on page: 39)

[87] G. Gottstein; Physikalische Grundlagen der Materialkunde; Springer-Verlag Berlin Heidelberg (2007). (citation on page: 42)

[88] V. Raghavan; Physical Metallurgy: Principles and Practice; Prentice-Hall of India Pvt.Ltd (2006). (citation on page: 42)

[89] J. P. Morniroli; Low Temperature Embrittlement of Undoped and Doped Tungsten; Elsevier, London (1989). (citation on page: 45)

[90] W. Martienssen, H. Warlimont; Springer handbook of condensed matter and materials data; Springer Berlin (2005). (citations on page: 45)

[91] E. Pink, R. Eck; Refractory Metals and Their Alloys; Wiley-VCH Verlag GmbH & Co. KGaA (2006); ISBN 9783527603978; doi: 10.1002/9783527603978.mst0088; http://dx.doi.org/10.1002/9783527603978.mst0088. (citation on page: 45)

[92] G. L. Krasko; Effect of impurities on the electronic structure of grain boundaries and intergranular cohesion in iron and tungsten; *Materials Science and Engineering: A* 234–236 (0) 1071–1074 (1997); ISSN 0921-5093; doi: 10.1016/S0921-5093(97)00417-6; http://www.sciencedirect.com/science/article/pii/S0921509397004176. (citation on page: 45)

[93] E. Pink, R. Eck; Materials Science and Technology: A comprehensive treatment Volume 8: Structure and Properties of Nonferrous Alloys volume 8; VCH Verlagsgesellschaft mbH, Weinheim (1996). (citations on page: 47)

[94] C. Uher; Thermal Conductivity: Theory, Properties, and Applications (Thermal conductivity of Metals); Springer US (2005). (citation on page: 48)

[95] T. Hirai, G. Pintsuk; Thermo-mechanical calculations on operation temperature limits of tungsten as plasma facing material; *Fusion Engineering and Design* 82 389–393 (2007). (citation on page: 51)

[96] M. Merola, V. Barabash et al.; ITER plasma facing component materials database in ANSYS format; *ITER doc. G 17 MD 71 96-11-19 W 0.1* Version 1.3 (2000). (citation on page: 53)

[97] R. W. Armstrong, S. M. Walley; High strain rate properties of metals and alloys; *International Materials Reviews* 53 105–128 (2008); doi: 10.1179/174328008X277795. (citation on page: 71)

[98] T. Dümmer, J. C. Lasalvia et al.; Effect of strain rate on plastic flow and failure in polycrystalline tungsten; *Acta Metallurgica* 46 (17) 6267–6290 (1998). (citation on page: 71)

[99] F. J. Humphreys, M. Hatherly; Recrystallization and Related Annealing Phenomena; Pergamon 2nd edition (2003). (citation on page: 74)

[100] T. Loewenhoff, A. Bürger et al.; Evolution of tungsten degradation under combined high cycle ELM and steady state heat loads; *Physica Scripta* T145 (1, Supplement) 014057 (2011); doi: 10.1088/0031-8949/2011/T145/014057; http://iopscience.iop.org/1402-4896/2011/T145/014057/pdf/1402-4896_2011_T145_014057.pdf; Proceedings of the 19th International Conference on Plasma-Surface Interactions in Controlled Fusion. (citations on pages: 79, 86, and 102)

[101] T. Loewenhoff; Combined steady state and high cycle transient heat load simulation with the electron beam facility JUDITH 2; Ph.D. thesis Rheinisch-Westfälischen Technischen Hochschule Aachen (2012). (citations on pages: 84 and 86)

[102] D. A. Komarov, A. V. Markin et al.; Role of grain boundaries and carbon deposition in deuterium retention behavior of deuterium plasma exposed tungsten; *Journal of Nuclear Materials* 290–293 433–436 (2001). (citation on page: 90)

[103] P. Cotterill; The hydrogen embrittlement of metals; *Progress in Materials Science* 9 (4) 205 – 250, IN1–IN2, 251–266, IN3–IN4, 267–301 (1961). (citations on pages: 100 and 101)

[104] R. Jewett, R. Walter et al.; Hydrogen Environment Embrittlement of Metals; *NASA CR-2163* (1973). (citation on page: 100)

[105] G. Wright, E. Alves et al.; Hydrogen retention of high-Z refractory metals exposed to ITER divertor-relevant plasma conditions; *Nuclear Fusion* 50 055004 (2010). (citations on page: 100)

[106] T. Venhaus, R. Causey et al.; Behavior of tungsten exposed to high fluences of low energy hydrogen isotopes; *Journal of Nuclear Materials* 290–293 505–508 (2001). (citation on page: 100)

[107] A. Haasz, J. Davis et al.; Deuterium retention in tungsten for fusion use; *Journal of Nuclear Materials* 258–263 889–895 (1998). (citation on page: 100)

[108] H. Eleveld, A. van Veen; Void growth and thermal desorption of deuterium from voids in tungsten; *Journal of Nuclear Materials* 212–215 1421–1425 (1994). (citation on page: 101)

[109] G. H. Ritz; Performance of Tungsten-Based Materials and Components under ITER and DEMO Relevant Steady-State Thermal Loads; Ph.D. thesis Rheinisch-Westfälischen Technischen Hochschule Aachen (2011); ISBN 978-3-89336-755-9. (citation on page: 106)

[110] http://www.tectra.de/heater.htm; tectra GmbH Homepage (June 2010). (citations on pages: 109 and 110)

Danksagung

Zuerst möchte ich mich bei meinem Doktorvater Prof. Dr. L. Singheiser für die Gelegenheit bedanken, diese Arbeit am Institut für Energie und Klimaforschung (IEK-2) durchführen und fertig stellen zu können.

Bedanken möchte ich mich auch bei Prof. Dr. B. Unterberg dafür, dass er sich bereiterklärt hat das Korreferat für diese Arbeit zu übernehmen.

Mein Dank gilt auch Dr. J. Linke für die herzliche und sehr gute Betreuung. Während meiner Promotion hatte er immer ein offenes Ohr für meine kleinen und großen Fragen oder Probleme.

Danken möchte ich den Postdocs: Dr. G. Pintsuk für die wertvollen Anregungen und die bereitwillige Weitergabe seines Wissens über Wolfram, sowie Dr. J. Du und Dr. C. Thomser für die angenehme und produktive Arbeitsatmosphäre.

Für die Unterstützung bei der Vermessung von Mikrostrukturen und den unkomplizierten Ablauf bei der Probenfertigung danke ich G. Knauf und G. Böling.

Ebenso bedanke ich mich bei den Mitarbeitern des Heißmateriallabors (HML), besonders Dr. M. Rödig und Dr. A. Schmidt für die wissenschaftliche Betreuung sowie A. Bürger. Für die Unterstützung bei den thermophysikalischen Untersuchungen danke ich F. Gormann und D. Pitzer. Sehr herzlich möchte ich mich auch bei M. Hühnerbein und M. Diederichs für die gute Zusammenarbeit bei der Durchführung der Elektronenstrahlexperimente bedanken.

W. Behr, Th. Koppitz und D. Nicolai gilt mein Dank für die Hilfe bei der Konstruktion eines Probenhalters für die Ionenstrahltestanlage MARION und die Unterstützung bei der Durchführung der Tests.

Nicht vergessen möchte ich in diesem Zusammenhang die gute Zusammenarbeit mit Kolleginnen und Kollegen anderer Forschungseinrichtungen. Besonders erwähnen möchte ich Dr. I. Uytdenhouwen vom SCK•CEN, Belgien, und Dr. G. De Temmermann vom DIFFER, Niederlande.

Mein Dank gilt auch allen Mitarbeitern des IEK-2. Besonders Dr. E. Wessel, V. Gutzeit und J. Bartsch für ihre Hilfe bei der Metallographie und den REM Untersuchungen sehr vieler Wolframproben. J. Mönch danke ich für die Unterstützung bei den Grindo Sonic Versuchen, M. Felden für die schnelle und unkomplizierte Art bei der Bearbeitung vieler Druckaufträge, sowie die hohe Qualität und Sorgfalt beim Photographieren von Proben und Probenhaltern aller Art. Außerdem möchte ich P. Joecken danken, der bei großen und kleinen Soft-/Hardwareproblemen immer zur Stelle war um größeren Schaden oder Datenverlust zu verhindern.

Bedanken möchte ich mich auch bei meinen Kollegen und Mitstudenten. Vor allem bei Th. Loewenhoff und G. Ritz für die sehr angenehme Arbeitsatmosphäre während der vergangenen drei Jahre. Es war nie langweilig sich mit euch ein Büro zu teilen. M. Zlobinski möchte ich für die Hilfe und Unterstützung bei den Lasertests danken. C. Asensio Jiménez danke ich für ihre fröhliche Art, mit der sie es immer geschafft hat den Arbeitsalltag aufzulockern.

Abschließend danke ich meiner Familie und meinen Freunden. Mein besonderer Dank gilt meinen Eltern. Ohne euch und eure Unterstützung wäre mir manches sehr viel schwerer gefallen oder überhaupt nicht möglich gewesen. Meinen Freunden und speziell meiner Freundin möchte ich dafür danken, dass sie mich und meine nicht immer beste Laune, gerade in den letzten Monaten, geduldig ertragen haben.

Band / Volume 147
Untersuchungen zum Sicherheits- und Transmutationsverhalten innovativer Brennstoffe für Leichtwasserreaktoren
O. Schitthelm (2012), V, 150 pp.
ISBN: 978-3-89336-806-8

Band / Volume 148
IEK-Report 2011. Klimarelevante Energieforschung
(2012), ca. 250 pp.
ISBN: 978-3-89336-808-2

Band / Volume 149
IEK-Report 2011. Climate-Relevant Energy Research
(2012), ca. 250 pp.
ISBN: 978-3-89336-809-9

Band / Volume 150
Netzintegration von Fahrzeugen mit elektrifizierten Antriebssystemen in bestehende und zukünftige Energieversorgungsstrukturen (2012)
ISBN: 978-3-89336-811-2

Band / Volume 151
Stratospheric ClOOCl chemistry at high solar zenith angles
O. Suminska-Ebersoldt (2012), VI, 126 pp
ISBN: 978-3-89336-817-4

Band / Volume 152
Keramiken und Keramikkombinationen zur Feinstpartikelabscheidung mit Hilfe thermisch induzierter Potentialfelder und Elektronenemissionen
D. Wenzel (2012), XXV, 155 pp
ISBN: 978-3-89336-820-4

Band / Volume 153
Bildung von sekundären Phasen bei tiefengeologischer Endlagerung von Forschungsreaktor-Brennelementen – Struktur- und Phasenanalyse
A. Neumann (2012), 329 pp
ISBN: 978-3-89336-822-8

Band / Volume 154
Coupled hydrogeophysical inversion for soil hydraulic property estimation from time-lapse geophysical data
M. Cho Miltin (2012), xi, 79 pp
ISBN: 978-3-89336-823-5

Band / Volume 155
Tiefentschwefelung von Flugturbinenkraftstoffen für die Anwendung in mobilen Brennstoffzellensystemen
Y. Wang (2012), 205 pp.
ISBN: 978-3-89336-827-3

Band / Volume 156
Self-consistent modeling of plasma response to impurity spreading from intense localized source
M. Koltunov (2012), V, 113 pp.
ISBN: 978-3-89336-828-0

Band / Volume 157
Phosphorsäureverteilung in Membran-Elektroden-Einheiten dynamisch betriebener Hochtemperatur-Polymerelektrolyt-Brennstoffzellen
W. Maier (2012), VI, 105 pp.
ISBN: 978-3-89336-830-3

Band / Volume 158
Modellierung und Simulation von Hochtemperatur-Polymerelektrolyt-Brennstoffzellen
M. Kvesic (2012), ix, 156 pp.
ISBN: 978-3-89336-835-8

Band / Volume 159
Oxidation Mechanisms of Materials for Heat Exchanging Components in CO_2/H_2O-containing Gases Relevant to Oxy-fuel Environments
T. Olszewski (2012), 200 pp.
ISBN: 978-3-89336-837-2

Band / Volume 160
Ice Crystal Measurements with the New Particle Spectrometer NIXE-CAPS
J. Meyer (2013), ii, 132 pp.
ISBN: 978-3-89336-840-2

Band / Volume 161
Thermal Shock Behaviour of Different Tungsten Grades under Varying Conditions
O. M. Wirtz (2013), XIV, 130 pp.
ISBN: 978-3-89336-842-6

Weitere ***Schriften des Verlags im Forschungszentrum Jülich*** unter
http://wwwzb1.fz-juelich.de/verlagextern1/index.asp

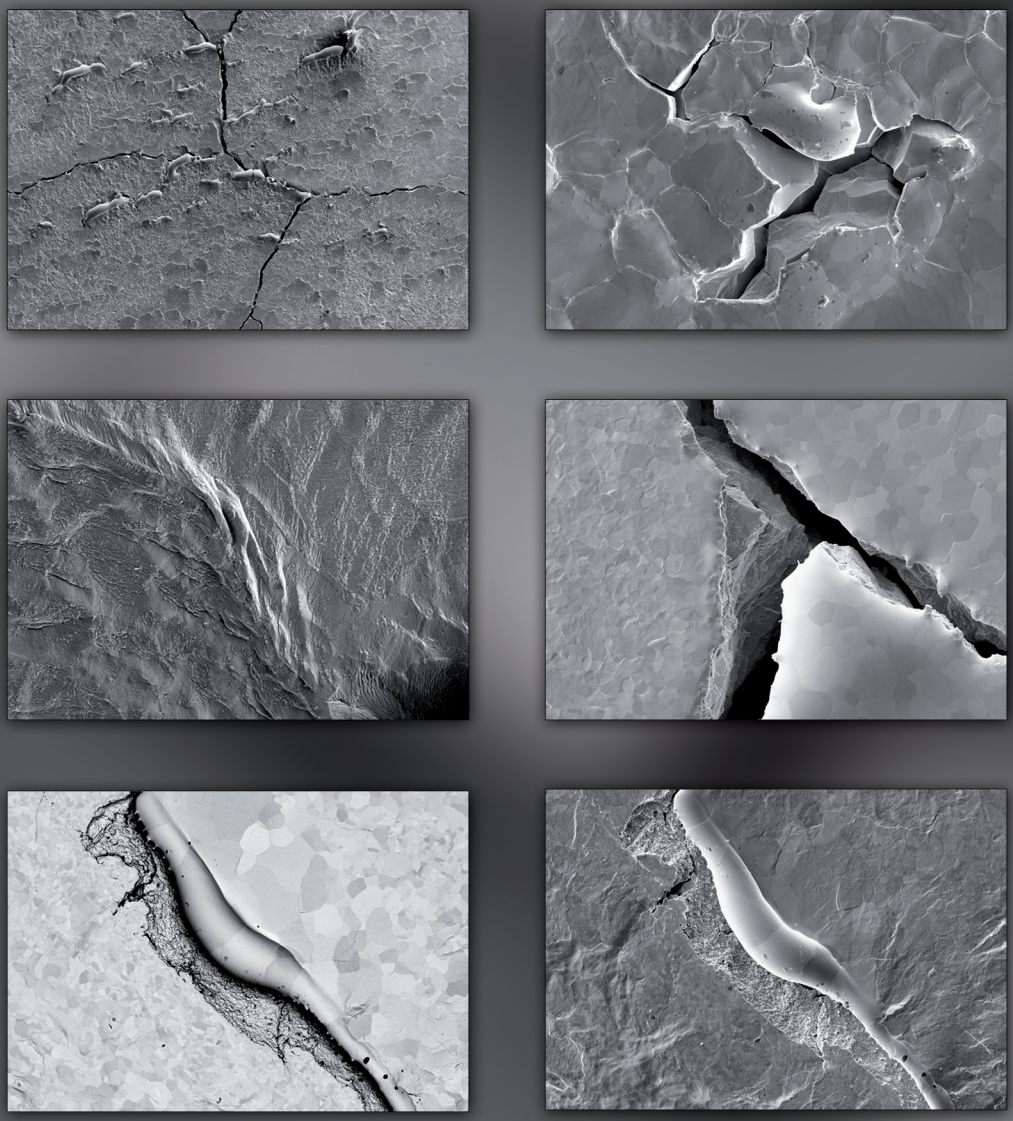

Energie & Umwelt / Energy & Environment
Band / Volume 161
ISBN 978-3-89336-842-6

JÜLICH
FORSCHUNGSZENTRUM